

QUANTUM ENGINEERING WITH QUANTUM OPTICS

A DISSERTATION

SUBMITTED TO THE DEPARTMENT OF APPLIED PHYSICS

AND THE COMMITTEE ON GRADUATE STUDIES

OF STANFORD UNIVERSITY

IN PARTIAL FULFILLMENT OF THE REQUIREMENTS

FOR THE DEGREE OF

DOCTOR OF PHILOSOPHY

Joseph Kerckhoff

May 2011

Abstract

Despite initial set backs in the 1980s, the prospect for large scale integration of optical devices with high spatial-density and low energy consumption for information applications has grown steadily in the past decade. At the same time these advances have been made towards *classical* information processing with integrated optics, largely in an engineering context, a broad physics community has been pursuing *quantum* information processing platforms, with a heavy emphasis on optics-based networks. But despite these similarities, the two communities have exchanged models and techniques to a very limited degree. The aim of this thesis is to provide examples of the advantages of an engineering perspective to quantum information systems and quantum models to systems of interest in optical engineering, in both theory and experiment.

I present various observations of ultra-low energy optical switching in a cavity quantum electrodynamical (cQED) system containing a single emitter. Although such devices are of interest to the engineering community, the dominant, classical optical models used in the field are incompatible with several photon, ultra-low energy devices like these that evince a discrete Hilbert space and are perturbed by quantum fluctuations. And in complement to this, I also propose a nanophotonic/cQED approach to building a self-correcting quantum memory, simply “powered” by cw laser beams and motivated by the conviction that for quantum engineering to be a viable paradigm, quantum devices will have to control themselves. Intuitive in its operation, this network represents a *coherent feedback network* in which error correction occurs entirely “on-chip,” without measurement, and is modeled using a flexible formalism that suggests a quantum generalization of electrical circuit theory.

Acknowledgement

One can't get through graduate school without help from a ridiculously large number of people (and a few cats). Here I'll try to acknowledge a few.

Tiku Majumder, my undergraduate advisor, who paid me to do research after only a single class of undergraduate physics and with whom I continued to work for much of my “free time” in college. His (continuing) encouragement and advice has so much to do with so many of my career choices in college and beyond. He's seriously great; look at where all his students have gone.

Ben Lev, into whose research shoes I stepped immediately after joining Hideo's group at Caltech. In three short months, on top of everything else he had going on, he was savvy enough to impart enough knowledge and excitement for the work to give me an excellent start.

Paul Barclay, my first collaborator, friend and housemate. Through him I had the privilege early on of seeing how a physicist learns new things and he always worked with me as an equal, even with all his experience. Through him, I've also met so many other great scientists at Caltech and HP.

Luc Bouten, with whom I actively worked only briefly and remotely, but whose mark has been indelible. If he hadn't been so bored with making figures, I never would have learned about QSDEs. I wouldn't be a “half-theorist” if it wasn't for his help, encouragement and writings.

Rick Pam, my teaching teacher, through whom I learned so much about inspiring younger students and conducting great courses. Every applied physics grad student should be his TA. I'm greatly in Mark Kasevich and Doug Osheroff's debt in this regard too.

Dmitri Pavlichin, enduring co-author. I don't understand why we work well together, but we do. He's taught me a lot and I've taught myself a lot trying to teach him.

Tony Miller, I don't know 1/5th of the technical things he knows. His practical, technical and actual gifts have been an essential part of me actually getting things done around here.

Hendra Nurdin was so critical in moving a solid third of this thesis work from mere concept to actual practice. His help, advice and interests have opened a whole new field to me.

Mike Armen, it's hard to know where to start. I snatched so many things and thoughts he knowingly and unknowingly prepared, sometimes for me and sometimes not. Seriously, he's the best style coach I've had. (in physics)

The Group. No, I'm not going to list them all. Everyone hates that anyways. Science is a social enterprise and I can't imagine having done any of this without being in and around such talented people.

Hideo Mabuchi was perhaps the perfect advisor for me. The support, advice, encouragement, freedom, talent and resources he's given me have been rare indeed. Perhaps my highest praise is that I can't think of a better place for me to have spent the past six years than in the group he's constructed.

Oz and GC. I don't care what everyone else says. You're great. May your little lives be full of packing tissue and turkey.

Mom and Dad, emotional, administrative, culinary, financial, and life support. Everyone's jealous that they've let me live with them the past two years (seriously, they are). It would be an understatement to say I owe everything to them.

Sara, would you believe it if I told you I did this all for you? Let's get married!

Contents

Abstract	v
Acknowledgement	vi
I Quantum Optics with Quantum Stochastic Differential Equations	3
1 Quantum stochastic differential equations	6
1.1 The quantum noise process	7
1.2 Quantum stochastic calculus	9
1.3 The master equation	15
1.4 The series product	16
1.5 Multiple fields	19
1.6 Adiabatic elimination with QSDEs	20
2 Optical measurements and state estimation	22
2.1 Optical measurement	22
2.1.1 Photon counting	22
2.1.2 Homodyne measurement	24
2.1.3 Calculating photocurrent statistics	26
2.2 Quantum trajectories	31
2.2.1 The stochastic Schrödinger equation	32

II	Quantum ‘Bistability’ in Cavity QED	35
3	The cQED model	37
3.1	The cQED master equation	37
3.2	The QSDE representation	41
3.3	The Maxwell-Bloch equations	43
4	Single atom ‘bistability’	47
4.1	Absorptive ‘bistability’	48
4.2	Dispersive ‘bistability’	55
4.2.1	The Jaynes-Cumming ladder	55
4.2.2	Phase ‘bistability’ in highly-excitated cQED	58
4.3	Toward optical control	61
4.3.1	Driven transition dynamics	62
4.3.2	Dynamics without control	64
4.3.3	Control dynamics	66
4.3.4	Simulation of a controlled quantum dot system	67
5	The broadband cavity QED apparatus	70
5.1	The atom	71
5.2	The cavity	72
5.3	A tour of the apparatus	76
5.3.1	Science cavity locking and probing	76
5.3.2	Delivering the atoms	80
5.3.3	Transit detection and homodyne measurements	81
6	Observations of optical ‘bistability’	84
6.1	Amplitude ‘bistability’	84
6.2	Phase ‘bistability’	90

III	Autonomous Nanophotonic Quantum Memories	98
7	Preliminary Models	102
7.1	Quantum error correction	102
7.1.1	The bit-flip and phase-flip codes	103
7.1.2	The 9 qubit Bacon-Shor code	106
7.2	cQED parity networks	109
7.2.1	Physical model of a cQED TLS	109
7.2.2	Continuous parity measurement in a nanophotonic network	115
8	Autonomous QEC nanophotonic networks	122
8.1	An autonomous bit-/phase-flip network	123
8.1.1	Intuitive operation	123
8.1.2	Network model and dynamics	128
8.2	The autonomous subsystem QEC network	132
	Bibliography	141

List of Tables

1.1	The quantum Ito table	12
7.1	Bit-flip code syndrome measurements	104

List of Figures

1.1	QSDE as I/O model	10
1.2	QSDE network example	17
2.1	Optical homodyne measurement	24
3.1	cQED concept	38
4.1	Steady state absorptive bistability	49
4.2	Steady state MBE vs. quantum solutions	50
4.3	Amplitude bistability W-functions	51
4.4	Amplitude bistability trajectories	52
4.5	Steady state amplitude bistability photocurrents	53
4.6	The Jaynes-Cummings spectrum	56
4.7	cQED transmission spectrum	57
4.8	Phase bistability steady state W-functions	60
4.9	Controlled phase switching in a quantum dot	68
5.1	Cavity mounting schematic	72
5.2	Cavity transmission noise	75
5.3	Cavity mount mechanical resonances	76
5.4	Cavity stabilization and probing optics	77
5.5	Laser frequency noise spectrum	79
5.6	Atom transits with weak heterodyne detection	82
6.1	Experiment concept	85

6.2	Experimental absorptive ‘bistability’ signal	86
6.3	Experimental steady state absorptive ‘bistability’	87
6.4	Photocurrent autocorrelation	88
6.5	cQED absorptive hysteresis.	89
6.6	Near-detuned phase ‘bistability’	91
6.7	Experimental phase ‘bistability’ signal	92
6.8	Phase switching rate estimation	93
6.9	High-drive-induced atom loss	94
6.10	Enhanced switching rate with cw control probe	97
6.11	A traditional quantum ‘circuit’	100
7.1	9 qubit subsystem code operator groups	106
7.2	One-sided cavity reflection	110
7.3	cQED qubit level structure	111
7.4	Cavity parity probe network	116
7.5	Bell-state production in a cQED network	117
7.6	Performance of reduced model as an approximate quantum filter	121
8.1	The autonomous bit-/phase-flip nanophotonic network	124
8.2	cQED relay level structure	125
8.3	QSDE circuit schematic for the bit-/phase-flip network	127
8.4	Logical fidelity in bit-flip network	131
8.5	The autonomous 9-qubit nanophotonic network	133
8.6	Alternate 9-qubit probe routing	135
8.7	Logical fidelity in the 9-qubit network	138
8.8	Correction of different error classes in 9-qubit network	139

Outline

On some days, my research has been motivated by the expectation that quantum optics will be a future discipline of electrical engineering. On others, it's been driven by a notion that a generalized concept of the electrical circuit should guide a future strain of quantum optics. Whichever way, both the experiments and theoretical work described below have rested heavily on a unifying formalism of open quantum optical systems that makes both perspectives natural, at the level of individual devices and for large scale networks.

Part **I** introduces this formalism. While quantum stochastic differential equations (QSDEs) have been developed by many authors over the past three decades, I have increasingly recognized a need for an informal introduction to the formalism to complement the technical literature. Chapter **1** describes this approach to modeling open quantum optical systems as noisy, Markovian dynamical processes. The interpretation of the QSDE model as describing input-output (I/O) devices for quantum fields is emphasized, as well as a method for constructing composite network models built from series and parallel interconnections of individual devices. Chapter **2** describes how continuous optical measurement is naturally incorporated into the formalism and gives it much of its utility, bringing together theories of weak measurement and real time state estimation.

Part **II** centers on various observations of spontaneous optical switching of the field transmitted by a Fabry-Perot cavity containing a single, strongly coupled Cs atom. While confirming long-standing theoretical predictions, these observations also highlight that binary optical signaling persists even into the 'deep quantum' regime of

devices with countable photon numbers and single emitters. As nanophotonic research pushes into the attojoule device regime, these observations underscore that quantum optical models will soon be essential for understanding nonlinear optical device physics, offering both technological problems and opportunities not captured by commonly employed semiclassical models. Chapter 3 introduces models for single-atom cavity quantum electrodynamics (cQED) in both a semiclassical approximation and as a QSDE optical I/O device. Chapter 4 describes how both models predict an I/O bistable response as the cQED device is driven at and into the atomic saturation regime. The picture that emerges is subtle, however: the quantum optical model (the more accurate model) both predicts disrupted signal stability (due to fractionally large quantum fluctuations) and sometimes enhanced signal discretization (due to a discrete Hilbert space). Two different I/O regimes are considered, absorptive/amplitude bistability, which occurs at the cusp of atomic saturation, and dispersive/phase bistability which appears well into the saturation regime. Chapter 5 then introduces the experimental apparatus built to measure the optical field transmitted by a high finesse Fabry-Perot cavity containing a single, strongly coupled Cs atom with broadband optical homodyne detection, emphasizing the improvements and continuing issues in the system since 2009. Finally, chapter 6 reports observations of the predictions introduced in chapter 4.

Part III considers how nanophotonic network models could aid the development of quantum memories. This work imports abstract concepts of quantum error correction (QEC) into a hardware-specific circuit formalism, yielding an approach to QEC that is well-suited to developing robust quantum technologies. These technologically homogenous nanophotonic networks are noteworthy in that the error suppression occurs continuously and autonomously, that is with a minimal amount of oversight and supporting hardware. Chapter 7 first introduces the specific QEC codes our designs emulate. It also details a physical model for cQED devices and networks appropriate to implement these codes and characterizes how their performance rapidly improves in a nanophotonic context. Finally, chapter 8 describes two types of designs for nanophotonic networks that emulate three different codes and characterizes their performance.

Part I

Quantum Optics with Quantum Stochastic Differential Equations

Introduction

This first part introduces a formalism for modeling open quantum optical systems that has been essential in both my experimental and theoretical work. While quantum stochastic differential equations (QSDEs) represent a rigorous stochastic dynamical modeling unfamiliar to most physicists, the approach becomes physically intuitive once internalized. QSDEs take quantum field theory as the underlying physical model [GPZ92, GZ04], but their manipulations appear as a quantum generalization of electrical circuit theory and are able to adapt many powerful techniques from classical control theory into the quantum regime, e.g. [NJD09, NJP09, JNP08, GJ09b]. Sufficiently general to describe the dynamics of most systems foreseeable in quantum optical systems, with or without measurement of optical fields, with or without stabilizing (coherent optical *or* classical ‘electrical’) feedback, these models are attractive due to their physically intuitive formulation [KNPM10] that admits both analytic and numerical analysis through connections to theories of continuous measurement [Bar90], state estimation [BvHJ07] and control [NJP09].

While the theory of QSDEs and QSDE networks has been developed by many authors in the past three decades, the literature is fairly mathematical [HP84, Par92, Fag90, GPZ92, Bar90, BvHJ07, BvHS08, GJ09b]. Over the past few years, many students have asked me to explain how to use QSDEs in their own work, but I’ve found that they usually get discouraged by the formal derivations and manipulations. Somehow, I got through that initial hurdle and they have been essential in my work ever since. As I feel there is a bright future for this formalism and that it has a natural role to play in the emerging field of quantum optical engineering, this first part introduces QSDEs and their manipulations that underlie most of the analysis

in the subsequent experimental and theoretical chapters. As the formalism has been incredibly useful to me as a *tool*, not an object of study in itself, the concepts are presented in a non-formal manner, at a level appropriate for a reader with grounding in more mainstream quantum optics. The ‘results’ in this part are pedagogical, if that, aiming to present an intuitive explanation of QSDEs to complement the proper formulation found in the literature.

Chapter 1

Quantum stochastic differential equations

Loosely, quantum stochastic differential equation (QSDEs) are a method of modeling open quantum optical systems that resembles a quantum version of electrical circuit theory. Free, bosonic quantum fields play the role of electrical current-carrying wires, while localized systems like atoms or optical resonators function as input-output (I/O) devices that affect the fields, but are also affected by them.

QSDEs are a rigorous, self-consistent mathematical formalism, but they are useful because they represent a good approximation of most systems foreseeable in quantum optics [GZ04, GPZ92]. This chapter begins by motivating the reasonableness of using this representation to describe physical quantum optic phenomena, but will gradually drift into working just with the abstracted objects themselves.

This introduction is quick and is meant to give the reader a glimpse of all the steps on the way to a complete theory of QSDEs and their physical justification. A more complete picture (although much longer) may be constructed through references cited along the way, especially [GZ04, GPZ92, BvHJ07, Bar90, GJ09b, BvHS08].

1.1 The quantum noise process

As is common when considering an open quantum system, the global system composed of a *system* (i.e. a localized system like an atom or optical resonator) and *bath* (i.e. free optical fields) is considered ‘closed’ and its dynamics may be described with the Hamiltonian

$$H_0 = H_s + H_b + H_i \quad (1.1)$$

where the system and bath have their own, internal evolution govern by H_s and H_b , respectively, and the two subsystems are also coupled via the interaction H_i . Hereon, I will use “system” to refer to the localized system (with Hamiltonian H_s) and “global system” to refer to the totality composed of isolated system(s) and bath(s). In the quantum optics context, we assume that the bath is comprised of a dense spectrum of bosonic fields, such that ($\hbar = 1$)

$$H_b = \int_0^\infty d\omega \omega b^\dagger(\omega)b(\omega) \quad (1.2)$$

where $b(\omega)$ are annihilation operator “densities,” † the Hermitian conjugate, and $[b(\omega), b^\dagger(\omega')] = \delta(\omega - \omega')$. We don’t need to specify anything about H_s yet, but the coupling between the system and bath has to have a particular linear form

$$H_i = i \int_0^\infty d\omega \sqrt{\kappa(\omega)} (cb^\dagger(\omega) - c^\dagger b(\omega)) \quad (1.3)$$

where c is some operator on the system and $\kappa(\omega)$ is a real-valued function describing the strength of the interaction. Already, this interaction typically makes an approximation, commonly known as the rotating wave approximation, that coupling terms of the form $c^\dagger b^\dagger(\omega)$ and its hermitian conjugate (which exist in a complete description) oscillate too quickly to influence the relatively slow dynamics we care about [GPZ92]. This approximation is itself only good when H_i is assumed to be weak compared to the evolution of both c under H_s and $b(\omega)$ under H_b . This is usually a very good approximation in quantum optics, as the coupling rates typically operate on GHz-MHz frequency scales (call these $\tilde{\kappa}$ frequency scales), while the principle system and bath

operators oscillate at frequencies of order 100s of THzs (i.e. optical frequencies).

It is convenient to go into an interaction frame such that the global system states become

$$|\psi'_t\rangle \rightarrow e^{i(H_s+H_b)t}|\psi'_t\rangle \equiv |\psi_t\rangle \quad (1.4)$$

and the operators also gain some time-dependence, accordingly. In this picture, the global state evolves according to the Schrödinger equation

$$\frac{d}{dt}|\psi_t\rangle = \int_0^\infty d\omega \sqrt{\kappa(\omega)}(c(t)b^\dagger(\omega, t) - c^\dagger(t)b(\omega, t))|\psi_t\rangle. \quad (1.5)$$

Given H_b , we have $b(\omega, t) = e^{-i\omega t}b(\omega, 0)$, and it is typical that in this picture $c(t) = e^{-i\omega_0 t}c$, where ω_0 is in the optical regime. In this case we can rewrite equation (1.5) as

$$\frac{d}{dt}|\psi_t\rangle = \sqrt{2\pi\kappa(\omega_0)}(cb^\dagger(t) - c^\dagger b(t))|\psi_t\rangle, \quad (1.6)$$

where

$$b(t) = \frac{1}{\sqrt{2\pi\kappa(\omega_0)}} \int_0^\infty d\omega \sqrt{\kappa(\omega)}b(\omega, 0)e^{-i(\omega-\omega_0)t}. \quad (1.7)$$

At this point, we make a *Markov approximation* that the coupling strength $\kappa(\omega)$ varies slowly around ω_0 , slow compared to the inverse time scales $\tilde{\kappa}$ on which we expect the interesting dynamics to occur. Also, we allow ourselves to extend the lower limit on the definition of $b(t)$ to $-\infty$, justifiable as $\omega_0 \gg \tilde{\kappa}$. With these approximations in hand, we can calculate the commutator of $b(t)$ [GPZ92]

$$[b(t), b^\dagger(t')] \approx \int_{-\infty}^\infty d\omega e^{-i(\omega-\omega_0)(t-t')} \frac{\kappa(\omega)}{2\pi\kappa(\omega_0)} \approx \delta(t-t'). \quad (1.8)$$

Thus, due to our approximations, $b(t)$ looks very much like a delta-correlated white noise process. In fact, with our aim set on a QSDE formalism, it is better to think of it as a sort of *quantum noise process*, rather than as its definition (1.7) as the integral of Schrödinger-picture operator densities in an interaction frame. Each $b(t)$ exerts its influence on the global system in Eq. (1.6) in chronological succession, independent of all other $b(t')$ [GPZ92]. For this reason, $b(t)$ may be considered noise ‘inputs’ to the system [GZ04], with the ‘time’ t indexing the time at which the operator $b(t)$

interacts with the system; call them $b_{in}(t) \equiv b(t)$. Essentially a Fourier transform of $b(\omega)$, $b(t)$ may also be thought of as a time-domain annihilation operator density, acting on the infinitesimal segment of field that interacts with the system at time t .

Now, for $t_1 > t$, consider

$$b_{out}(t) = \frac{1}{\sqrt{2\pi}} \int_{-\infty}^{\infty} d\omega e^{-i(\omega-\omega_0)(t-t_1)} b(\omega, t_1), \quad (1.9)$$

which is almost the same as $b_{in}(t)$, except that it is defined in terms of $b(\omega, t_1)$ in the ‘future.’ Comparing $b_{in}(t)$ and $b_{out}(t)$ is more naturally done in the Heisenberg picture. In this picture, given our interaction Hamiltonian, it may be straightforwardly shown that for any choice of t_1 in the definition of $b_{out}(t)$ [GZ04]

$$b_{out}(t) = b_{in}(t) + \sqrt{2\pi\kappa(\omega_0)}c(t). \quad (1.10)$$

In other words, $b_{out}(t)$ is a linear superposition of the ‘noise’ that interacts with the system at time t , plus a contribution from the system at time t , proportional to $c(t)$ (which is itself dependent on all previous input values of $b_{in}(t')$, $t' < t$). For this reason, $b_{out}(t)$ may be considered the field ‘output’ of the system at time t .

1.2 Quantum stochastic calculus

Although it may appear we now have a very nice quantum optic I/O theory, our input and output operators are highly singular. For example, we immediately run into a problem if we try to calculate the expectation of $b(t)b^\dagger(t)$ on the vacuum field state [GPZ92]

$$\langle vac|b(t)b^\dagger(t)|vac\rangle = \langle vac|b(t)b^\dagger(t) - b^\dagger(t)b(t)|vac\rangle = \delta(0) \quad (1.11)$$

where we have used $b(t)|vac\rangle = 0$. Fortunately, a solution to problems of this nature is well known for classical noisy systems. Roughly speaking, we consider $b(t)$ to be the

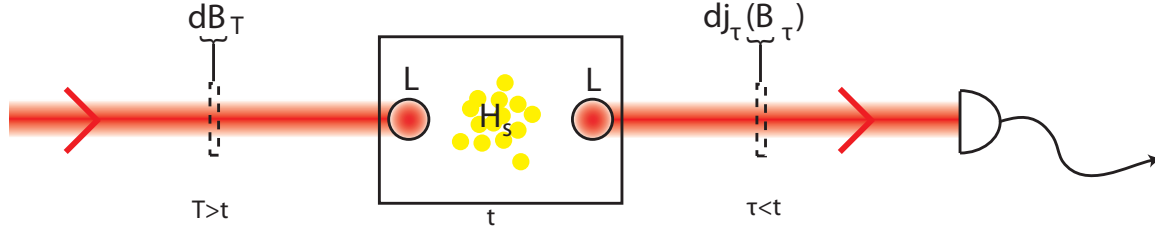


Figure 1.1: A cartoon depiction of the QSDE I/O formulation. A single, free optical mode couples via an operator L to a fixed Hamiltonian system (H_s), affecting it and being affected by it. After interaction, the field continues to propagate, and is possibly detected. The fundamental noise increment dB_t may be thought of as the annihilation operator on an infinitesimal segment of the field that interacts with the system at time t . At time t , the segment indexed by $T > t$ has yet to interact with the system (an ‘input’), but the segment indexed by $\tau < t$ already has (and is an ‘output’), transforming its noise increment as $dj_\tau(B_\tau)$ (Eq. (1.28)).

(ill-defined) derivative of some rapidly varying, *noise integral* [GPZ92, GZ04, Gar04]

$$\begin{aligned} B_t - B_{t_0} &\equiv \int_{t_0}^t dt' b(t') \equiv \int_{t_0}^t dB_{t'}, \\ B_t^\dagger - B_{t_0}^\dagger &\equiv \int_{t_0}^t dt' b^\dagger(t') \equiv \int_{t_0}^t dB_{t'}^\dagger. \end{aligned} \quad (1.12)$$

In a classical analogy, $b(t)$ is like the velocity of a particle undergoing Brownian motion (i.e. diffusion), whereas B_t is its position. The usual terminology is to call B_t the *annihilation* and B_t^\dagger the *creation process*. Later on we’ll also use another noise process, called the *gauge process* [Bar90]

$$\Lambda_t - \Lambda_{t_0} \equiv \int_{t_0}^t dt' b^\dagger(t') b(t') \equiv \int_{t_0}^t d\Lambda_{t'}. \quad (1.13)$$

Note that through these definition and the commutator of $b(t)$, B_t , B_t^\dagger and Λ_t act as the identity on processes that don’t overlap with the time interval $(0, t]$, a property called *adapted* [BvHJ07, Bar90]. With these definitions, our Schrödinger equation

above (1.6) is more accurately considered an integral equation

$$|\psi, t\rangle - |\psi, t_0\rangle = \int_{t_0}^t (LdB_t^\dagger - L^\dagger dB_t)|\psi, t'\rangle, \quad (1.14)$$

where we have now defined the *coupling operator* $L \equiv \sqrt{2\pi\kappa(\omega_0)}c$. Replacing the $b(t)$ and $b^\dagger(t)$ with dB_t and dB_t^\dagger in (1.6) produces a *quantum stochastic differential equation* (QSDE) representing the evolution of the global system in the Schrödinger picture,

$$d|\psi_t\rangle = (LdB_t^\dagger - L^\dagger dB_t)|\psi_t\rangle, \quad (1.15)$$

but it is understood as merely a symbolic abbreviation of integral equation (1.14). This brings us to the critical question of how do we calculate these integrals? It can be shown that if we require the noises to obey ordinary calculus (e.g. that $d(B_t^\dagger B_t) = d(B_t^\dagger)B_t + B_t^\dagger d(B_t)$), as would be expected of a physical system described with “natural” processes and we’ve implicitly assumed so far, then these integrals have to be understood as the limit (for example)

$$\int_{t_0}^t f(t')dB_{t'} = \lim_{n \rightarrow \infty} \frac{1}{2} \sum_{i=0}^n (f(i) + f(i+1))(B_{i+1} - B_i) \quad (1.16)$$

where $f(t)$ is some adapted function, and is known as a *Stratonovich integral* [GPZ92, GZ04, Gar04]. However, there is a problem here: $f(i+1)$ does not commute with the interval $B(i+1) - B(i)$ in general, which makes working with these equations very awkward. This means that

$$\int_{t_0}^t f(t')dB_{t'} \neq \int_{t_0}^t dB_{t'} f(t'), \quad (1.17)$$

causing a practical nightmare in any integral calculation (in a classical analogy, the noise processes $f(t)$ and dB_t are correlated and their product is difficult to integrate). An alternative definition of the stochastic integral is

$$\int_{t_0}^t f(t')dB_t = \lim_{n \rightarrow \infty} \sum_{i=0}^n f(i)(B_{i+1} - B_i) \quad (1.18)$$

dX/dY	dB_t^k	$dB_t^{k\dagger}$	$d\Lambda_t^{kl}$	dt
dB_t^i	0	$\delta_{ik}dt$	$\delta_{ik}dB_t^l$	0
$dB_t^{i\dagger}$	0	0	0	0
$d\Lambda_t^{ij}$	0	$\delta_{jk}dB_t^{i\dagger}$	$\delta_{jk}d\Lambda_t^{il}$	0
dt	0	0	0	0

Table 1.1: The quantum Ito table by which the noncommutative product of two quantum noise increments $dXdY$ is evaluated when the fields are in the vacuum state. Latin superscripts index the free field modes the processes act on and all noise products at dissimilar times vanish.

which is called an *Ito integral* [GPZ92, GZ04, Gar04]. Now, in symbolic form, $[f(t), dB_s] = 0 \forall s \geq t$. Notice that the Stratonovich integral is defined by an average of $f(t)$ over an infinitesimal increment $B_{t+dt} - B_t$, while the Ito is defined by the initial value of $f(t)$. In a smooth function, there would be no difference between the two definitions as the increment shrinks to the infinitesimal, but noise is decidedly non-smooth!

Although we always work with Ito QSDEs, there is a price to be paid. As is the case in classical Ito integrals, the normal rules of calculus no longer apply [Gar04]. With a classical noisy process we describe its infinitesimal increment by a straightforward Taylor expansion $df(X_t) = f'(X_t)dX_t + \frac{1}{2}f''(dX_t)^2 + \dots$. However, when X_t is an Ito noise process, $(dX_t)^2$ is of order dt (in the case of Brownian motion the position variance increases linearly in time so that if X_t is the position at time t , $(dX_t)^2 \propto dt$). A proper differential representation of the integral should carry all expansion terms $\leq \mathcal{O}(dt)$, including these second order Taylor expansion terms $\sim (dX_t)^2$.

In order to define an equivalent calculus for the quantum Ito processes B_t and B_t^\dagger , it turns out that we have to define the state of the bath. Although the formalism can be applied to any Gaussian field state initially un-entangled with the fixed system [GPZ92, HP84, Par92], we almost always assume that the field is in a vacuum state (why this is reasonable, even when we probe systems with lasers will be discussed later), which means that the entire system factorizes $\rho = \rho_s \otimes \rho_{vac}$. Under this assumption, quantum Ito calculus may be performed by expanding all differentials to second order and evaluating the terms quadratic in the increments by the quantum

Ito table 1.1. For example, for the adapted quantum stochastic processes X and Y , we calculate

$$d(XY) = (dX)Y + X(dY) + dXdY, \quad (1.19)$$

where the last term is evaluated according to the above table. Taken together, the rule of differentiation and the table above are called the *quantum Ito rule* [HP84, GPZ92, BvHJ07].

While the derivation of table 1.1 for general quantum noise processes is found in [HP84, Par92], its construction is based on calculations similar to Eq. (1.11). For example, note that

$$\begin{aligned} \langle vac|B_t B_t^\dagger|vac\rangle &= \langle vac|\int_0^t dB_{t'} \int_0^t dB_{t''}^\dagger|vac\rangle \\ &= \langle vac|\int_0^t b(t')dt' \int_0^t b^\dagger(t'')dt''|vac\rangle \\ &= \langle vac|\int_0^t dt' \int_0^t dt'' [b(t'), b^\dagger(t'')]|vac\rangle \\ &= \langle vac|\int_0^t dt' \int_0^t dt'' \delta(t' - t'')|vac\rangle \\ &= \langle vac|\int_0^t dt'|vac\rangle \\ &= \langle vac|t|vac\rangle, \end{aligned} \quad (1.20)$$

which suggest that $dB_t dB_t^\dagger = dt$ when the field is in the vacuum state, as given by the table 1.1.

We now have two definitions of quantum stochastic processes in quantum optics: the Stratonovich and Ito. They each have their merits, namely that Stratonovich is in some sense more “natural” (as ordinary calculus applies), while Ito is much easier to manipulate. Fortunately, we can have our cake and eat it too: it is possible to convert between the two descriptions for our dynamics whenever convenient. The correspondence comes from noting that our global system’s equation of motion has a straightforward solution. As Eq. 1.15 was derived assuming normal calculus, it must be considered a Stratonovich integral. It then follows from (1.15) that the time

evolution of any operator in the Heisenberg picture is $f(t) = U_t^\dagger f(0) U_t$, where we use ordinary calculus to calculate U_t as the *unitary* propagator

$$U_t = \mathcal{T} \exp \left\{ L \int_0^t dB_{t'}^\dagger - L^\dagger \int_0^t dB_{t'} \right\} \quad (1.21)$$

where \mathcal{T} is the time-ordering operator. But, as U_t has no t' dependence in the integrals, it may be considered either a Stratonovich or Ito integral. If we interpret the propagator as a Stratonovich integral, we re-apply our familiar rules of calculus to arrive at a (symbolic) differential equation for our propagator

$$(\mathbf{S})dU_t = (LdB_t^\dagger - L^\dagger dB_t)U_t, \quad U_0 = I, \quad (1.22)$$

where I is the identity. However, as is more common, if we consider U_t an Ito integral, its differential form is arrived at through a second-order expansion and application of the quantum Ito rule

$$(\mathbf{I})dU_t = (LdB_t^\dagger - L^\dagger dB_t - \frac{1}{2}L^\dagger L dt)U_t, \quad U_0 = I. \quad (1.23)$$

Thus, conversion between the two representation of the dynamics is done simply through the identification of these two differential equations for the propagator U_t [GPZ92, GZ04].

The other important thing to note about the propagator is that all of the fundamental noise increments $dB_t, dB_t^\dagger, d\Lambda_t$ commute with any propagator $U_{[r,s]}$, $r, s \geq t$, which evolves the global system for the time interval from s to r [BvHJ07, Bar90]. This represents the intuitive property is that the field does not evolve after it has interacted with the system, but simply propagates freely away, which will be of particular importance when we consider making measurements of the field. Moreover, U_t is adapted, so it also commutes with the noise increments dB_s , $s \geq t$. This represents a convenient notion that the free field “noise” that drives the system at time t or later is independent of any past, global dynamics.

It is often the case that in addition to the system-bath coupling, there are slow, internal system dynamics that also perturb the otherwise fast $\sim \omega_0$ evolution in

the lab frame. This common case is dealt with by carrying the perturbing system Hamiltonian H , through all the above analysis such that, at the end, we are left with an Ito QSDE for the propagator (dropping the (\mathbf{I}) hereon)

$$dU_t = (LdB_t^\dagger - L^\dagger dB_t - (iH + \frac{1}{2}L^\dagger L)dt)U_t, \quad U_0 = I. \quad (1.24)$$

Expressing the entire system dynamics, this equation of motion for the propagator is the main object of analysis in most QSDE models [GZ04, BvHJ07, GJ09b].

You may have noticed that at no point have we “traced over the bath” in the analysis, as is common to do in open quantum systems theory. This is because we typically measure the bath to some extent. Before we get to the topic of measurement, though, let’s consider what the above propagator tells us about the evolution of system expectations when an experimenter makes no measurements.

1.3 The master equation

Say we have some system operator X and we want to calculate the evolution of its expectation in time. The evolution of X in the Heisenberg picture is $U_t^\dagger XU_t \equiv j_t(X)$. A clearer picture of $j_t(X)$ comes from considering its differential form (using the quantum Ito rule) [BvHJ07]. For this calculation, recall that as we are considering Ito noise processes, the noise increments at time t are independent of the propagators up to that point, or in other words $[U_t, dB_t] = [U_t, dB_t^\dagger] = 0$. Moreover, as we are limiting ourselves to system operators, the noise increments also commute with X . With these, we have

$$\begin{aligned} dj_t(X) &= d(U_t^\dagger)XU_t + U_t^\dagger X d(U_t) + d(U_t^\dagger)X d(U_t) \\ &= j_t(\mathcal{L}^\dagger X)dt + j_t([L^\dagger, X])dB_t + j_t([X, L])dB_t^\dagger \end{aligned} \quad (1.25)$$

where the super-operator $\mathcal{L}^\dagger X = i[H, X] + L^\dagger XL - \frac{1}{2}(L^\dagger LX + XL^\dagger L)$ is called the *Lindblad generator* in this Heisenberg picture. The expectation of X as a function of time is just $\langle j_t(X) \rangle = \text{Tr}[\rho j_t(X)]$, where $\rho = \rho_s \otimes \rho_{vac}$ is the global system state. The

differential form of this expectation is simply the expectation of the above QSDE. However, this expression may be greatly simplified due to our assumption that the bath is in the vacuum state. From our definition of the noise increments, $dB_t|vac\rangle = \langle vac|dB_t^\dagger = 0$. Thus, the expectation of any term in the above expression for $j_t(X)$ that contains dB_t or dB_t^\dagger is zero and we are left with

$$d\langle j_t(X) \rangle = \langle j_t(\mathcal{L}^\dagger X) \rangle dt \quad (1.26)$$

which may be familiar as the *master equation* used in many other, non-QSDE contexts for describing the unconditional evolution of an open quantum system [Car93a, GZ04, Gar04].

From Eq. (1.26) and the definition of the expectation, we can also derive an unconditional master equation for the *system* state in the Schrödinger picture, for use in calculating expectations of arbitrary X :

$$d\rho_{uc} = \mathcal{L}\rho_{uc}dt \quad (1.27)$$

where $\mathcal{L}\rho = -i[H, \rho] + L\rho L^\dagger - \frac{1}{2}(L^\dagger L\rho + \rho L^\dagger L)$.

1.4 The series product

You may have noticed that we dropped the “input” and “output” terminology when we moved from the “ $b(t)$ ” to the QSDE description. In some sense, what’s been developed here is more flexible, but still contains that I/O intuition. For example, consider the evolution of the noise process (using the quantum Ito rule)

$$dj_t(B_t) = j_t(L)dt + dB_t \quad (1.28)$$

which is equivalent to the relationship between $b_{in}(t)$ and $b_{out}(t)$ considered above (1.10), and is depicted in Fig. 1.1. So, if $j_t(B_t)$ is the field output after interaction with a system, can it be “fed into” another quantum system, and can QSDEs describe this quantum network? Yes and yes.

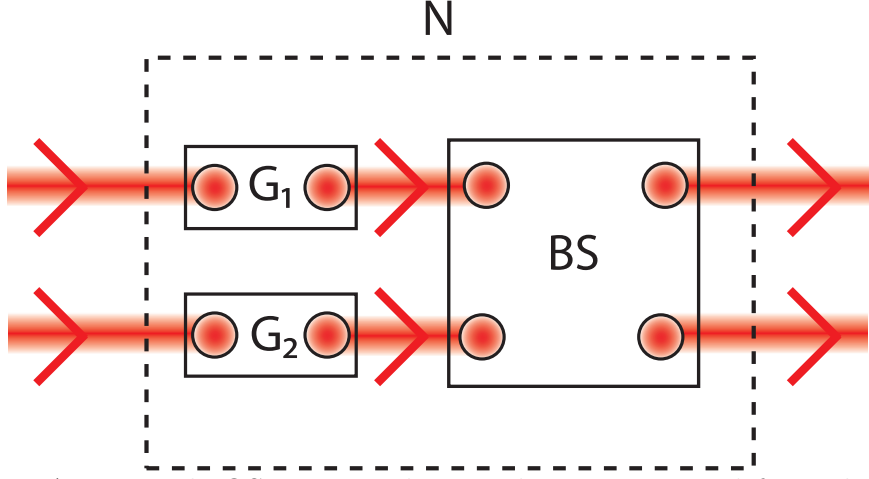


Figure 1.2: An example QSDE optical network N constructed from the series and parallel connection of QSDE subsystems G_1 , G_2 , and BS : $N = BS \triangleleft G_1 \boxplus G_2$.

Suppose the “first” system is characterized by a typical QSDE propagator, $U_t^{(1)}$ (Eq. (1.24)), specified by the set of coupling and Hamiltonian operators $G_1 = (L_1, H_1)$. A “later” system, $U_t^{(2)}$, is specified by $G_2 = (L_2, H_2)$. The process of feeding the field, after its interaction with the first system immediately into a second (assuming any propagation delay is much less than the dynamical timescales of the system [GJ09a]) is modeled in the Heisenberg picture by infinitesimally propagating any operator first by $U_{[t+dt,t]}^{(2)}$ and then by $U_{[t+dt,t]}^{(1)}$ in infinite sequence (the Heisenberg picture essentially operates in “backwards” time). If we look just at the first infinitesimal propagator [GJ09b, SSM08, GZ04]

$$U_{dt}^{(2)}U_{dt}^{(1)} = (I + dU_0^{(2)})(I + dU_0^{(1)}) \quad (1.29)$$

we can apply the quantum Ito rule to find

$$\begin{aligned} U_{dt}^{(2)}U_{dt}^{(1)} &= I + ((L_1 + L_2)dB_0^\dagger - (L_1 + L_2)^\dagger dB_0 - \\ &\quad (\frac{1}{2}(L_1^\dagger L_1 + L_2^\dagger L_2) + i(H_1 + H_2))dt - L_2^\dagger L_1 dt) \\ &= I + ((L_1 + L_2)dB_0^\dagger - (L_1 + L_2)^\dagger dB_0 - \\ &\quad (\frac{1}{2}(L_1 + L_2)^\dagger(L_1 + L_2) + i(H_1 + H_2 + \frac{1}{2i}(L_2^\dagger L_1 - L_1^\dagger L_2))dt)(1.30) \end{aligned}$$

A recursive analysis along these lines suggests that we may describe the evolution of this cascaded system with a single propagator $U_t^{(21)}$ propagated by the infinitesimal increment in Eq. 1.30. More abstractly, we define a *series product* [GJ09b]

$$G_{21} \equiv G_2 \triangleleft G_1 \equiv \left(L_1 + L_2, H_1 + H_2 + \frac{1}{2i}(L_2^\dagger L_1 - L_1^\dagger L_2) \right) \quad (1.31)$$

with its own, effective, coupling and Hamiltonian operators derived from the G_1 and G_2 subsystems. Note that the consequence of putting one system after another is essentially to couple their Hamiltonian dynamics. The ordering of the systems in the the series is subtly encoded in the sign of this coupling term.

With this approach in hand, we revisit the question of how to model the field produced by a laser if we are required to keep the bath in a vacuum state. First, recall from QED that a coherent state like the output of an ideal laser may be modeled as a *displaced vacuum* [WM08]. Thus, we can model a bath state with a coherent amplitude α at times $[t, 0]$ as

$$|\alpha, t\rangle = \mathcal{T} \exp\left\{ \alpha \int_0^t dB_{t'}^\dagger - \alpha^\dagger \int_0^t dB_{t'} \right\} |vac\rangle \equiv W_t^{(\alpha)} |vac\rangle. \quad (1.32)$$

From Eq. (1.32), we now have a new unitary operator called the *Weyl operator* that has the differential form

$$dW_t^{(\alpha)} = \left(\alpha dB_t^\dagger - \alpha^\dagger dB_t - \frac{1}{2} |\alpha|^2 dt \right) W_t^{(\alpha)}. \quad (1.33)$$

If we want to analyze the dynamics of an open quantum system probed by a laser, we can still use all our QSDE machinery by modeling the “laser” as a QSDE system that takes the vacuum as input, displaces it by α using $W_t^{(\alpha)}$, and then feeds its output field into the system of interest. That is, in our QSDE formalism a quantum system interacting with the vacuum, $G_0 = (L, H)$, is related to the same system probed by a laser with amplitude α by [KNPM10]

$$G_\alpha = G_0 \triangleleft W^{(\alpha)} = (L + \alpha, H + \frac{i}{2}(\alpha L^\dagger - \alpha^\dagger L)). \quad (1.34)$$

1.5 Multiple fields

In addition to connecting systems in series, it is possible to connect them in parallel, as depicted in Fig. 1.2. In fact, this is a more straightforward concept. We simply assume the existence of multiple input fields, each of which must also have an output. Physically, these fields may be any other free optical mode somehow orthogonal to the others due to polarization, frequency, spacial mode, etc. Individual systems may also have multiple field inputs (and an equal number of outputs). In this generalization, each process must carry an index specifying to which mode it is associated. However, the gauge process becomes particularly interesting in this generalization. If both $b_i(t)$ and $b_j(t)$ are quantum noise processes, indexed to modes i and j , then we define

$$\Lambda_t^{ij} \equiv \int_0^t d\Lambda_t^{ij} \equiv \int_0^t dt b_i^\dagger(t) b_j(t). \quad (1.35)$$

Because of this, gauge processes may now scatter field inputs between the outputs (e.g. be used in the modeling of a beamsplitter). With multiple fields present, the index of each field enters the quantum Ito table 1.1 in a straightforward manner. We also define a more generalized propagator that evolves multiple fields, and may describe a scattering among them [GJ09b, KNPM10]

$$dU_t = \sum_{j,k} \left((S_{jk} - \delta_{jk}) d\Lambda_t^{jk} + L_j dB_t^{j\dagger} - L_j^\dagger S_{jk} dB_t^k - (iH + \frac{1}{2} L_j^\dagger L_j) dt \right) U_t, \quad U_0 = I \quad (1.36)$$

where the *scattering matrix* S is necessarily unitary, and whose elements may be system operator-valued. Thus, our set of characteristic operators for a system used in the previous section must be expanded and generalized to be the set of operator arrays $G = (\vec{S}, \vec{L}, H)$. As an example, a beamsplitter (which only scatters fields and has no internal dynamics) is modeled as

$$BS = \left(\left[\begin{array}{cc} \alpha & -\beta^\dagger \\ \beta & \alpha^\dagger \end{array} \right], 0, 0 \right) \quad (1.37)$$

where $|\alpha|^2 + |\beta|^2 = 1$. Given this, individual QSDE components may be placed in parallel using the *concatenation product*

$$G_1 \boxplus G_2 = \left(\left[\begin{array}{cc} S_1 & 0 \\ 0 & S_2 \end{array} \right], \left[\begin{array}{c} L_1 \\ L_2 \end{array} \right], H_1 + H_2 \right) \quad (1.38)$$

The introduction of the scattering matrix also requires our definition of the series product to be slightly modified to account for field scattering. Namely, we have

$$G_2 \triangleleft G_1 = \left(S_2 S_1, L_2 + S_2 L_1, H_1 + H_2 + \frac{i}{2} (L_1^\dagger S_2^\dagger L_2 - L_2^\dagger S_2 L_1) \right) \quad (1.39)$$

1.6 Adiabatic elimination with QSDEs

Although the Markov approximation in section 1.1 yields a dramatically simpler (but typically extremely accurate) description of the system-bath coupling dynamics, many QSDE descriptions are still quite complex. In traditional quantum optics, it is sometimes appropriate to simplify open quantum systems by invoking a separation of time-scales principle to *adiabatically eliminate* fast dynamical variables that do not affect slower quantities of interest [Gar04, Sto06]. This technique has been adopted into the QSDE literature with an algorithm that calculates an approximate propagator U_t that converges to the exact propagator $U_t^{(k)}$ in a very strong sense [BvHS08]

$$\lim_{k \rightarrow \infty} \sup_{0 \geq t \geq T} \|(U_t^{(k)} - U_t)|\psi\rangle\| = 0, \quad (1.40)$$

for all $|\psi\rangle$ in the domain of the ‘slow’ dynamical subspace, where k is a parameter that scales with the fast dynamical rates. The theorem that guarantees this strong convergence assumes that the operator coefficients that define a stochastic integral of the form Eq. (1.36) for $U_t^{(k)}$ scale with k in a particular way

$$-(iH^{(k)} + \frac{1}{2} \sum_l L_l^{(k)\dagger} L_l^{(k)})^\dagger = k^2 Y + kA + B, \quad L_i^{(k)\dagger} = kF_i + G_i, \quad (S_{ji}^{(k)})^\dagger = W_{ij}. \quad (1.41)$$

Define P_0 as the projector onto the slow dynamical subspace, P_1 the projector onto the complement subspace, and assume that there exists a \tilde{Y} such that $\tilde{Y}Y = Y\tilde{Y} = P_1$. Given this scaling, and some structural domain requirements, the limit theorem is guaranteed for an approximate propagator U_t that is also a stochastic integral of the form Eq. (1.36) with operator coefficients [BvHS08]

$$\begin{aligned}
 - (iH + \frac{1}{2} \sum_l L_l^\dagger L_l)^\dagger &= P_0(B - A\tilde{Y}A)P_0, & (S_{ji})^\dagger &= \sum_l P_0 W_{il} (F_l^\dagger \tilde{Y} F_j + \delta_{lj}) P_0 \\
 L_i^\dagger &= P_0(G_i - A\tilde{Y}F_i)P_0, & (L_j^\dagger S_{ji})^\dagger &= \sum_j P_0 W_{ij} (G_j^\dagger - F_j^\dagger \tilde{Y} A) P_0
 \end{aligned} \tag{1.42}$$

Readers familiar with the adiabatic elimination procedure common in the quantum optics literature should see a clear parallel between the form of the approximate dynamics derived with that approach [Gar04, Sto06] and the approximate QSDE defined by Eqs. (1.42). This adiabatic elimination theorem has been essential in my quantum network projects [KNPM10, KPCM11], yielding excellent approximate models that isolate the critical dynamics we are interested in and require a simulation space orders of magnitude smaller than that of the full physical model.

Chapter 2

Optical measurements and state estimation

Any physical system obeys continuous time laws. The optical measurements we make in a quantum optics lab are also continuous. Thus we gain knowledge about the system we are measuring as it is evolving. In turn, by the postulates of quantum mechanics, the dynamics of the system we are observing must be perturbed by our measurement record. The continuous interplay of Hamiltonian and measurement dynamics is naturally described in a QSDE context and is what gives the approach much of its utility.

2.1 Optical measurement

2.1.1 Photon counting

As we interpret the $b(t)$ quantum noise objects as time-domain annihilation operator densities on a free field (Eq. (1.7)), it is reasonable to claim that the gauge process operator Eq. (1.13)

$$\Lambda_t = \int_0^t b^\dagger(t)b(t)dt \tag{2.1}$$

is an observable that counts the number of photons in the field over the time interval $(0, t]$ [Bar90, Car93a, GZ04, BvHJ07]. We can measure this operator experimentally by shining the field on a photodetector for this time interval and then reading off the total number of photons it received over the interval (as in the depiction in Fig. 1.1); that they were received within the interval is the only information we have about the arrival times of the photons. This procedure is known as photon counting.

In the Heisenberg picture, the photon counting operator evolves in time according to the global propagator Eq. (1.36)

$$U_t^\dagger \Lambda_t U_t = j_t(\Lambda_t) \equiv Y_t^\Lambda. \quad (2.2)$$

The infinitesimal increment of Y_t^Λ is obtained by the quantum Ito rule

$$dY_t^\Lambda = d\Lambda_t + j_t(L)dB_t^\dagger + j_t(L^\dagger)dB_t + j_t(L^\dagger L)dt, \quad (2.3)$$

and reapplying the rule, it immediately follows that $(dY_t^\Lambda)^2 = dY_t^\Lambda$ [BvHJ07, GZ04]. This tells us that each infinitesimal increment is an observable with eigenvalues of only 0 and 1, supporting the intuition that while Y_t^Λ may count the number of photons in an extended interval, dY_t^Λ counts the number of photons incident on a detector in a very small segment of time (i.e. so small that the probability of collecting >1 photons is negligible). The expectation of this increment (in the vacuum field state) is $\langle dY_t \rangle = \langle j_t(L^\dagger L) \rangle dt$, indicating that photon counting is useful as an indirect measurement of the system's $L^\dagger L$ operator.

From the definition of Λ_t (2.1) in terms of the noise processes $b(t)$ it may be easily seen that $[\Lambda_t, \Lambda_s] = 0$ for all t and s . More than this, though, due to the adaptedness (section 1.2) of Λ_t , $Y_t^\Lambda = U_t^\dagger \Lambda_t U_t = U_s^\dagger \Lambda_t U_s$ for all $s \geq t$. Thus, $[Y_t^\Lambda, Y_s^\Lambda] = 0$ for all t and s as well. This is the very important *self-nondemolition* property of photocounting measurements of field outputs [BvHJ07]. This property is an expression of the physically obvious notion that it is possible to build an experiment that counts the photons up to time t and also counts them up to time s , and that we can speak of the joint statistics of the results from both measurements. For example, if they didn't commute, a joint operator of these observables $Y_t^\Lambda Y_s^\Lambda$ wouldn't even be an observable

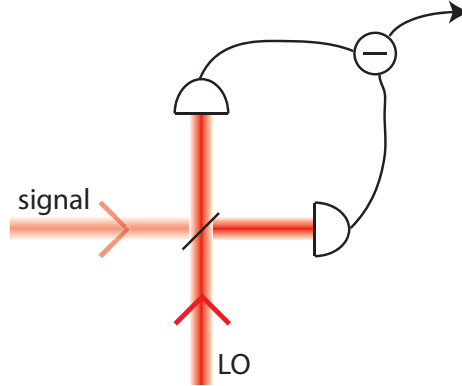


Figure 2.1: A depiction of optical homodyne detection. A signal mode is interfered with a strong local oscillator (LO) beam on a 50/50 beamsplitter. The two outputs of the beamsplitters are monitored with photodetectors and their photocurrents subtracted.

(e.g. $(Y_t^\Lambda Y_s^\Lambda)^\dagger = Y_s^{\Lambda\dagger} Y_t^{\Lambda\dagger} = Y_s^\Lambda Y_t^\Lambda \neq Y_t^\Lambda Y_s^\Lambda$), and clearly couldn't have any measurement statistics. Because Y_t^Λ and Y_s^Λ commute, we can talk of these observables having joint statistics. Similarly, it is straightforward to show that $[j_t(X), Y_s^\Lambda] = 0$ for all $s \leq t$, with X being any operator of the localized system (and thus commutes with field observables like Λ_t). This is called the *nondemolition* property of photoncounting. $[j_t(X), Y_s^\Lambda] = 0$ is not generally true when $s > t$. The nondemolition property will allow us to speak of *future* system observables as also having joint statistics with the measurements we have already made [BvHJ07].

2.1.2 Homodyne measurement

There is another common type of optical measurement that is also naturally modeled in the QSDE formalism. Homodyne detection consists of interfering a field signal with a strong, co-resonant, coherent ‘local oscillator’ (LO) field on a 50-50 beamsplitter, as depicted in Fig. 2.1. Photodetectors then monitor the two beamsplitter outputs and their photocurrents are subtracted [Bar90, Car93a, WM93, GZ04, BvHJ07]. This type of measurement has the effective operator

$$Y_t^W = U_t^\dagger (e^{-i\phi} B_t + e^{i\phi} B_t^\dagger) U_t, \tag{2.4}$$

for some relative optical phase ϕ between the local oscillator and signal fields, defining the *quadrature* of the homodyne measurement. We can use our series and concatenation products (sections 1.4 and 1.5), and our definition of photodetection to see why this is a physically reasonable measurement model. Notice that we can describe this quantum network of fields, local oscillators and beamsplitters as

$$G_{\text{homodyne}} = BS \triangleleft (G \boxplus W^{(\alpha)}) = \left(\frac{1}{\sqrt{2}} \begin{bmatrix} 1 & 1 \\ -1 & 1 \end{bmatrix}, \frac{1}{\sqrt{2}} \begin{bmatrix} L + \alpha \\ L - \alpha \end{bmatrix}, H \right) \quad (2.5)$$

where $G = (I, L, H)$ is the system we seek to measure. The measurement operator associated with our homodyne detection is now $Y_t^{\Lambda 1} - Y_t^{\Lambda 2}$ which subtracts the photon counts measured in one beamsplitter output from the other. This operator has the increment

$$\begin{aligned} dY_t^{\Lambda 1} - dY_t^{\Lambda 2} &= d\Lambda_t^{11} - d\Lambda_t^{22} + \frac{1}{\sqrt{2}} j_t(L + \alpha) dB_t^{1\dagger} - \frac{1}{\sqrt{2}} j_t(L - \alpha) dB_t^{2\dagger} + \\ &\quad \frac{1}{\sqrt{2}} j_t(L + \alpha)^\dagger dB_t^1 - \frac{1}{\sqrt{2}} j_t(L - \alpha)^\dagger dB_t^2 + j_t(\alpha^\dagger L + \alpha L^\dagger) dt \end{aligned} \quad (2.6)$$

In the limit that $\alpha = |\alpha|e^{i\phi}$ is very large (compared to either the vacuum fluctuations or L times them) this becomes

$$\begin{aligned} dY_t^{\Lambda 1} - dY_t^{\Lambda 2} &= \frac{1}{\sqrt{2}} |\alpha| e^{i\phi} j_t \left(dB_t^{1\dagger} + dB_t^{2\dagger} \right) + \frac{1}{\sqrt{2}} |\alpha| e^{-i\phi} j_t \left(dB_t^1 + dB_t^2 \right) + \\ &\quad |\alpha| j_t (e^{-i\phi} L + e^{i\phi} L^\dagger) dt, \end{aligned} \quad (2.7)$$

which, up to a multiplicative factor of $|\alpha|$ and “undoing” the beamsplitter’s coherent scattering of the fields (i.e. a simple change of free field bases) is exactly what one gets for

$$dY_t^W = e^{i\phi} dB_t^\dagger + e^{-i\phi} dB_t + j_t(e^{-i\phi} L + e^{i\phi} L^\dagger) dt; \quad (2.8)$$

the two measurements are informationally equivalent.

Importantly, it can also be shown that homodyne detection satisfies the self-nondemolition property and the nondemolition property. However, $[Y_t^\Lambda, Y_s^W] \neq 0$

$\forall t, s$, which means that the joint statistics of homodyne and photocounting measurements are ill-defined on overlapping time intervals, or more concretely, in a single experiment, we can only choose one type of measurement on a given free field over a given time interval (again, a physically sensible notion). Nor do homodyne measurements of a given ϕ -quadrature commute with any other homodyne measurement of a different quadrature over the same time interval. Also, it is straightforward to show that in the case of homodyne measurement $(dY_t)^2 = dt$ and $\langle Y_t^W \rangle = \langle j_t(e^{-i\phi}L + e^{i\phi}L^\dagger) \rangle$ [BvHJ07]. Together, these properties give Y_t^W the appearance of Brownian motion (section 1.2), plus a deterministic drift determined by the coupling operators L .

2.1.3 Calculating photocurrent statistics

While it is immediately clear how to calculate the expectation of an optical measurement increment $\langle dY_t^{(W,\Lambda)} \rangle$ in the QSDE formalism, calculating the joint statistics of measurements, e.g. $\langle dY_t^W dY_s^W \rangle$, takes a bit more effort [WM93]. There are various ways of calculating continuous measurement correlation functions, but QSDEs admit an elegant approach based on characteristic functionals [Bar90, GZ04]. As the vast majority of the experiments and theoretical work in this thesis utilize homodyne measurements, this technique will be demonstrated for homodyne measurements alone, and so I will drop the W superscript and write Y_t as the optical measurement operator. This section is written more as an explanation of calculations presented later in the thesis, and thus has a different motivation than the pedagogical explanation of the QSDE formalism in the preceding and succeeding sections. These technical descriptions are a bit more involved.

Consider the functional [GZ04]

$$\Phi_T[k] = \langle \exp\{i \int_0^T k(s) dY_s\} \rangle \equiv \langle U_T^\dagger V_T[k] U_T \rangle \quad (2.9)$$

where $k(s)$ is an arbitrary function of s , and dY_s is the homodyne measurement increment. Now note that for $t_1 < \dots < t_n < T$ and using the functional derivative

we get

$$\begin{aligned} -i \frac{\partial}{\partial k(t_1)} \Phi_T[k] \Big|_{k=0} &= \langle \frac{dY_{t_1}}{dt} \rangle \equiv \langle I_{t_1} \rangle \\ (-i)^n \frac{\partial^n}{\partial k(t_1) \dots \partial k(t_n)} \Phi_T[k] \Big|_{k=0} &= \langle I_{t_1} \dots I_{t_n} \rangle, \end{aligned} \quad (2.10)$$

where I_t may be thought of as the *photocurrent* operator (i.e. the rate of change in Y_t). Thus, we can use the characteristic functional $\Phi_T[k]$ to find all moments of the photocurrent correlations. We can propagate $\Phi_t[k]$ in time by first defining the reduced characteristic operator $\chi_t[k] = \text{Tr}_b[V_t[k]U_t\rho U_t^\dagger]$, in which $\rho = \rho_s \otimes \rho_{vac}$ is the global system state and the trace is over the bath subsystem only. It follows that $\Phi_t[k] = \text{Tr}_s[\chi_t[k]]$ and $\chi_t[0] = \text{Tr}_b[U_t\rho U_t^\dagger]$ (i.e. $\chi_t[0]$ is the reduced density matrix at time t of the system alone). Choosing for demonstration purposes the $\phi = 0$ case (i.e. amplitude quadrature measurement), the QSDE representation of $V_t[k]$ is then

$$dV_t[k] = \left\{ ik(t)(dB_t + dB_t^\dagger) - \frac{1}{2}k(t)^2 \right\} V_t[k] \quad (2.11)$$

and it follows that

$$\frac{d}{dt}\chi_t[k] = \mathcal{L}\chi_t[k] - \frac{1}{2}k(t)^2\chi_t[k] + ik(t)(L\chi_t[k] + \chi_t[k]L^\dagger), \quad \chi_0[k] = \text{Tr}_b[\rho], \quad (2.12)$$

where \mathcal{L} is the Lindblad generator from the master equation Eq. (1.27). Moreover, note that this is a completely deterministic, ‘master equation-like’ equation of motion for the measurement characteristic operator. Now using Eq. (2.12), we can find the expected photocurrent at time t

$$\begin{aligned} \langle I_t \rangle &= -i \frac{\partial}{\partial k(t)} \Phi_T[k] \Big|_{k=0} = -i \text{Tr}_s \left[\frac{\partial}{\partial k(t)} \chi_T[k] \right] \Big|_{k=0} \\ &= -i \text{Tr}_s \left[\frac{\partial}{\partial k(t)} \int_0^T \left(\left(\mathcal{L} - \frac{1}{2}k(s)^2 \right) \chi_s[k] + ik(s)(L\chi_s[k] + \chi_s[k]L^\dagger) \right) ds \right] \Big|_{k=0} \\ &= \text{Tr}_s[(L + L^\dagger)\chi_t[0]], \end{aligned} \quad (2.13)$$

as well as the photocurrent correlation function (let $t < t' < T$)

$$\begin{aligned}
 \langle I_{t'} I_t \rangle &= -\frac{\partial^2}{\partial k(t') \partial k(t)} \Phi_T[k] \Big|_{k=0} \\
 &= -\frac{\partial^2}{\partial k(t') \partial k(t)} \text{Tr}_s \left[\mathcal{T} \exp \left\{ \int_0^T \left(\mathcal{L} - \frac{1}{2} k(s)^2 + ik(s) \mathcal{J} \right) ds \right\} \chi_0[k] \right] \Big|_{k=0} \\
 &= -\frac{\partial}{\partial k(t')} \text{Tr}_s \left[\mathcal{T} \exp \left\{ \int_0^T \left(\mathcal{L} - \frac{1}{2} k(s)^2 + ik(s) \mathcal{J} \right) ds \right\} \times \right. \\
 &\quad \left. (-k(t) + i\mathcal{J}) \chi_t[k] \right] \Big|_{k=0} \\
 &= \text{Tr}_s [\delta(t' - t) \exp\{\mathcal{L}T\} \chi_0[0] + \exp\{\mathcal{L}(T - t')\} \mathcal{J} \exp\{\mathcal{L}(t' - t)\} \mathcal{J} \chi_t[0]] \\
 &= \delta(t' - t) + \text{Tr}_s [\mathcal{J} \exp\{\mathcal{L}(t' - t)\} \mathcal{J} \chi_t[0]] \tag{2.14}
 \end{aligned}$$

where $\mathcal{J}\rho = L\rho + \rho L^\dagger$, \mathcal{T} is the time-ordering operator and we have used the fact that the Lindblad operator is trace-preserving. With Eq. (2.12), all higher order photocurrent correlations are similarly calculable. Although the calculations themselves may be a bit opaque on a first read, note that the photocurrent expectation and correlation functions have an intuitive final form. The expectation of the amplitude quadrature photocurrent is simply the expectation of the ‘‘amplitude quadrature’’ of the system, $L + L^\dagger$, at time t . The two-time autocorrelation function is produced by a combination of optical ‘shot noise’ ($\delta(t' - t)$) and another term that applies the *measurement jump* super-operator \mathcal{J} at time t , evolves the system unconditionally until t' (via $\exp\{\mathcal{L}(t' - t)\}$), and then applies the measurement operator again before finally taking the expectation. Eq. (2.14) was the basis for the theoretically predicted photocurrent statistics used in Fig. 6.5.

Rather than consider the autocorrelation of instantaneous photocurrents, it is more practically useful to consider the small, but not infinitesimal changes to the measurement record over small, but not infinitesimal time intervals. This models a realistic experimental situation where photocurrents are measured with a finite bandwidth, or in our approximation, simply integrated over small time intervals $(0, \tau]$. The approach adapts the above characteristic functional approach to give a 2D representation of the finite bandwidth photocurrents expected from homodyne measurements of an arbitrary quadrature [Bar90], essentially producing a Wigner quasi-probability

representation [WM08] of realistic photocurrent observables. This representation is given by the function

$$\begin{aligned} W(\beta) &= \frac{1}{\pi^2} \int d^2\alpha e^{\beta\alpha^\dagger - \beta^\dagger\alpha} \Phi_\tau(\alpha); & \Phi_\tau(\alpha) &\equiv \langle U_\tau^\dagger V_\tau(\alpha) U_\tau \rangle; \\ V_\tau(\alpha) &\equiv \mathcal{T} \exp\{\alpha B_\tau^\dagger - \alpha^\dagger B_\tau\} \end{aligned} \quad (2.15)$$

where α and β are c-numbers. Going beyond the suggestive looking construction of $W(\alpha)$, to demonstrate why this is like a W-function for homodyne measurements, we can integrate the function over its imaginary axis:

$$\int d\beta_i W(\beta) = \frac{1}{\pi} \int d\alpha_i \langle \mathcal{T} e^{2i\alpha_i(\frac{1}{2}Y_\tau - \beta_r)} \rangle = \langle \delta(\frac{1}{2}Y_\tau - \beta_r) \rangle \quad (2.16)$$

(where β_i and β_r are the real and imaginary components of β , etc.), which gives the expectation of the observable that indicates whether amplitude quadrature measurement yields a $2\beta_r$ measurement result, in complete analogy to a Wigner function [WM08]. In much the same way, we calculate $W(\beta)$ by defining a $\chi_\tau(\alpha) = \text{Tr}_b[V_\tau(\alpha)U_t\rho U_t^\dagger]$ and finding its equation of motion

$$\frac{d}{dt}\chi_\tau(\alpha) = (\mathcal{L} - \frac{1}{2}|\alpha|^2 + \mathcal{J}(\alpha))\chi_\tau(\alpha); \quad \mathcal{J}(\alpha)\chi = \alpha\chi L^\dagger - \alpha^\dagger L\chi. \quad (2.17)$$

This means we can write

$$\begin{aligned} \chi_\tau(\alpha) &= e^{\tau(\mathcal{L} - \frac{1}{2}|\alpha|^2 + \mathcal{J}(\alpha))} \chi_0 = e^{\tau(\mathcal{L} - \frac{1}{2}|\alpha|^2 - 2i\alpha_r\mathcal{J}_i + 2i\alpha_i\mathcal{J}_r)} \chi_0 \\ \mathcal{J}_r\chi &= \frac{1}{2}(\chi L^\dagger + L\chi); \quad \mathcal{J}_i\chi = \frac{i}{2}(\chi L^\dagger - L\chi); \quad [\mathcal{J}_i, \mathcal{J}_r] = 0 \end{aligned} \quad (2.18)$$

where $\chi_0 = \text{Tr}[U_t\rho U_t^\dagger]$. Although everything thus far has been exact, and representations for time intervals $(0, \tau]$ of arbitrary length are valid, calculation of $W(\beta)$ at this stage would be highly numerical in most cases. However, if our detection bandwidth $\sim \tau^{-1}$ is fast enough, we should be able to ignore the internal, unconditional evolution of the system over the sampling time of the detector and approximate $\mathcal{L}\tau \approx 0$. With

this restriction in hand, we can use familiar non-commutative calculus to find

$$W(\beta) = \frac{2}{\pi\tau} \text{Tr}_s[e^{-\frac{2}{\tau}|L-\beta|^2} \chi_0] \quad (2.19)$$

which is very satisfying!

Why is this satisfying? It has an intuitive connection to the Wigner function *for infinitely strong measurements* of the system operators L we are indirectly probing with our homodyne field measurements. First, for simplicity assume we work with a scaling such that L and τ are unitless. It can be shown that this strong measurement Wigner function is [WM08]

$$W_{s,strong}(\beta_s) = \frac{2}{\pi} \text{Tr}[e^{-2|L-\beta_s|^2} \chi_0] \quad (2.20)$$

where the subscript s indicates units of the system “amplitude” (i.e. the range of L -quadrature measurements). Through a simple change of variables, we can translate Eq. (2.19) into these units:

$$W(\beta) \rightarrow W_s(\beta_s) = \frac{2}{\pi} \text{Tr}[e^{-2|\sqrt{\tau}L-\beta_s|^2} \chi_0] \quad (2.21)$$

which is equivalent to the strong measurement, but with ‘collection efficiency’ $\sqrt{\tau}$. This can be seen by considering extending the system to include some other vacuum mode $\chi_0 \rightarrow \chi_0 \otimes |vac\rangle\langle vac|$ and taking $L \rightarrow \sqrt{\tau}L + \sqrt{1-\tau}a_{vac}$ which also acts like an annihilation operator on the vacuum mode. With this extension $W_{s,strong}(\beta_s)$ is modified into $W_s(\beta)$. Moreover, as we are assuming high bandwidth detection (so that the collection efficiency $\tau < 1$), we can calculate the photocurrent’s Wigner function representation $W_s(\beta_s)$ directly from $W_{s,strong}(\beta_s)$ by noting that

$$W_s(\beta_s) = \frac{1}{\sqrt{\tau}} W_{s,strong}\left(\frac{\beta_s}{\sqrt{\tau}}\right) * \frac{1}{\sqrt{1-\tau}} W_v\left(\frac{\beta_s}{\sqrt{1-\tau}}\right); \quad W_v(\beta_s) = \frac{2}{\pi} e^{-2|\beta_s|^2}, \quad (2.22)$$

that is, the photocurrent Wigner function is simply the convolution of the strong one with the Wigner function of a vacuum. This approach was the basis for the 2D photocurrent representations and marginal quadrature distributions shown in Figs.

4.5 and 6.3.

2.2 Quantum trajectories

Photocurrent correlation functions may contain a complete description of I/O dynamics, but they don't give a visceral sense of what these optical measurements look like on an oscilloscope. How can we construct typical measurement trajectories? At any given time, we already know that the expectation of the next photocurrent increment is $\langle dY_t \rangle = \langle L + L^\dagger \rangle_t dt$ (Eq. (2.13)) where the expectation is taken according to the state at time t , and that $(dY_t)^2 = dt$ (apply the quantum Ito rule to Eq. (2.8)). With these two facts, the spectral theorem and Levy's theorem together tell us that the quantity

$$\int_0^t dM_s - \int_0^t \langle L + L^\dagger \rangle_s ds, \quad (2.23)$$

where dM_t/dt is some photocurrent measurement sequence, is simple Brownian motion [BvHJ07], or in other words, that

$$dM_t = \langle L + L^\dagger \rangle_t dt + dW_t \quad (2.24)$$

where dW_t is the increment of the Brownian motion process (a Gaussian-distributed random variable). So far these arguments are very loose. For instance, we can't yet say what the state is at time t . If we have been making continuous homodyne measurements up to t , the state is conditioned on the entire measurement sequence up to time t , according to the postulates of quantum mechanics. The derivation of the *conditional* expectation $\langle L + L^\dagger \rangle_c$ has been described by many other authors in more rigorous contexts [Car93a, GZ04, GPZ92, SD81, WM93], most elegantly as a continuous-time conditioning procedure derived from Bayes rule known as *quantum filtering* [BvHJ07, vH07]. Again, a proper derivation is quite mathematical and is framed in terms of probability rather than physical theories. Rather than simply reiterate these derivations (which would take a long time), I feel it is more valuable to try to offer a heuristic explanation for interested physicists.

2.2.1 The stochastic Schrödinger equation

If we have a global system state that is initially $|\Psi_0\rangle = |\psi_s, vac_b\rangle$ – the system is in some state $|\psi_s\rangle$ and the free field that interrogates it is in the vacuum state – the Schrödinger equation tells us that (using Eq. 1.24)

$$d|\Psi_t\rangle = \left(-(iH + \frac{1}{2}L^\dagger L)dt + LdB_t^\dagger - L^\dagger dB_t \right) |\Psi_t\rangle. \quad (2.25)$$

Recall that from our definition of the noise increments, $dB_t|\Psi_t\rangle = 0$ for all t , that is, dB_t annihilates the state as it acts on the ‘incoming’ segment of the vacuum field at time t . This means we can change the coefficient in front of dB_t in (2.25) almost freely without affecting the global dynamics. For example, it is also true that [BvHJ07]

$$\begin{aligned} d|\Psi_t\rangle &= \left(-(iH + \frac{1}{2}L^\dagger L)dt + L(dB_t^\dagger + dB_t) \right) |\Psi_t\rangle \\ &\equiv \left(-(iH + \frac{1}{2}L^\dagger L)dt + LdY_t^S \right) |\Psi_t\rangle \end{aligned} \quad (2.26)$$

where $Y_t^S = B_t^\dagger + B_t$ is the amplitude quadrature homodyne observable in this Schrödinger picture. As every dY_s^S commutes with every dY_t^S (the self-nondemolition property in section 2.1.2), these operators may be simultaneously diagonalized. The diagonal elements of dY_t^S are simply the possible photocurrent increments dM_t at time t . In principle any measurement increment from $(-\infty, \infty)$ is possible, but only a narrow range of increments are reasonably probable, with a probability function set by $|\Psi_t\rangle$. The diagonal elements are indexed by every possible *entire* measurement sequence $\{dM_0, \dots, dM_t\}$.

By the projection postulate, if we observe a particular measurement sequence $\{dM_0, \dots, dM_t\}$, then the state $|\Psi_t\rangle$ is projected onto the subspace corresponding to that particular sequence (generally decreasing the norm, if not re-normalized). Correspondingly, for a particular measurement sequence, we may recursively construct

the unnormalized state of the system for all times $[0, t]$, conditioned on these measurements, using the *stochastic Schrödinger equation* [Car93a, GZ04, WM93]

$$d|\Psi_t\rangle_c = \left(-iH + \frac{1}{2}L^\dagger L \right) dt + L dM_t \Big|_{\Psi_t\rangle_c}, \quad (2.27)$$

where the conditional state $|\Psi_t\rangle_c$ is a state on the system only; we can think of the field state as being “projected away” by the measurements. This equation of motion may also be modified so that the conditional state maintains its normalization:

$$d|\Psi_t\rangle_c = \left((-iH - \frac{1}{2}L^\dagger L + \langle L^\dagger \rangle_c L + \frac{1}{2}|\langle L \rangle_c|^2) dt + (L - \langle L \rangle_c)(dM_t - \langle L^\dagger + L \rangle_c dt) \right) |\Psi_t\rangle_c \quad (2.28)$$

where $\langle X \rangle_c = \langle \Psi_t | X | \Psi_t \rangle_c$ is the conditional expectation. Although Eq. (2.28) propagates a proper quantum state, its nonlinearity in $|\Psi_t\rangle_c$ makes it very awkward to work with. In practice, Eq. (2.27) is more often used in simulations, with the state forcibly renormalized when necessary. While (2.28) is valid for initially pure states and perfectly efficient photodetection, if either of these conditions are not met, the conditional state must be described as a mixed state density matrix. The equation of motion for a conditional, normalized density matrix may be derived from (2.28)

$$d\rho_{t,c} = \mathcal{L}\rho_{t,c} dt + ((L - \langle L \rangle_c)\rho_{t,c} + \rho_{t,c}(L - \langle L \rangle_c)^\dagger) (dM_t - \langle L^\dagger + L \rangle_c dt) \quad (2.29)$$

where, again \mathcal{L} is the unconditional generator from Eq. (1.27). Note, though, that according to Eq. (2.24), the final terms in Eqs. (2.28) and (2.29) are equal to

$$dM_t - \langle L^\dagger + L \rangle_c dt = dW_t \quad (2.30)$$

where W_t is a Brownian motion process. In a sense, Eq. (2.30) expresses that $\langle L^\dagger + L \rangle_c$ is an optimal, unbiased estimate of the next measurement increment [BvHJ07]. Moreover, it is the dW_t deviation of the actual increment, dM_t , from the expected, $\langle L^\dagger + L \rangle_c dt$, that drives the stochastic aspect of these evolutions. dW_t is often referred to as the *innovation*, quantifying the ‘surprise’ in our measurement result. It is this

‘surprise’ that drives the stochastic evolution in Eq. (2.29); averaging over all possible innovation trajectories W_t , we simply acquire the unconditional, master equation dynamics for ρ_{uc} , as in Eq. (1.27).

Now we have a method for constructing photocurrent trajectories that we might actual see on the oscilloscope of a quantum optics experiment, sampled from the space of all possible measurement trajectories with the proper likelihoods. In each time step, we first calculate the next dM_t using the current $\rho_{t,c}$ and a randomly sampled value for dW_t (a Weiner increment, which has a Gaussian probability density function and generates the Brownian motion process W_t), according to (2.30). With this same value for dW_t , the conditional state $\rho_{t+dt,c}$ is updated according to (2.29). The next photocurrent increment is then constructed in the same way, using the latest conditioned state, and so on. Generalizations to imperfect detection efficiency are straightforward (section 5.2.4 in [vH07]). Quantum trajectory simulations are used throughout the following chapters (often using the *quantum optics toolbox* for MATLAB [Tan99]), but Figs. 4.5, 6.3, and 6.5 are particularly notable for comparing experimental and trajectory-simulated photocurrents with expected measurement ensembles derived from the methods in section 2.1.3.

Any powerful set of equations has multiple interpretations, and Eqs. (2.29) and (2.30) are powerful equations. If we have an experiment that produces a photocurrent trajectory $\{dM_0, \dots, dM_t\}/dt$, this sequence may serve as an *input* to Eq. (2.29), generating a sequence of conditional states $\rho_{t,c}$ that track the evolution of the isolated system. This conditional state may be used to track the expectations of operators that act on this system $\text{Tr}[X\rho_{t,c}] \equiv \pi_t(X)$, conditioned on our measurement sequence [BvHJ07, vH07]. This *quantum filter* function $\pi_t(\cdot)$ is optimal in the sense that, for example, it may be used as an unbiased estimator of the next dM_t/dt increment, using $\pi_t(L + L^\dagger)$ according to (2.30): $\pi_t(L + L^\dagger)$ filters the photocurrent sequence down to Gaussian (dW_t) residuals. Quantum filtering using (simulated) photocurrents as inputs is most directly employed in section 7.2.2.

Part II

Quantum ‘Bistability’ in Cavity QED

Introduction

A two-level system (TLS) interacting with an optical resonator mode via an electric dipole interaction has become one of the best studied quantum optical systems in the past two decades [MD02, Car93a, TRK92, MTCK96, BMB⁺04, EFZ⁺07, FSS⁺10, SBF⁺10]. For this simple system, the sum is far richer than its parts. On its own, an optical resonator is essentially a “classical” device: quantum mechanics may adequately describe the system, but classical models also suffice unless the cavity is driven by a non-classical field. A two-level atom is perhaps the canonical quantum system, but in isolation, the system was completely described in the earliest decades of quantum theory. Modern engineering has already provided us with a number of critical technologies based on (approximate) two-level atomic spins, notably NMR and atomic clocks. Many nonlinear optical systems may also be modeled as the interaction of light with atom ensembles. However, such well-known applications still rely on *ensembles* of quantum mechanical spins and typically admit semi-classical models for their interaction with electromagnetic radiation. When a single TLS couples to an optical cavity mode with a very small mode volume, and both sub-systems each couple weakly to all other free field modes, a fully quantum model is generally required to describe the dynamics of both the fixed (i.e. TLS and resonator) and free field degrees of freedom, even for completely classical input fields.

Chapter 3

The cQED model

This chapter introduces a standard model for cavity quantum electrodynamics (cQED) [MD02, Car93a] utilized in much of the remaining two parts. A single emitter with a transition coupled to and nearly degenerate with a micron-scale optical resonator properly requires a fully quantum I/O model to predict the evolution of its internal states and its effect on optical probe fields. This quantum model is described, but I also present a standard *semiclassical* approximation to the equations of motion. This approximation corresponds to an analogous cQED system with many atoms coupling strongly to the resonator in aggregate only. While the approximation fails in many respects to describe our experimental system [KAPM11, KAM10], it is not irrelevant and highlights the subtle dynamical transformations that occur as photonic devices approach microscopic scales.

3.1 The cQED master equation

The Hamiltonian

We adopt the Jaynes-Cummings model [Car93a, AM06] to describe the internal, Hamiltonian dynamics of our cQED system. Despite its dramatic simplifications of any experimentally realistic system, the model captures much of what's essential and interesting in atom-photon interactions, and experimental realizations that best

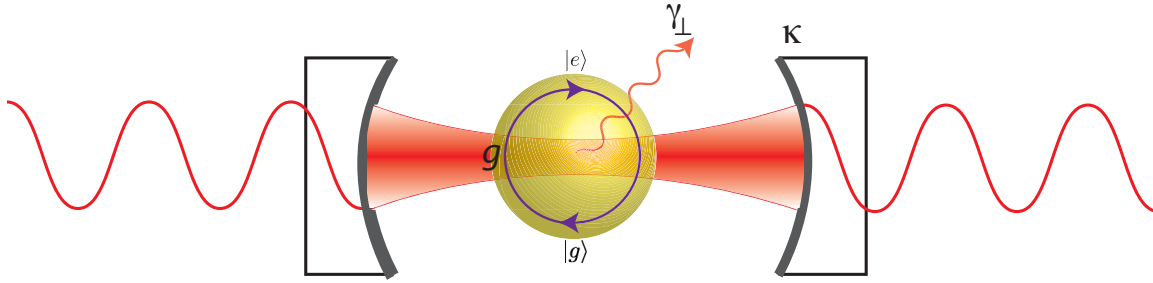


Figure 3.1: A depiction of the cavity quantum electrodynamics (cQED) I/O system. A single, two level atom couples with rate g (per $\sqrt{\text{photon}}$) to a single optical mode of a resonator, here shown as a Fabry-Perot cavity. Optical free fields may drive one side of the resonator and be transmitted through the other side via the highly reflective mirrors. The cQED system is thus coupled to various free optical fields: the cavity mode and the input-output (I/O) free fields with cavity field decay rate κ , and the atom and transverse free fields with the atom’s electronic dipole decaying at rate γ_{\perp} .

approximate this simplicity are often considered the most fruitful to study.

The “atom” (be it a real atom, like Cs [Ste], or a solid-state charge impurity, like a nitrogen vacancy center [BFSB09] or quantum dot [EFZ+07]) is a two-level system (TLS), with the natural basis states *ground* $|g\rangle$ and *excited* $|e\rangle$, so-named to reflect their association with the atom’s electronic ground state and a single excited state. The lab-frame energy associated with the two atomic states are 0 for the ground state and a fraction of an aJ for the excited (corresponding to the optical range of the EM spectrum, or several hundred THz). The single, optical cavity mode is modeled as a quantum simple harmonic oscillator (SHO), with a harmonic spectrum that also bestows single excitations (that is, photons) with optical energies. These models may be derived from fundamental QED, but doing so is beyond the scope of the chapter and is well-covered in many text books [CTDRG89, CTDRG92].

The Hamiltonians that describe the internal dynamics of the atom and cavity in isolation are thus $H_a = \omega_a \sigma^{\dagger} \sigma$ and $H_c = \omega_c a^{\dagger} a$, respectively, where $\sigma = |g\rangle\langle e|$ is the atomic *lowering operator*, a is the cavity *annihilation operator*, \dagger the hermitian conjugate, and ω_a and ω_c are the energies of the atom and cavity excitations, respectively ($\hbar = 1$ will be assumed throughout – except when experimental values are needed). In addition to this, the dynamics associated with a coherent free field

(i.e. a laser) driving the cavity may be modeled with an added Hamiltonian term [Car93a, CTDRG92] $H_d = i(\mathcal{E}a^\dagger e^{-i\omega_0 t} - \mathcal{E}^* a e^{i\omega_0 t})$, where \mathcal{E} is a c-number with $|\mathcal{E}|^2$ and $\arg(\mathcal{E})$ proportional to the photon flux and phase of the laser drive, respectively, and ω_0 is the optical frequency of the drive.

The interaction between the cavity mode and atom is modeled as an electric dipole interaction, or $H_{ed} = g\hat{d} \cdot \hat{E}$, where \hat{d} is the atomic dipole operator (i.e. a vector of Pauli-X and Pauli-Y operators in the $\{|g\rangle, |e\rangle\}$ basis), \hat{E} is electric field operator for the cavity field, and g quantifies the rate of energy exchange between the atom and field. However, it is common to invoke the rotating wave approximation for cQED systems (dropping terms that produce interaction dynamics at twice the excited state/photon energies), such that the interaction Hamiltonian simply becomes $H_i = ig(a^\dagger\sigma - a\sigma^\dagger)$, where the ‘phase’ of the interaction here is a convention and sets a reference phase for the system [Car93a, AM06].

Putting all the terms together, the Hamiltonian that describes the internal dynamics of the cQED system in the lab frame is

$$\begin{aligned} H_{lab} &= H_a + H_c + H_i + H_d \\ &= \omega_a \sigma^\dagger \sigma + \omega_c a^\dagger a + ig(a^\dagger \sigma - a \sigma^\dagger) + i(\mathcal{E} a^\dagger e^{-i\omega_0 t} - \mathcal{E}^* a e^{i\omega_0 t}). \end{aligned} \quad (3.1)$$

Dissipation dynamics

All experimental systems are *open quantum systems* [Car93a], meaning that at some point they must interact with the many-body, “classical” systems which may (e.g. photodetectors) or may not (e.g. brick walls) provide us with measurement results. Measurements always perturb quantum systems, but when measurements are made continuously, their effects become a critical aspect of the dynamical evolution. Even if an experimenter is not dutifully measuring every free field that interacts with the system with perfect efficiency (a practical impossibility), open system dynamics are fundamentally perturbed from a Hamiltonian evolution.

Under fairly general conditions of a weak and Markovian interaction with a zero temperature bath (like a freely-propagating optical field in a coherent state), the equation of motion for a quantum system’s *density matrix* ρ , unconditioned on any

measurement result, is described by the master equation (see section 1.3 and [Car93a, GZ04])

$$\frac{d}{dt}\rho = -i[H, \rho] + 2\tilde{\kappa}\mathcal{D}[\hat{O}]\rho, \quad (3.2)$$

where H is the system Hamiltonian,

$$\mathcal{D}[\hat{O}]\rho = \hat{O}\rho\hat{O}^\dagger - \frac{1}{2}\hat{O}^\dagger\hat{O}\rho - \frac{1}{2}\rho\hat{O}^\dagger\hat{O} \quad (3.3)$$

is a superoperator describing the system's coupling to the bath via operator \hat{O} and strength $\tilde{\kappa}$. Often, master equations like 3.2 are symbolically represented as

$$\dot{\rho} = \mathcal{L}\rho \quad (3.4)$$

where the *Lindblad* superoperator \mathcal{L} generates the entire unconditional evolution.

In our cQED system, two different bath couplings are significant: transverse radiation modes coupling to the atom (inducing spontaneous emission, for example), and two single free field modes coupling to the cavity mode via the two high reflectivity cavity mirrors (providing optical input and transmission channels). For interactions with uncorrelated baths like these, the unconditional dynamics may be simply aggregated, and the overall unconditional evolution in the lab frame becomes

$$\frac{d}{dt}\rho_{lab} = -i[H_{lab}, \rho] + 2\kappa\mathcal{D}[a]\rho_{lab} + 2\gamma_\perp\mathcal{D}[\sigma]\rho_{lab}, \quad (3.5)$$

where κ is the cavity field decay rate (such that each photon in the cavity leaks out at mean rate 2κ) and γ_\perp is the atomic dipole decay rate (such that an excited atom decays at mean rate $2\gamma_\perp$).

More convenient reference frames

The explicit time-dependence in H_{lab} is awkward to deal with. Consequently, it is typical to boost our model into an *interaction frame* that removes these terms from the Hamiltonian [CTDRG89, Arm09]. This is done by modeling the dynamics on the

state

$$\rho_{lab} \rightarrow T^\dagger \rho_{lab} T = \rho \quad (3.6)$$

where

$$T = e^{-i\omega_0(\sigma^\dagger \sigma + a^\dagger a)t}. \quad (3.7)$$

It follows from Eqs. (3.5), (3.6), and (3.7) that the unconditional dynamics in our new frame is

$$\frac{d}{dt}\rho = -i[H, \rho] + 2\kappa\mathcal{D}[a]\rho + 2\gamma_\perp\mathcal{D}[\sigma]\rho, \quad (3.8)$$

where

$$H = T^\dagger H_{lab} T + i\frac{\partial T^\dagger}{\partial t} T = \Delta\sigma^\dagger\sigma + \Theta a^\dagger a + ig(a^\dagger\sigma - a\sigma^\dagger) + i(\mathcal{E}a^\dagger - \mathcal{E}^*a) \quad (3.9)$$

where $\Delta = \omega_a - \omega_0$ and $\Theta = \omega_c - \omega_0$ describe the laser drive's detuning from the atomic transition and cavity resonance frequencies, respectively.

While most analyses may be conveniently done in the frame of Eq. (3.8), for computations it is often advantageous to apply yet another frame boost. Physically, this transformation corresponds to “displacing” the cavity field by some complex amplitude α such that a cavity coherent state with amplitude β becomes $\beta + \alpha$. This can be very convenient for canceling out large, DC cavity field amplitudes in simulations if we are only interested in relatively small fluctuations in these amplitudes, for example. The aptly named *displacement operator* [WM08, Arm09]

$$D(\alpha) = e^{\alpha a^\dagger - \alpha^* a} \quad (3.10)$$

induces this transformation of the frame: $\rho \rightarrow D(\alpha)^\dagger \rho D(\alpha) = \rho_\alpha$ as well as a corresponding transformation for the master equation.

3.2 The QSDE representation

While the master equation of Eq. (3.8) is extremely useful, it only tells part of the story. While it represents the “average” effect of a bath on the cQED system (under

appropriate approximations) [Car93a, GZ04], it doesn't speak to the effect of the quantum system on the bath fields that interact with it. If we are concerned with the I/O dynamics of the free fields interacting with cQED devices, this is a critical oversight!

A quantum stochastic differential equation (QSDE) representation of the the cQED system is convenient for rolling both internal and free-field aspects of the global system into a single, unified model. Given an initial state, the dynamics on this global system is described by the QSDE for the propagator (see chapter 1)

$$dU_t = \left\{ \sqrt{2\kappa} a dA_t^\dagger - \sqrt{2\kappa} a^\dagger dA_t + \sqrt{2\gamma_\perp} \sigma dB_t^\dagger - \sqrt{2\gamma_\perp} \sigma^\dagger dB_t - (iH - \kappa a^\dagger a - \gamma_\perp \sigma^\dagger \sigma) dt \right\} U_t, \quad U_0 = I \quad (3.11)$$

where dA_t and dB_t are QSDE annihilation processes ('quantum noise') on orthogonal free field modes. As described in more detail in Part I, in the QSDE representation, the internal cQED and external fields are on equal footing, so to speak. For example, one may analyze the dynamics of internal variables $j_t(X) = U_t^\dagger X U_t$ (in the Heisenberg picture; X some cQED operator)

$$dj_t(X) = j_t(\mathcal{L}^\dagger X) dt + \sqrt{2\kappa} \left(j_t([a^\dagger, X]) dA_t + j_t([X, a]) dA_t^\dagger \right) + \sqrt{2\gamma_\perp} \left(j_t([\sigma^\dagger, X]) dB_t + j_t([X, \sigma]) dB_t^\dagger \right), \quad (3.12)$$

where \mathcal{L}^\dagger is the superoperator adjoint of the (Schrödinger-picture) unconditional generator in equation (3.4), analogous to that in Eq. (1.26), and the dynamics of external field outputs, e.g. $j_t(A_t)$

$$dj_t(A_t) = \sqrt{2\kappa} j_t(a) dt + dA_t, \quad (3.13)$$

revealing intricate interrelations. Note that, in this system, the output field $j_t(A_t)$ looks an awful lot like a copy of the intracavity field, with added noise.

Similarly, dynamics conditioned on measurements of the free field outputs are also naturally derived with the QSDE representation, as in section 2.2.1. For example,

we may wish to infer the internal state of the cQED system, ρ_c , based on amplitude quadrature homodyne measurement of the optical field transmitted by a cQED device. Given a photocurrent record from time 0 to t , with integral M_t , the equation of motion for the conditional state can be shown to be (section 2.2.1)

$$d\rho_c = \mathcal{L}\rho_c dt + \sqrt{\eta}\sqrt{2\kappa} (a\rho_c + \rho_c a^\dagger - \langle a + a^\dagger \rangle_c \rho_c) \left(dM_t - \sqrt{\eta}\sqrt{2\kappa} \langle a + a^\dagger \rangle_c dt \right) \quad (3.14)$$

where η is the quantum efficiency of the detection, and $\langle \cdot \rangle_c$ is the conditional expectation at time t . Note that when $\eta = 0$, Eq. (3.14) is equivalent to the *unconditional* evolution Eq. (3.8). Moreover, it can be shown that

$$dW_t = dM_t - \sqrt{\eta}\sqrt{2\kappa} \langle a + a^\dagger \rangle_c dt \quad (3.15)$$

is a Wiener increment (section 2.2.1), and thereby the statistics of M_t are also completely determined by the model. Thus, a QSDE approach, through Eqs. (3.14) and (3.15) – and through the more elegant techniques of section 2.1.3 – is also naturally suited to analyzing optical measurements.

3.3 The Maxwell-Bloch equations

As noted in section 3.2, the output fields we are interested in are roughly noisy versions of the intracavity field. Thus, much intuition about the input-output dynamics of cQED devices may be gained by considering the equations of motion for expectations of internal cQED operators. For example, from the master equation (3.8), we find that

$$\begin{aligned} \langle \dot{a} \rangle &= -(\kappa + i\Theta) \langle a \rangle + g \langle \sigma \rangle + \mathcal{E} \\ \langle \dot{\sigma} \rangle &= -(\gamma_\perp + i\Delta) \langle \sigma \rangle + g \langle a \sigma_z \rangle \\ \langle \dot{\sigma}_z \rangle &= -2\gamma_\perp (\langle \sigma_z \rangle + 1) - 2g (\langle \sigma a^\dagger \rangle + \langle \sigma^\dagger a \rangle). \end{aligned} \quad (3.16)$$

where σ_z is the atomic Pauli-Z operator. Already, we see some important characteristic dynamics. For example, with $g \rightarrow 0$, the intracavity field amplitude $\langle a \rangle$ will decay to $\mathcal{E}/(\kappa + i\Theta)$ and the atom will decay to its ground state, $\langle \sigma_z \rangle \rightarrow -1$. The coupling

between the cavity and the atom introduces more complicated dynamics: the cavity field drives the atom (through terms like $g\langle a\sigma_z \rangle$) and the atomic dipole radiates its own field back into the cavity through the $g\langle \sigma \rangle$ term. However, it is impossible to say much more than this from Eqs. (3.16) alone, as they are not a closed set of equations for the operator expectations.

If we simply *factorize* compound expectations such as $\langle a\sigma_z \rangle \rightarrow \langle a \rangle \langle \sigma_z \rangle$, we arrive at a closed set of non-linear, deterministic dynamical equations known as the *Maxwell-Bloch equations* (MBE) [Lug84]

$$\begin{aligned}\langle \dot{a} \rangle &= -(\kappa + i\Theta)\langle a \rangle + g\langle \sigma \rangle + \mathcal{E} \\ \langle \dot{\sigma} \rangle &= -(\gamma_{\perp} + i\Delta)\langle \sigma \rangle + g\langle a \rangle \langle \sigma_z \rangle \\ \langle \dot{\sigma}_z \rangle &= -2\gamma_{\perp}(\langle \sigma_z \rangle + 1) - 2g(\langle \sigma \rangle \langle a^{\dagger} \rangle + \langle \sigma^{\dagger} \rangle \langle a \rangle).\end{aligned}\tag{3.17}$$

But *can* we do this? Not really. Factorization of cavity and atomic operator expectations returns the same expectation value only if there is no correlation between the states of the two subsystems. In a sense, the MBE represent a semiclassical approximation to the internal dynamics of a cQED system. More precisely, they model an atomic TLS, and also a *classical* cavity field characterized by a single, complex amplitude $\langle a \rangle$. It is difficult to specify exactly when the MBE are inaccurate at explaining cQED phenomena, but for a single atom cQED system with strong coupling between the cavity and atom – such as the experimental system described in this thesis – it is generally understood that the MBE provide accurate predictions in the “bad cavity limit” ($\kappa \gg g \gg \gamma_{\perp}$) and weak atomic excitation [Lug84, Car93b, ROKD91, RC88]– which does *not* correspond with the experimental system described in this thesis. In the bad cavity limit and weak excitation, the atom and cavity field remain largely uncorrelated, per photon, and the semiclassical MBE largely suffice.

The MBE also arise from semiclassical approximations of the collective spin dynamics in a *multi-atom* cQED system. In the multi-atom MBE, $\sigma \rightarrow \sum_i^N \sigma^{(i)}$ and $\sigma_z \rightarrow \sum_i^N \sigma_z^{(i)}$, with all atoms coupling to the same optical mode [AM06]. Thus, the multi-atom MBE are equivalent to the single atom MBE up to scaling factors.

Even if the entire atomic ensemble couples strongly to the cavity mode, it is generally accepted that the MBE accurately describe the system if each atom contributes only weakly to the overall coupling [SC88, RTB⁺89, RTB⁺91]. In such cases, again, each atom and photon are only weakly correlated and the mean-field, semiclassical description is sufficient.

However, surprisingly, the MBE are not inconsequential when considering the strongly coupled, strongly driven, single-atom cQED experimental system at hand. While the MBE cannot account for much that is observed experimentally or in simulations of the full quantum model, the the complete system often qualitatively appears to be guided by a competing influence of mean-field and quantum noise dynamics [SC88, AM06, KAM10]. Moreover, the application of dynamical systems analysis to the semiclassical MBE has proven successful at identifying parameters under which the quantum dynamics exhibit bifurcation-like behavior [AM06, GNH90a, GNH90b]. It has also been shown [Mab08b] that the MBE are also derivable from a method less *ad hoc* than expectation factorization through the orthogonal projection [vHM05] of the quantum master equation dynamics (3.8) onto the ‘semiclassical’ manifold of states

$$\rho_{atom} \otimes |\alpha\rangle\langle\alpha| \quad (3.18)$$

where $|\alpha\rangle$ is a coherent field state, up to a multiplicative factor in the $g\langle\sigma\rangle$ term in Eq. (3.17) of order unity representing the atomic purity; for pure atomic states, the MBE are recovered exactly.

As it facilitates analysis and provides some physical insight as well, I also provide a dimensionless version of the MBE [AM06, GNH90a, GNH90b]:

$$\begin{aligned} \dot{x} &= -k((1 + i\theta)x + 2Cp - y) \\ \dot{p} &= -(1 + i\delta)p + xD \\ \dot{D} &= -2(D - 1 + (x^*p + xp^*)/2). \end{aligned} \quad (3.19)$$

In these equations, we have made the following dimensionless scalings

$$t \rightarrow t/\gamma_{\perp}, \quad \frac{g^2}{2\kappa\gamma_{\perp}} = C, \quad \frac{\gamma_{\perp}^2}{2g^2} = n_0, \quad \kappa/\gamma_{\perp} = k, \quad \Theta/\kappa = \theta, \quad \Delta/\gamma_{\perp} = \delta, \quad y = \frac{\mathcal{E}}{\kappa\sqrt{n_0}}$$

$$\frac{\langle a \rangle}{\sqrt{n_0}} = x, \quad -\frac{1}{\sqrt{2}}\langle \sigma \rangle = p, \quad -\langle \sigma_z \rangle = D. \quad (3.20)$$

Dimensionless representations not only de-clutter equations, but they aid comparisons of dissimilar quantities. For example, we see in Eqs. (3.19) that the cavity field x is only strongly affected by the atomic dipole p when the *cooperativity* C is greater than 1, that the atom is only strongly affected by the cavity field when the intracavity photon number is at least the *saturation photon number* n_0 , i.e. $|x|^2 \gtrsim 1$, and that the system may only reach this level of high excitation when $\mathcal{E}/\kappa \gtrsim \sqrt{n_0}$. Finally, we may calculate the steady state solutions to Eqs. (3.19)

$$y = |x_{ss}| \left[\left(1 + \frac{2C}{1 + \delta^2 + |x_{ss}|^2} \right)^2 + \left(\theta - \frac{2C\delta}{1 + \delta^2 + |x_{ss}|^2} \right)^2 \right]^{1/2}$$

$$\arg[x_{ss}] = \arctan \left[\frac{\frac{2C\delta}{1 + \delta^2 + |x_{ss}|^2} - \theta}{1 + \frac{2C}{1 + \delta^2 + |x_{ss}|^2}} \right]$$

$$p_{ss} = \frac{(1 - i\delta)x_{ss}}{1 + \delta^2 + |x_{ss}|^2}$$

$$D_{ss} = \frac{1 + \delta^2}{1 + \delta^2 + |x_{ss}|^2}. \quad (3.21)$$

These steady state solutions are often a convenient starting point in dynamical analysis of the MBE [AM06, GNH90a, GNH90b].

Chapter 4

Single atom ‘bistability’

The Maxwell-Bloch equations (MBE, Eq. 3.17) introduced in the previous chapter represent a semiclassical description of cQED systems containing a single atom or an ensemble of any number of atoms. Up to scaling factors, MBE describing the two cases are equivalent. Although it’s impossible to draw a hard line between the parameter regimes the MBE adequately describe and those they don’t, the rule of thumb is that they fail to capture the complete picture when individual atoms and photons are highly correlated through strong coupling and strong driving. In these ‘deep quantum’ systems, proper modeling requires a fully quantum mechanical representation. Unfortunately, there is not yet a set of theoretical tools that generalize dynamical systems theory to open quantum systems and one typically resorts to brute force simulation for analysis. In other words, we don’t really understand or know what to expect from strongly coupled, dynamical quantum systems. In particular, the *a priori* relevance of semiclassical MBE dynamics to strongly-coupled cQED systems is unclear. This thesis doesn’t resolve this uncertainty, but it demonstrates, with experimental data, that any resolution is subtle.

This issue is not purely academic. Optical device engineering is beginning to push into attojoule energy regime [ASO⁺08, YHW⁺07, LKH⁺10, NTS⁺10]. In the visible to near-infrared regime, attojoule energies correspond to a countable number of photons; e.g. one photon with an 852nm wavelength carries an energy of .23aJ. Scientific, economic and environmental pressures are pushing information devices

smaller, faster and lower in energy [Mil09], and the logical consequence of this trend is unavoidably quantum technologies. Indeed, for future optics-based processing to be feasible, ~ 10 aJ scale devices are necessary [Mil10a], and quantum effects must be significant if not dominant when the operating photons number in the hundreds or less. Experimental and theoretical research has barely begun to systematically explore this emerging engineering paradigm.

With this motivation, this chapter introduces a case study of optical I/O nonlinear devices operating in the ~ 10 photon regime that naturally arise in single atom, strongly-coupled cQED systems. This theoretical background sets the stage for the experiments presented in the following chapters.

4.1 Absorptive ‘bistability’

The saturable absorber is a canonical optical nonlinear I/O device. At low optical drive powers, a medium may absorb a given fraction of incident photons, but at high drive powers, the total power absorbed by the medium saturates. The input-output power relationship is therefore nonlinear. Moreover, when the medium is contained in a two-sided optical resonator and if the absorption coefficient is strong enough, positive optical feedback from the resonator can even cause the I/O relationship to be *bistable*, with either a low- or high-power transmission state possible with any input power in a certain range [SDGK69].

This behavior can be inferred from the steady state solutions to the MBE (3.21), with the cQED atoms in the role of the saturable medium [RTB⁺91, AM06]. As they become excited, the atoms scatter photons into radiation modes, dissipating the drive power. The partially excited atoms also re-radiate their own intracavity field, largely 180° out of phase with the optical drive, which *coherently* interferes with the drive, preventing it from exciting the cavity. At high drive powers, however, the two-level atoms become fully saturated, and the amplitude of the re-radiated field and the rate of scattered photons no longer increase with increasing drive power. For example, for MBE parameters (Eq. (3.20)) achievable in our single atom experiment [KAM10], $\{C, n_0, \Delta, \Theta\} = \{67, .001, .7\kappa, -1.1\kappa\}$, I plot the steady-state solutions for

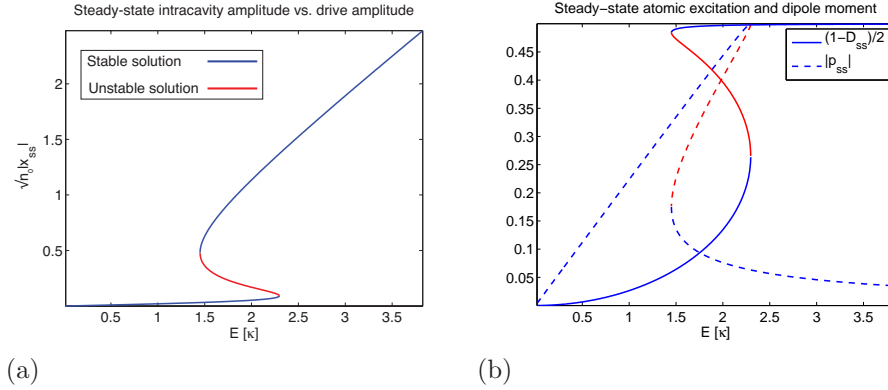


Figure 4.1: Steady state solutions to the MBE given the parameters $\{C, n_0, \Delta, \Theta\} = \{67, .001, .7\kappa, -1.1\kappa\}$. (a), Steady state intracavity field magnitude, $\sqrt{n_0}|x_{ss}|$, as a function of drive amplitude \mathcal{E} . Dynamically stable solutions are in blue, unstable solutions in red. (b), Steady state atomic excited population, $(1 - D_{ss})/2$, and dipole moment, $|p_{ss}|$, for the same parameters. Dynamical stability again shown in blue and red.

the intracavity amplitude $\sqrt{n_0}|x_{ss}|$ as a function of the optical drive amplitude \mathcal{E}/κ in Fig. 4.1 using Eqs. (3.21). At low drive amplitudes, $|\mathcal{E}| < 1.5\kappa$, the intracavity amplitude hardly increases with increasing drive. With increasing steady-state dipole moment and excited state population in response to an increasing drive amplitude, the atoms in the MBE coherently and incoherently work to prevent field build up. For a two-sided resonator, such as a Fabry-Perot cavity, the transmitted field is simply proportional to the intracavity amplitude and this low- $|x_{ss}|$ state corresponds to low optical power transmission. At high drive amplitudes, $\mathcal{E} > 2.4\kappa$, there is almost a 1:1 correspondence between increasing drive and increasing intracavity amplitude; consequently, nearly all the power incident on a symmetric, two-sided cavity is transmitted. In this regime, atom has become completely saturated, and has no mean dipole orientation ($p_{ss} \rightarrow 0$). The atom no longer responds to an increasing drive amplitude, but simply scatters photons at the maximal rate of γ_{\perp} .

Between $1.5 < \mathcal{E}/\kappa < 2.4$, however, there are three steady state solutions for any given drive strength. The low- and high- $|x_{ss}|$ states can be shown to be dynamically stable, while the mid-level one is unstable [AM06]. Thus, the unstable solution serves as a separatrix: if the system is initialized on the high- or low-side of the middle

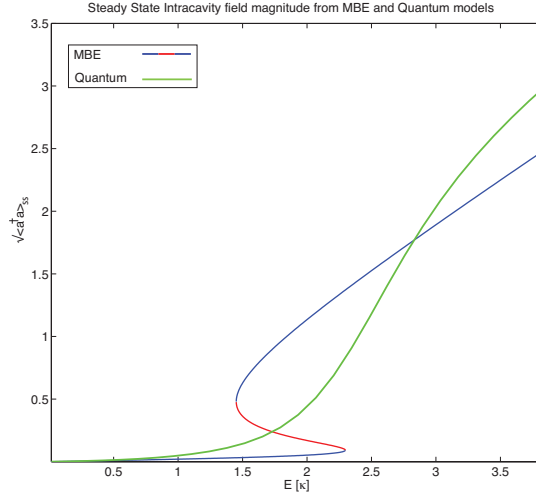


Figure 4.2: Steady state intracavity field amplitude solutions according to the MBE and full quantum models using the same parameters in Fig. 4.1.

solution, the system will respectively relax to the high- or low- $|x_{ss}|$ steady state. The MBE thus predict an *amplitude bistable* system for this parameter set. One dramatic consequence is that it should be possible to adiabatically sweep the drive amplitude from below 1.5κ to above 2.4κ and back again, and trace out a *hysteretic* I/O curve. The potential use for a hysteretic input-output device like this as a robust digital switch or for threshold signaling, has long been recognized [SDGK69, Mil10b].

But do the MBE apply in this single atom system [SC88]? To begin to answer this question, we go back to the complete quantum mechanical master equation (3.8) from which the MBE were derived and solve for the steady state density matrix for a cQED system with the same parameters, over the same range of external drive amplitudes. With these steady states, we can plot the expected magnitude of the intracavity field, $\sqrt{\langle a^\dagger a \rangle_{ss}}$, as in Fig. 4.2. In Fig. 4.2, rather than the same bistable response, we see that the expected intracavity field in the full quantum model roughly ‘‘averages’’ the semiclassical response, smoothly connecting the low- and high-drive regimes. In fact, the lack of a truly bistable response is clear simply upon solving for ρ_{ss} : for any given external drive there is a unique ρ_{ss} . Early single-atom cQED studies confirmed this failure of the MBE to describe experimental single atom systems in the strong

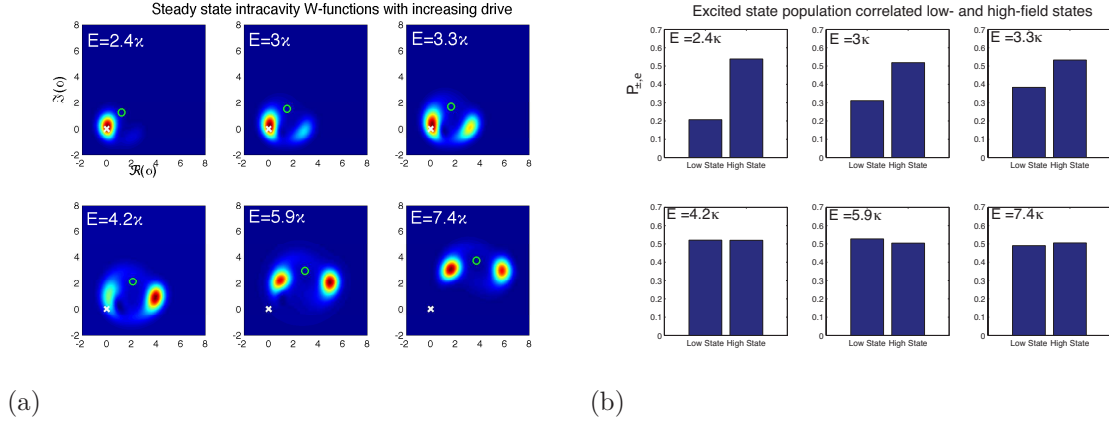


Figure 4.3: (a), Steady state intracavity field W-functions for the same cQED parameters as 4.1 and various drive amplitudes. The white cross marks the amplitude origin, the green circle the centroid of the W-function when the cavity is empty. (b), Excited state population correlated with the steady state low- and high-field states for the same parameters.

coupling regime by measuring the *long-time averaged* field transmitted by a Fabry-Perot cavity containing a Cs atom [HCLK98]. But is that all there is to say about the quantum-semiclassical correspondence?

The expected magnitude of the transmitted field is only one characteristic of ρ_{ss} . A more complete picture of the intracavity field comes when we look at the Wigner quasi-probability functions [WM08] of each ρ_{ss} after tracing over the atomic degrees of freedom, Fig. 4.3a. As the drive amplitude is increased, in Fig. 4.3a the intracavity field transitions from a near-vacuum state to a bimodal distribution for $2.4 < \mathcal{E}/\kappa < 4.2$. Further inspection of ρ_{ss} reveals that these lobes represent an *incoherent* superposition of field states, each roughly coherent with amplitudes $\alpha_- \approx 0$ and $\alpha_+ \approx \mathcal{E}/\kappa$. Moreover, by projecting each ρ_{ss} onto coherent field states centered at the low- and high-lobes, we can find the excited state population associated with each field state. To this end, in Fig. 4.3b, I plot

$$\frac{\langle |\alpha_{\pm}, e\rangle \langle \alpha_{\pm}, e| \rangle_{ss}}{\langle |\alpha_{\pm}, e\rangle \langle \alpha_{\pm}, e| + |\alpha_{\pm}, g\rangle \langle \alpha_{\pm}, g| \rangle_{ss}} \equiv P_{\pm, e} \quad (4.1)$$

for each value of \mathcal{E} in Fig. 4.3a. In Fig. 4.3b, for $2.4 < \mathcal{E}/\kappa < 4.2$, we see that the atom in the low-field state is less than completely saturated, while the high-field

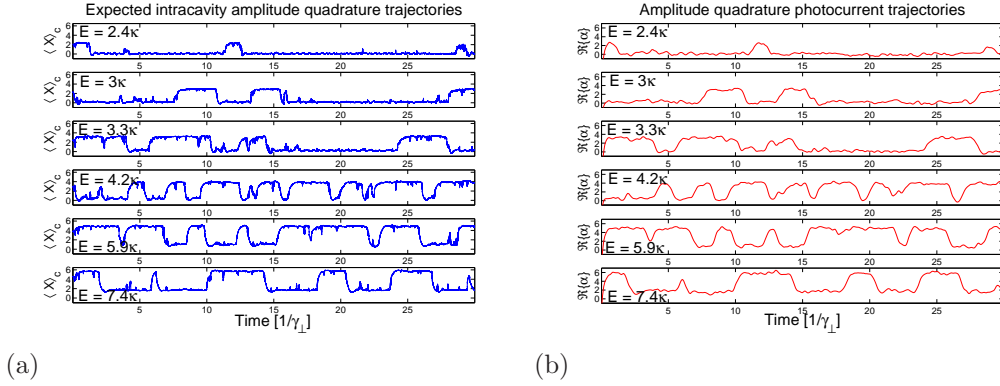


Figure 4.4: (a), Quantum trajectory simulations of the conditional expectation of the intracavity amplitude field quadrature $\frac{1}{2}\langle a^\dagger + a \rangle_c \equiv \langle X \rangle_c$ for the same parameters as Figs. 4.1. (b), Simulated, 20MHz bandwidth amplitude quadrature homodyne photocurrent data from the same trajectories in (a), assuming unit detection efficiency.

state is correlated with a fully-saturated atom. In contrast, the reemerging bimodality for $\mathcal{E} > 5.9\kappa$ associates a fully saturated atom with *both* field states, and thus has more in common with the dispersive ‘bistability’ [AC91, AMM09, Arm09] described in section 4.2.2. From Figs. 4.3a and 4.3b we see why the MBE fails to capture the complete dynamics of the system (e.g. Fig. 4.2): in this near-saturation regime the atom and cavity relax toward a superposition of highly correlated states, such that, for example, $\langle a\sigma_z \rangle_{ss} \not\approx \langle a \rangle_{ss} \langle \sigma_z \rangle_{ss}$. However, although the MBE steady state analysis cannot be simply mapped onto the more accurate quantum mechanical model in this case, the two descriptions are not completely foreign to each other. In particular, it appears that evocative ‘remnants’ of semiclassical bistability are still retained in this near-saturation regime: low- and high-excitation states exist in superposition in the steady state.

But what does it mean for the steady state intracavity field to be bimodal? The cavity can’t output a high and low amplitude field simultaneously. On a somewhat related note, why does the long-time averaged transmitted field produce an I/O picture equivalent to $\sqrt{\langle a^\dagger a \rangle_{ss}}$? These questions can be naturally addressed from the QSDE representation of the system, as in section 3.2. For instance, from a QSDE description, straightforward application of quantum trajectory techniques (section 2.2.1) allow us to simulate probable broadband homodyne measurements of the field

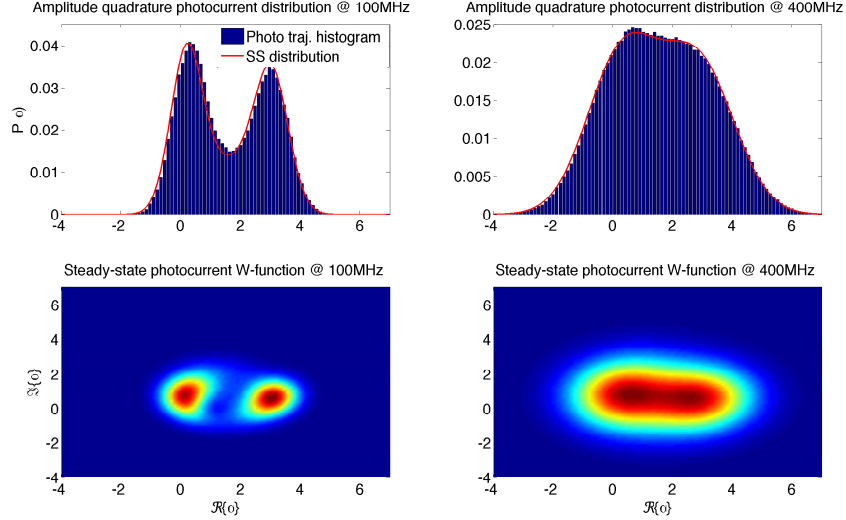


Figure 4.5: Top) Histogram of simulated amplitude quadrature photocurrents, as in Fig. 4.4b, for an experimentally-inspired cQED parameter set (that produces amplitude bistability) with 100MHz (Left) and 400MHz (Right) detection bandwidth. Overlaying the histograms are the marginal distributions expected for amplitude quadrature measurements with the system in its steady state. Bottom) Steady state photocurrent Wigner functions (section 2.1.3) from which these marginal distributions were calculated.

transmitted by a single-atom/Fabry-Perot cQED system. In Figs. 4.4a and 4.4b, I plot representative trajectory simulations of the absorptive bistability system for parameters corresponding to the steady state simulations of Fig. 4.3. In Fig. 4.4b, simulated photocurrents from the measured amplitude quadrature of the transmitted field are shown for different values of a cw drive amplitude. At low drive amplitude, $\mathcal{E} = 2.4\kappa$, the output field amplitude is essentially localized around 0, with shot noise variance. As the drive amplitude is increased, the measured field begins to switch stochastically between a low- and high-output state, with each signal state persisting for a short, characteristic time. Likewise, the conditional expected amplitude quadrature of the intracavity field associated with each simulated measurement trajectory, Fig. 4.4a, appears as a “noiseless” version of the amplitude quadrature homodyne measurement, a direct consequence of Eq. (3.15).

Recall that the distribution of high-bandwidth homodyne photocurrents may be

associated with a convolution of the cavity field and vacuum field distributions, as in section 2.1.3. If broadband photocurrents produced by an experiment or simulation with a cw drive are accumulated for time intervals much longer than their mean correlation time (see Fig. 4.3, section 2.1.3 and figure 6.4) they may be accumulated into a histogram that matches the distribution of photocurrents expected from ρ_{ss} , as in Fig. 4.5 (suggesting that the system is in a sense Ergodic). Moreover, the expected *integral* of these measurements approaches $\langle Y_t \rangle_{ss} = t\sqrt{2\kappa}\langle a^\dagger + a \rangle_{ss}$ (section 2.1.3). Thus, if an experiment only has access to long time-averaged (low-bandwidth) records, the inferred homodyne photocurrents of the field transmitted by a cavity simply reflect the steady state expectation of the corresponding intracavity field quadrature, i.e. $\sqrt{2\kappa}\langle a^\dagger + a \rangle_{ss}$, and may be used to directly compare the steady state semiclassical and quantum mechanical predictions for the intracavity field, in a manner similar to Fig. 4.2 or [HCLK98]. At the other extreme, very large bandwidth photocurrents correspond to very weak measurements of the instantaneous intracavity field, and thus appear to be mainly shot noise. However, if full bandwidth measurements are resampled at intermediate rates, only slightly faster than the bandwidth of the photocurrent autocorrelation function, a sort of quasi-‘bistability’ response to the cw drive is apparent in the transmitted field, randomly switching between low and high states that correspond to the low- and high-amplitude states of the steady state intracavity field, as in Figs. 4.4b, and accumulation of these photocurrents reveal bimodal distributions as in 4.5. This insight begs the question then, if quasi-‘bistability’ is apparent on these intermediate time scales, are other signatures of true bistability, like hysteresis, apparent on these time scales? We will take up this question again in chapter 6.

A loose explanation for the spontaneous switching dynamics visible in the quantum trajectories Figs. 4.4 is that the semiclassical steady states apparent in Fig 4.1a are ‘destabilized’ by quantum fluctuations [SC88, RTB⁺91, HCLK98]. As the low- and high- field states are essentially coherent states in Fig. 4.3, separated by only ~ 10 photons, the quantum uncertainty in the field amplitude in either state is fractionally large. For example, if the cQED system is in the saturated, high-field state, it doesn’t take that long (the apparent state correlation time in Fig. 4.4b) for the statistical

fluctuations in the intracavity field and atomic dipole to ‘kick’ the system into the unsaturated, low-field state: if, by chance, a low intracavity photon number happens to coincide with the atom being the ground state, the atom can efficiently work to reinforce the low-field state. The MBE, however, accurately predict a truly bistable system when the saturable medium is a strongly coupled atomic ensemble, rather than a single atom [RTB⁺91]. This is because although the single- and multi-atom MBE are equivalent up to scaling factors, the photon-number separation of the low- and high-field states scales as the number of atoms in the ensemble, greatly increasing the fluctuation-limited correlation times of the two states [SC88]. Ensemble cQED devices operate on much higher energy scales than single-atom devices with the same dimensionless MBE parameters (3.20) [RTB⁺91, SC88], in a regime where quantum fluctuations are dynamically negligible.

4.2 Dispersive ‘bistability’

As a highly nonlinear system with many tunable parameters, it should not be surprising that single atom cQED offers a wide range of interesting (and potentially useful) I/O regimes. While the absorptive ‘bistability’ described in the preceding section occurs right at the cusp of atomic saturation, many nonlinear I/O systems exist completely into the high drive regime. This perhaps runs contrary to a popular conception that in the high-excitation regime, single-atom cQED becomes increasingly ‘classical’ [HCLK98, EFF⁺07, FSS⁺10]. In a sense, this section complements the previous one and illustrates that even into this ‘classical’ regime of strongly coupled, but fully saturated single atom cQED, quantum dynamics are clearly apparent, if you know how to look for them [AC91, AMM09, Arm09, KAPM11]!

4.2.1 The Jaynes-Cumming ladder

The argument for recovered classical behavior in the high-drive limit comes from analysis of the Jaynes-Cummings Hamiltonian Eq. (3.1). Minus the external drive term, the spectrum of energies associated with the lab-frame Eq. (3.1) for a *resonant*

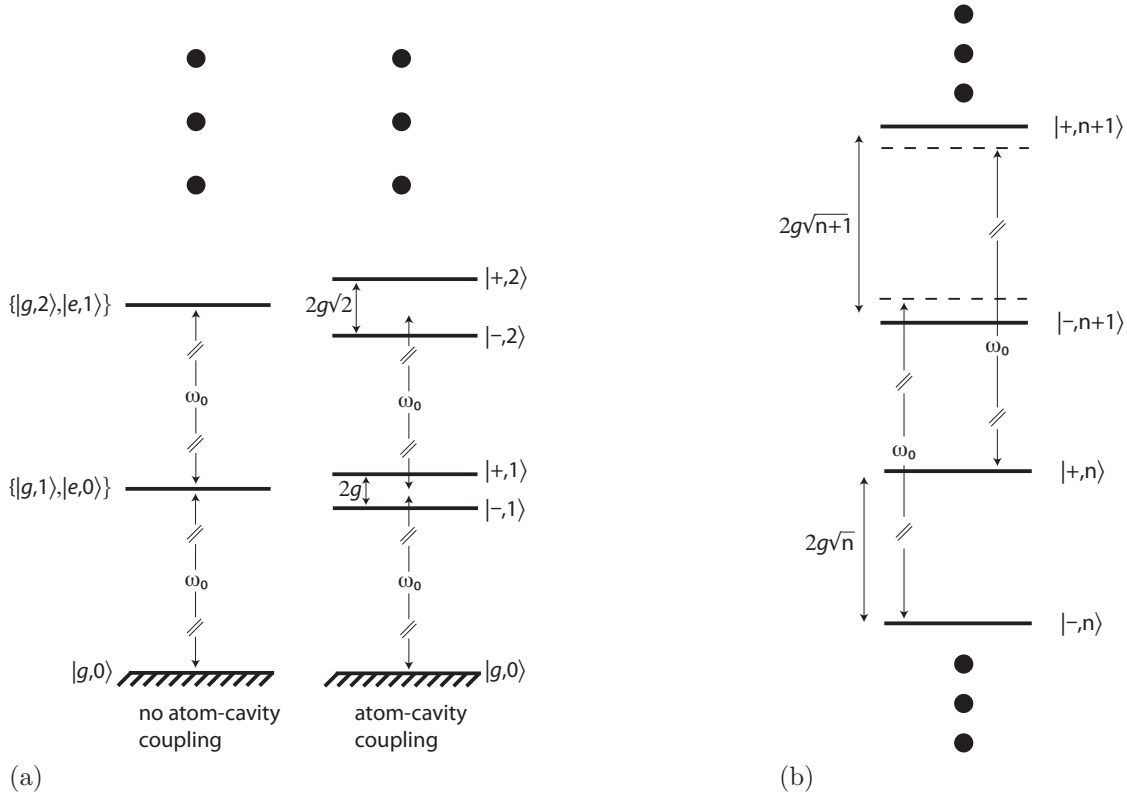


Figure 4.6: a), Lowest energy eigenlevels of the Jaynes-Cummings Hamiltonian (without the cavity drive term) in the lab frame with $\Theta = \Delta = 0$. (b), Jaynes-Cummings spectrum for high excitations $n \gg 1$. In this fully saturated regime, $|\pm, n\rangle \leftrightarrow |\pm, n+1\rangle$ transitions are nearly ω_0 -separated in energy.

system ($\omega_a = \omega_c = \omega_0$) are portrayed in Fig. 4.6. Without atom-cavity coupling ($g = 0$), the spectrum of energies is as on the left. In this resonant case, the atomic excited state has the same energy as a single photon in the cavity. Thus, the spectrum forms a harmonic ladder of states, with each ‘rung’ a degenerate doublet of $\{|e, n-1\rangle, |g, n\rangle\}$, except for the bottommost state, with energy eigenvalue $n\omega_0$. When $g \neq 0$, these degenerate states split into symmetric and anti-symmetric energy eigenstates

$$|\pm, n\rangle = \frac{1}{\sqrt{2}} (|e, n-1\rangle \pm i|g, n\rangle) \quad (4.2)$$

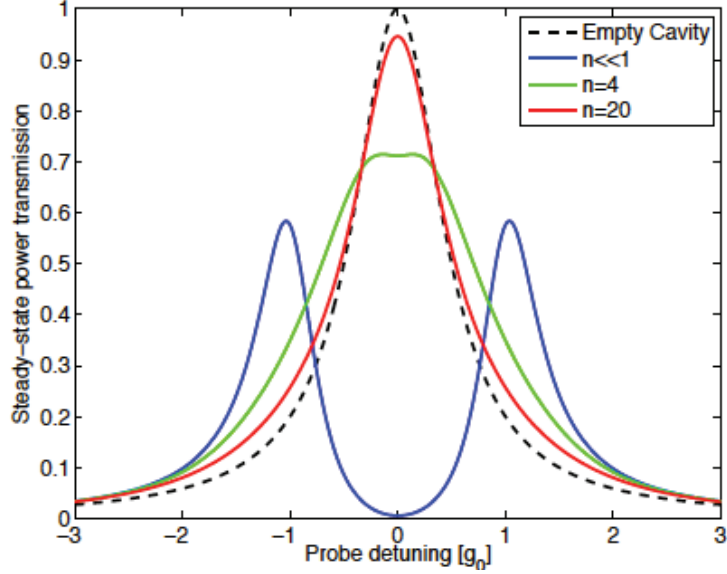


Figure 4.7: The fractional optical power transmitted by a Fabry-Perot cavity containing a resonant strongly coupled TLS at various drive powers. The n drive power index refers to the number of photons that would be in an empty cavity on resonance. Taken from [Arm09].

with energy eigenvalues $E_{\pm,n} = n\omega \pm \sqrt{n}g$. Thus, for $n \geq 1$, the energy eigenstates are associated with a fully saturated atom ($\langle \sigma_z \rangle = 0$). However, an additional atom-and-cavity ‘saturation regime’ exists very high up, when $n \gg 1$. At these levels in the energy spectrum, see Fig. 4.6b, the energy separation between eigenstates with the same \pm orientation approaches

$$E_{\pm,n+1} - E_{\pm,n} = \omega_0 \pm g(\sqrt{n+1} - \sqrt{n}) \approx \omega_0 \pm \frac{g}{2\sqrt{n}}. \quad (4.3)$$

As $n \rightarrow \infty$, the spectrum of energies approaches that of a *pair* of harmonic ladders, with raising/lowering energy $\approx \omega_0$.

Adding drive dynamics to this picture provides the necessary energy to access these high energy states, and dissipation dynamics cause the system to stabilize in some energy regime. Moreover, the spontaneous decay of photons out of the cavity, through the mirrors, and atomic spontaneous emission into radiation modes, broadens the energy eigenstates of the Hamiltonian model such that each has an intrinsic

linewidth $\Gamma \sim \max\{\kappa\sqrt{\bar{n}}, \gamma_{\perp}\}$. When an external laser also at frequency ω_0 is used to drive the cavity when $g \gg \Gamma$, the cQED system cannot easily absorb the energy quanta necessary to work its way up the first few rungs of the Jaynes-Cummings spectrum; photons from the laser drive are not resonant with any allowed energy transitions (to within their linewidth). However, a laser tuned to $\omega_0 \pm g$ will resonantly excite a ground state system to $|\pm, 1\rangle$, but again cannot easily drive the transition to $|\pm, 2\rangle$. But once an ω_0 laser does manage to *off-resonantly* excite the cQED system to the $|\pm, 2\rangle$ state, all subsequent transitions to higher energy states become increasingly resonant with the drive. If the cQED dissipation rates are slow, such that for a $g = 0$ system, a strong, on-resonant drive yields the steady state expected intracavity photon number $\langle a^\dagger a \rangle_{ss} = |\mathcal{E}/\kappa|^2 \gg 1$, then even with a strongly coupled, $g \gg \Gamma$ single atom in the cavity, the steady state $\langle a^\dagger a \rangle_{ss} \lesssim |\mathcal{E}/\kappa|^2$. Consequently, if the optical drive strength is weak, the steady state power transmitted by a Fabry-Perot cavity reveals a bimodal spectrum, with peaks at $\omega_0 \pm g$, but if the drive is strong, a single transmission peak is observed at ω_0 , as in Fig. 4.7. This ‘recovered’ harmonic spectrum at high drive strengths would seem to suggest that highly excited single-atom cQED systems are essentially classical objects, like any SHO [FSS⁺10].

4.2.2 Phase ‘bistability’ in highly-excited cQED

However, even in the on-resonant, fully saturated regime of cQED with a cw laser drive, the I/O field relationship carries clear signatures of the quantum mechanical nature of the atom-cavity system [AC91, Arm09]. A heuristic, but remarkably accurate [AC91, Arm09], explanation for this phenomenon comes from first noting that in steady state with strong drives, the intracavity field is in some coherent state (this is also suggested by the harmonic spectrum). Although the steady state system is not in a photon number eigenstate, or even an energy eigenstate, the intracavity energy distribution is centered at some $\omega_0 \bar{n}$, with width $\sim \omega_0 \sqrt{\bar{n}}$. This corresponds to a population distribution amongst the $|\pm, \bar{n} \pm \sqrt{\bar{n}}\rangle$ energy eigenstates. The separation in energy between ‘+’-oriented eigenstates is then $\approx \omega_0 + \frac{g}{2\sqrt{\bar{n} \pm \sqrt{\bar{n}}}} \approx \omega_0 + \frac{g}{2\sqrt{\bar{n}}}$ and the ‘-’-oriented eigenstates are split by $\approx \omega_0 - \frac{g}{2\sqrt{\bar{n}}}$.

We can then approximate this cQED system about the steady state as two, offset SHOs with resonant energies $\omega_0 \pm \frac{g}{2\sqrt{n}}$. As our optical drive is tuned to ω_0 , and is thus slightly off-resonant with either SHO system, the intracavity optical dynamics largely satisfy

$$\langle \dot{a} \rangle_{\pm} = - \left(\kappa \pm \frac{ig}{2|\langle a \rangle_{\pm}|} \right) \langle a \rangle_{\pm} + \mathcal{E} \quad (4.4)$$

where $\langle a \rangle_{\pm}$ is the intracavity field expectation associated with each, independent SHO sub-system (compare with the MBE (3.17)). The steady state solutions to Eq. (4.4) are

$$\alpha_{ss}^{\pm} \equiv \langle a \rangle_{\pm,ss} = \frac{\mathcal{E}}{\kappa} \left(1 - \left(\frac{g}{2\mathcal{E}} \right)^2 \right) \mp \frac{ig}{2\kappa} \sqrt{1 - \left(\frac{g}{2\mathcal{E}} \right)^2}, \quad (4.5)$$

and as $\frac{g}{2\mathcal{E}} \rightarrow 0$, $\langle a \rangle_{\pm,ss} = \frac{\mathcal{E}}{\kappa} \mp \frac{ig}{2\kappa}$. Thus the intracavity field will have a slight *phase shift* dependent on which SHO ladder the system is localized on, the ‘+’ one or the ‘-’ one. Note that the existence of only two SHO systems can ultimately be traced to the binary states of the atom. If the atom had more states, or if there was more than one atom, there would be several or many more available levels in the energy spectrum, which would eventually ‘wash out’ the digitization of the steady states $\langle a \rangle_{\pm,ss}$. The intracavity $\mp \frac{ig}{2\kappa}$ phase shift consequently results in a potentially observable positive or negative phase shift in the field transmitted by a Fabry-Perot cavity.

So which phase state will the cQED system be in? As the system is completely symmetric, the answer is, again, ‘both.’ But again, the cavity can’t simultaneously transmit both types of fields. The open dynamics efficiently decoheres any quantum superposition between the two intracavity coherent states. As in the case of single atom absorptive ‘bistability,’ we can plot Wigner functions of the steady state intracavity field for an on-resonant cQED system with increasing optical drive, see Fig. 4.8. As expected from the heuristic, semiclassical model Eq. (4.5), these fully quantum mechanical simulations show a bimodal field distribution emerging in the *phase quadrature* of the intracavity field as \mathcal{E}/g increases beyond .5, with the separation saturating at $i\frac{g}{\kappa}$. Again, it can be shown that the steady state in the full saturation regime is an incoherent mixture of the \pm SHO steady states,

$$\rho_{ss} \approx \frac{1}{2} (|-, \alpha_{ss}^- \rangle \langle -, \alpha_{ss}^-| + |+, \alpha_{ss}^+ \rangle \langle +, \alpha_{ss}^+|). \quad (4.6)$$

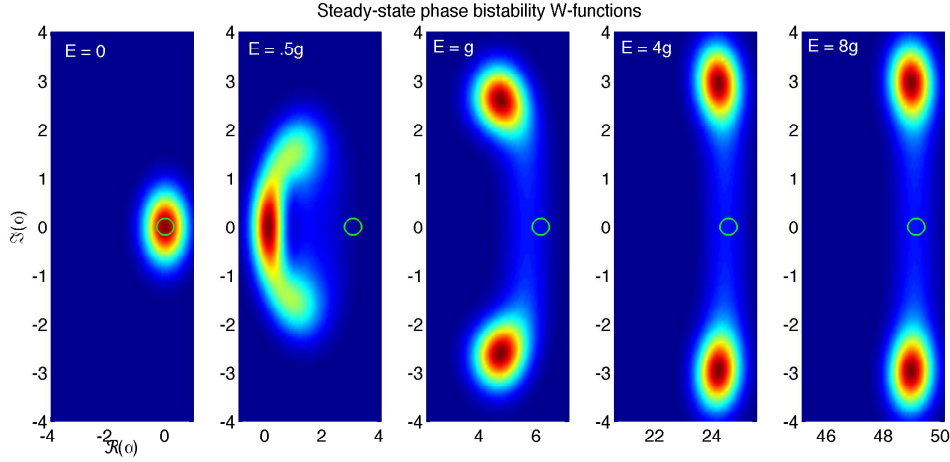


Figure 4.8: Steady-state intracavity field Wigner functions for $\{g, \kappa, \gamma_{\perp}, \Theta, \Delta\} = 2\pi \times \{56.8, 9.3, 2.6, 0, 0\}$ MHz and variable cavity drives \mathcal{E} . The green circle denotes the W-function centroid for an empty cavity for each drive case. Note that the real axis changes for each plot.

As photon counting destroys any optical phase information, if one simply measures the transmitted *power* in such a cQED system, as in Fig. 4.7, the cavity appears to simply transmit a coherent field with amplitude

$$|\alpha_{ss}| = \frac{\mathcal{E}}{\kappa} \sqrt{1 - \left(\frac{g}{2\mathcal{E}}\right)^2}, \quad (4.7)$$

which approximates the empty cavity transmission in the high-drive limit.

Phase quadrature optical homodyne measurements reveal far more interesting dynamics, however [AC91]. As with the absorptive ‘bistability’ dynamics, the answer to the question “which phase state will the cQED system be in” is essentially “sometimes one, sometimes the other.” The rate at which these transitions happen on average is $\gamma_{\perp}/2$, which can be traced to the following physical picture. We have not yet addressed the role of atomic spontaneous emission in these phase ‘bistable’ systems. As the atom is fully saturated in the strong driving regime, it will spontaneously emit photons with an average rate of γ_{\perp} . With each emission event, the atom falls into the ground state and one excitation (out of many) is lost from the system. The still-strong field inside the cavity will again work to saturate the atom, but with a

random polarization-orientation; half of the time the atom will reorient itself in the ‘+’ state, half of the time in the ‘-’ state. Thus the intracavity field, and the field transmitted by the cavity will switch randomly between the two possible phase states with mean rate $\gamma_{\perp}/2$. Although the random, digital switching between two coherent states in these phase ‘bistable’ systems (e.g. Fig. 4.9) may appear equivalent to the behavior of the amplitude ‘bistability’ system (e.g. Fig. 4.4b) at first glance, it should be emphasized that the system parameters, the underlying physical mechanisms, and the energies associated with both flavors of ‘bistability’ are quite distinct.

4.3 Toward optical control

The existence of a ‘bistable’ response to an optical input is necessary to motivate single atom cQED systems as a potential paradigm for ultra-low energy optical signaling devices. That these systems switch between the two possible states spontaneously due to quantum fluctuations in the cavity and atomic dipole is convenient for experimental demonstration that both states exist and is a fundamental issue for low-energy devices, but uncontrollable dynamics are usually useless. Some external, preferably optical, control of the signaling state would be critical in any engineering application.

To this end, we have made some initial attempts to control the switching dynamics of the phase ‘bistability’ system, as described in [KAPM11] and section 6.2. The origin of the phase bistable phenomenon depicted in Fig. 4.6b suggests an intuitive strategy for external control of the system’s phase state. By driving the cavity with an additional laser beam tuned resonant with the $|+, \bar{n}\rangle \leftrightarrow |-, \bar{n} + 1\rangle$ transition, one should be able to externally drive transitions between the two phase states. Such a strategy is attractive in its simplicity, but there are several problems with it. For instance, applying a full ‘bit-flip’ to the I/O state would depend on a carefully timed optical pulse, with the required pulse length fairly sensitive to drifts in the system parameters. Moreover, driving transitions between the two dispersive states coherently (i.e. with the additional laser) works in direct competition with the dissipative dynamics that enforce the digitization of the I/O response. On both counts, a more elegant approach would be to *incoherently* “draw out” photons that would induce

the desired transition. An additional optical cavity tuned to $\omega - 2\sqrt{\bar{n}}g$ surrounding the atom would do precisely that: a system in the $|-, \alpha_{ss}^-\rangle$ state would tend to emit photons into the additional cavity mode, relaxing the system into the $|+, \alpha_{ss}^+\rangle$ state, where it would stabilize. Unfortunately, building a second cavity is not a realistic experimental option (yet). Whereas adding another laser drive is a relative piece of experimental cake.

In the next subsections, I lay out a partial theoretical analysis for the dynamics associated with simply adding an additional $\omega - 2\sqrt{\bar{n}}g$ tuned control beam to a phase ‘bistability’ system. Not only does this analysis introduce an alternative approach to analyzing single atom cQED quantum dynamics using hybrid-Wigner functions, it is hoped the analysis will aid future efforts to find more sophisticated optical control techniques.

4.3.1 Driven transition dynamics

We model our controlled phase bistability system by adding a second cavity driving term to the Hamiltonian, representing a second, control laser at a distinct optical frequency:

$$H'' = \omega_c a^\dagger a + \omega_a \sigma_+ \sigma_- + ig(a^\dagger \sigma_- - a \sigma_+) + i\varepsilon(e^{-i\omega_p t} a^\dagger - e^{i\omega_p t} a) + i(\varepsilon_c e^{-i\omega_m t} a^\dagger - \varepsilon_c^* e^{i\omega_m t} a) \quad (4.8)$$

where ω_p is the frequency of the ‘probe’ laser, ε is its amplitude (chosen to be real, by convention), ω_m is the frequency of the ‘control’ laser with amplitude ε_c . As usual, we transform the reference frame to remove the time dependence in the probe driving term of the Hamiltonian using the transformation operator

$$T_t = e^{-i\omega_p t a^\dagger a} e^{-i\omega_p t \sigma_+ \sigma_-}, \quad (4.9)$$

which transforms the Hamiltonian as $T^\dagger H T + i\frac{\partial}{\partial t}(T^\dagger)T$ to give

$$H' = \Theta a^\dagger a + \Delta \sigma_+ \sigma_- + ig(a^\dagger \sigma_- - a \sigma_+) + i(\varepsilon + \varepsilon_c e^{-i\Phi t})a^\dagger - i(\varepsilon + \varepsilon_c^* e^{i\Phi t})a \quad (4.10)$$

where $\Phi = \omega_m - \omega_p$ is the residual rotation frequency of the control drive. The dissipative cavity decay and spontaneous emission dynamics are not affected by this transformation and are represented in a master equation by

$$\mathcal{D}[C]P = C^\dagger PC - \frac{1}{2}C^\dagger CP - \frac{1}{2}PC^\dagger C \quad (4.11)$$

using $C_c = \sqrt{2\kappa}a$ and $C_a = \sqrt{2\gamma_\perp}\sigma_-$ terms. We will assume $\Theta = \Delta = 0$ for the remainder of this section. We will further displace the expected system mean field $\alpha = \varepsilon/\kappa$ with

$$D(\alpha) = e^{\alpha a^\dagger - \alpha^* a} \quad (4.12)$$

so that we again have a new, effective Hamiltonian

$$H = ig(a^\dagger\sigma_- - a\sigma_+) + i(\varepsilon_c e^{-i\Phi t} a^\dagger - \varepsilon_c^* e^{i\Phi t} a) + i\Omega(\sigma_- - \sigma_+) \quad (4.13)$$

where $\Omega = g\varepsilon/\kappa$. We transform the dynamics yet again into a $i\Omega(\sigma_- - \sigma_+)$ interaction picture,

$$T_\Omega = e^{\Omega(\sigma_- - \sigma_+)t} = e^{-i\Omega\sigma_y t}, \quad (4.14)$$

such that

$$T_\Omega^\dagger \sigma_- T_\Omega = -\frac{i}{2}(\mu_- e^{-2i\Omega t} + \mu_z - \mu_+ e^{2i\Omega t}) \quad (4.15)$$

where the μ 's are essentially the raising and lowering operators in the Pauli- y basis: $\sigma_y|\pm\rangle = \pm|\pm\rangle$, $\mu_- = |-\rangle\langle +|$, $\mu_z = \sigma_y$. With this final transformation, the Hamiltonian becomes

$$H_{PB} = gX\mu_z - igY(\mu_- e^{-2i\Omega t} - \mu_+ e^{2i\Omega t}) + i\varepsilon_c(e^{-i\Phi t} a^\dagger - e^{i\Phi t} a) \quad (4.16)$$

where $X = \frac{1}{2}(a + a^\dagger)$, $Y = \frac{i}{2}(a^\dagger - a)$. Normally, when ε_c is not present, the rotating wave approximation is invoked at this point to omit the time dependent Hamiltonian terms. The dissipative dynamics are unaffected by this final transformation, and after the rotating wave approximation we are left with $2\kappa\mathcal{D}[a]\rho$, $\gamma_\perp/2(\mathcal{D}[\mu_-] + \mathcal{D}[\mu_z] + \mathcal{D}[\mu_+])\rho$ decay processes. For much of the rest of this analysis we will set $\gamma_\perp \rightarrow 0$ to simplify the generally much faster dynamics we are concerned with. It's hard

to pinpoint the effect of ε_c on the familiar phase ‘bistability’ dynamics. However, a number of clues about its significant effect when $\Phi \approx 2\Omega$ can be found through analysis and supported by simulation. Roughly, when this resonance condition is met, the modulation of Y at frequency Φ by the final term in Eq. 4.16 results in ‘slow’ dynamics in the atomic dipole due to the ‘ 2Ω ’ coupling term in the Hamiltonian that is usually ignored. Intuitively, this ‘control’ drive is tuned to excite coherent population transfer between the $|+, \bar{n}\rangle \leftrightarrow |-, \bar{n} + 1\rangle$ states of the system. How well it can achieve this, though, is limited both by the ‘measurement’ of the $|\pm, n\rangle$ ‘dressed state observable’ through cavity decay and the distribution of system population at any given time over various ‘rungs’ in the phase bistability eigenenergy ‘ladder.’ I attempt to understand these effects through divide and conquer: first tackling the ‘measurement’ of the system state through cavity decay without any control drive, and then isolating just the control dynamics to gain some intuition of how well they perform even without this decoherence process.

4.3.2 Dynamics without control

We will now shift to a Wigner function representation of the cavity state with the hope that it will lead to a more physical picture of the dynamics (e.g. something that appears like a Fokker-Planck equation). Thus, the system state will now be described as a hybrid object:

$$\rho(\alpha) = \frac{1}{\pi^2} \int d^2\beta e^{\beta^* \alpha - \beta \alpha^*} \text{Tr}_c[\rho D(\beta)] \quad (4.17)$$

where $\rho(\alpha)$ is a density matrix of the atom only, $\text{Tr}_c[\cdot]$ is a partial trace over the cavity field and $D(\beta)$ is the displacement operator of coherent amplitude β , and $d^2\beta = d(\Re\{\beta\})d(\Im\{\beta\})$. By writing the evolution of $\rho(\alpha)$ due to the cavity operators as partial differential operators on $D(\beta)$ (e.g. $a^\dagger D(\beta) = \left(\frac{\partial}{\partial \beta} + \frac{\beta^*}{2}\right) D(\beta)$) the cavity master equation dynamics may be turned into a differential equation for the Wigner representation [WM08]

$$\frac{\partial}{\partial t} \rho(\alpha) = \left(\frac{\partial}{\partial \alpha} (\kappa \alpha - \varepsilon_c e^{-i\Phi t}) + \frac{\partial}{\partial \alpha^*} (\kappa \alpha^* - \varepsilon_c^* e^{i\Phi t}) + \kappa \frac{\partial^2}{\partial \alpha \partial \alpha^*} \right) \rho(\alpha). \quad (4.18)$$

Similarly, if we look at the dynamics that couple the field to the atomic dipole in Eq. 4.16 we get (ignoring terms that oscillate at 2Ω)

$$\frac{\partial}{\partial t}\rho(\alpha) = \frac{i}{4}g\left(\frac{\partial}{\partial\alpha} - \frac{\partial}{\partial\alpha^*}\right)\{\mu_z, \rho(\alpha)\} - \frac{i}{2}g(\alpha + \alpha^*)[\mu_z, \rho(\alpha)] \quad (4.19)$$

where $\{\cdot, \cdot\}$ is the anticommutator and $[\cdot, \cdot]$ is the commutator. So that if we ignore spontaneous emission and the control beam, we have the master equation dynamics on this representation

$$\begin{aligned} \frac{\partial}{\partial t}\rho(\alpha) &= \frac{\partial}{\partial\alpha_i}(\kappa\alpha_i\rho(\alpha) + \frac{g}{4}\{\rho(\alpha), \mu_z\}) + \frac{\partial}{\partial\alpha_r}\kappa\alpha_r\rho(\alpha) + ig\alpha_r[\rho(\alpha), \mu_z] + \\ &\quad \frac{\kappa}{4}\left(\frac{\partial^2}{\partial\alpha_r^2} + \frac{\partial^2}{\partial\alpha_i^2}\right)\rho(\alpha) \end{aligned} \quad (4.20)$$

From Eq. 4.20, note that

$$\frac{\partial}{\partial t}\langle\mu_-e^{-2i\frac{g}{\kappa}\alpha_r}\rangle = -\frac{g^2}{\kappa}\langle\mu_-e^{-2i\frac{g}{\kappa}\alpha_r}\rangle \quad (4.21)$$

That is, the expectation of $\mu_-e^{-2i\frac{g}{\kappa}\alpha_r}$ decays exponentially at the rate $\frac{g^2}{\kappa}$. It can be shown that this operator is simply $\mu_-D(-i\frac{g}{\kappa})$ in the usual representation (and it's operator evolution is of course the same), but it was easier to identify this observable in Wigner representation. When the system (in this displaced frame) is in the subspace spanned by the states $|\pm, \mp ig/\kappa\rangle$, the expectation of this operator and its Hermitian conjugate are the off-diagonal matrix elements of the density matrix. If we are to use these off-diagonals to coherently rotate the system between $|\pm\rangle$, then we expect to want $\kappa > g$ so that these state coherences are long-lived. Note, too, that in the $\kappa \gg g$ limit, $\mu_-D(-i\frac{g}{\kappa}) \approx \mu_-$, clarifying the dynamics we're interested in yet further.

4.3.3 Control dynamics

The ‘control’ aspects of the Hamiltonian consist of those terms rotating at 2Ω in our frame:

$$H_c = -igY(\mu_+ e^{i\Phi t} - \mu_- e^{-i\Phi t}) + i(\varepsilon_c e^{-i\Phi t} a^\dagger - \varepsilon_c^* e^{i\Phi t} a) \quad (4.22)$$

where we have set $2\Omega \rightarrow \Phi$. To analyze these control dynamics, we rotate the system into the control beam frame with $T = \exp(-i\Phi a^\dagger a t)$ so that

$$H'_c = -\Phi a^\dagger a - \frac{g}{2}(a\mu_+ + a^\dagger \mu_-) + i(\varepsilon_c a^\dagger - \varepsilon_c^* a) \quad (4.23)$$

after we ignore all terms rotating at $\pm\Phi$. It is still convenient to analyze the dynamics in this frame as the atomic operators remain unaffected by the transformation. Note that that we have recovered a familiar cQED Hamiltonian with atom-field coupling Eq. (3.9). The cavity is effectively off resonant with the drive, though, by Φ . The equations of motion for the principle cQED operators are

$$\begin{aligned} \dot{a} &= i\Phi a + i\frac{g}{2}\mu_- + \varepsilon_c - \kappa a \\ \dot{\mu}_- &= -i\frac{g}{2}a\mu_z \\ \dot{\mu}_z &= ig(a\mu_+ - a^\dagger \mu_-) \end{aligned} \quad (4.24)$$

We apply the familiar semiclassical approximation (section 3.3), and replace $a \rightarrow z, 2\mu_- \rightarrow v, \mu_z \rightarrow m$ to represent the (factorized) operator expectations in the equations above. Solving for steady state, we get

$$\begin{aligned} z &= 0 \\ v &= 4i\frac{\varepsilon_c}{g} \\ m &= \pm\sqrt{1 - \left|\frac{4\varepsilon_c}{g}\right|^2} \end{aligned} \quad (4.25)$$

when $|\varepsilon_c| < g/4$. The limit for large control amplitude may be solved in this semiclassical approximation, but other than the solution $m = 0$, the steady state expectations are quite messy and probably not very useful as the semiclassical approximation is

not appropriate in this limit. Although it doesn't really apply in the simulations I've tried, however, the perturbative control amplitude limit is useful as it suggests that the phase of the control amplitude is unimportant and that the control should be able to drive complete inversions of the atomic dipole as long as it is faster than g (in the limit of very slow spontaneous emission). The suggestion of this analysis is also that a large $\sqrt{\kappa}/g$ is preferred (so that a larger inversion per external control wattage is achieved), which is consistent with the conclusions of the no-control dynamics section [4.3.2](#).

4.3.4 Simulation of a controlled quantum dot system

The principle insight from the immediately preceding sections is that the additional $\omega \pm 2\sqrt{\bar{n}}g$ laser only efficiently transfers population between the two phase states if g/κ is small. At first glance, this may seem completely contrary to the regime of 'good' phase bistability. For example, if $g/\kappa < 1$, the bimodality in [Fig. 4.8](#) would be impossible to see. However, these figures aren't very relevant in this context. For example, any coherent state is perfectly distinguishable, given an infinite integration time. What ultimately limits the visibility of a phase bistability system is the *correlation time* of the phase states, i.e. $2/\gamma_{\perp}$, recall [Eq. \(2.14\)](#) and [Fig. 4.4b](#). Thus, simple arguments suggest that the visibility of a phase bistability system essentially scales as $g/\sqrt{\kappa\gamma_{\perp}} \propto \sqrt{C}$; two cQED systems with different $\{g, \kappa, \gamma_{\perp}\}$ parameters, but similar cooperativities C should yield phase bistability systems with similar visibility.

In this light, the world of nanophotonics looks particularly appealing. Solid state cQED systems typically feature extremely small mode volumes and broad cavity linewidths, relative to what's achievable in gas-phase cQED systems. For instance, a photonic crystal cavity containing a single quantum dot demonstrated in the Vuckovic group [[FMK⁺10](#)] features a parameter set of $\{g, \kappa, \gamma_{\perp}\} = 2\pi \times \{20, 40, .1\}$ GHz, which has a comparable cooperativity as our Cs/Fabry-Perot system, but with $g \sim \kappa$. In quantum trajectory simulation we can straightforwardly try the intuitive optical control strategy of adding a $\omega + 2\sqrt{\bar{n}}g$ cw laser that should simply *increase* the mean rate at which transitions between the two phase states occur.

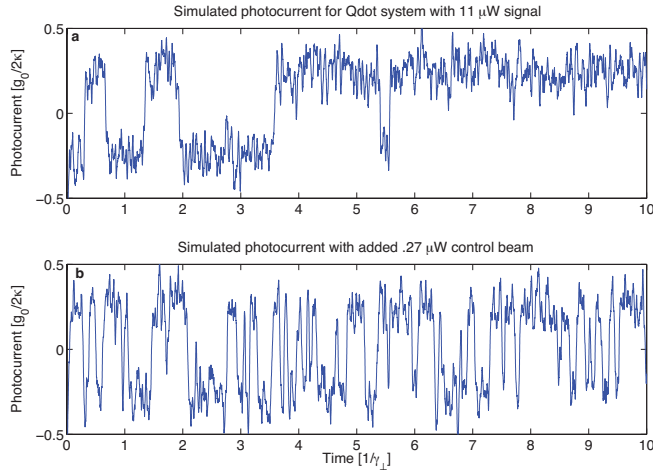


Figure 4.9: (from [KAPM11]) (a) Simulated photocurrent segment assuming cQED parameters demonstrated by [FMK+10], a $11\mu\text{W}$ probe with perfect detection efficiency with a 10GHz detection bandwidth. (b) Simulated photocurrent segment assuming the same system, plus a $.27\mu\text{W}$ cw ‘control’ beam detuned by the magnitude of the quantum dot-mode coupling Hamiltonian, i.e. by -400GHz relative to the probe beam.

The results of this simulation are seen in Fig. 4.9 [KAPM11]. With no control beam present, simulated phase-quadrature homodyne measurements portray a normal phase bistable system with switching at rate $\sim \gamma_{\perp}/2$. Although $g/\kappa < 1$ in this system, the relatively slow atomic decay allows the photocurrent to be aggressively low-passed (here at 10GHz) such that the difference in phase mean of the two states is clearly visible. When a cw control beam with less than 2.5% of the optical power of the signal probe beam is added, the spontaneous switching rate clearly increases by roughly an order of magnitude. Although neither phase state is actually stabilized, if the signaling state is instead defined as the *rate* of spontaneous phase switching, we can define-our-way-to-success by this simulated demonstration of a controlled ultra-low energy optical device that exploits a single two-level atom to produce a digital I/O response.

To give a sense of the energy scales involved here, an $11\mu\text{W}$ probe corresponds to roughly 100 intracavity photons, or a 20aJ intrinsic energy scale. More simple calculations show that the energy dissipated in the control beam (out of every control

photon incident on the cavity) per induced switching event falls in the 100aJ/edge regime, right at the current state of the art for controlled nanophotonic switching devices [ASO⁺08, YHW⁺07, LKH⁺10, NTS⁺10]. However low, 100aJ is still almost three orders of magnitude above the apparent, single-photon (sub-aJ) energy difference between the phase states. The experimentally difficult (but conceptually elegant) detuned-cavity approach to “drawing-out” single photons to stabilize desired phase states confirms that much more energy efficient approaches to controlled and quantum nanophotonic devices exist in principle. It is hoped and expected that more sophisticated techniques such as pulse-shaping could help bring all-optical control to cQED devices like these down to this “natural,” single-photon limit.

Chapter 5

The broadband cavity QED apparatus

An experiment was built to realize a strongly-coupled single-atom cQED system that could be driven at and beyond the point of atomic saturation and the field transmitted by the cavity monitored with broadband homodyne detection. The vast majority of the apparatus was inherited from Michael Armen's thesis work [[Arm09](#)], himself building upon a less specialized laser-cooling setup built by Anthony Miller.

In the experiment, a cloud of laser-cooled (but still thermal) Cs atoms are dropped onto a high-finesse Fabry-Perot cavity that is actively stabilized to be resonant to optical drives close in frequency to the D2 line in Cs [[Ste](#)]. The Cs cloud is diffuse enough, and the fundamental cavity mode a small enough target that as the cloud free-falls past the cavity only single atoms interact with the mode. Weak, off-resonant optical probing and optical heterodyne detection of the transmitted field is used to detect when an atom is near-maximally coupled to the cavity mode. Upon detection, the optical probe is immediately shifted to a frequency and amplitude appropriate to drive the system into its saturation regime and observe the dynamical response of the transmitted field.

5.1 The atom

There's no such thing as a two-level atom, but we have a nice little alkali that can approximate one pretty well: ^{133}Cs , the only stable isotope of cesium. With a nuclear spin of $7/2$ and a single valence electron, the lowest hyperfine electronic states have the valence electron in an S orbital, with total angular momentum quantum numbers $F = 3$ and $F = 4$. Our experiment attempts to target a single optical transition from one Zeeman magnetic sub-level in this ground state manifold to another single Zeeman sub-level of a low-lying electronic excited state. Specifically, we attempt to isolate the $(6S_{1/2}, F = 4, m_F = +4) \leftrightarrow (6P_{3/2}, F' = 5, m_F = +5)$ transition using a near-resonant, circularly polarized optical probe with a wavelength of roughly 852nm. This transition is an atomic *cycling transition*, meaning that a properly tuned and polarized cw probe will rapidly drive an atom initialized anywhere in the $F = 4$ hyperfine ground state manifold to the $m_F = +4$ state, where it will then continuously cycle between the $(6S_{1/2}, F = 4, m_F = +4) \leftrightarrow (6P_{3/2}, F' = 5, m_F = +5)$ ground and excited states. Imperfect optical polarization and (to a lesser degree) fluctuating magnetic fields can cause the atom to explore different states within the $F = 4$ and $F' = 5$ manifolds. For our purposes here, this is problematic as each ground and excited state has a different coupling strength to a given optical drive, and can even cause the atom to be optically pumped into the 'dark' $F = 3$ ground states, where it is effectively lost to the experiment. Thus, maintaining full control of the optical polarization inside our cavity was a high priority in the experimental construction.

A nice thing about working with real atoms is that they are *all the same*. This is not the case with any solid-state 'atom' in a photonic or superconducting microwave system. The solid state atoms can be fairly tunable and stay put, but are also frustratingly inconstant and are only partially understood [TMH⁺08, PLZY08, HKD⁺09]. You know what you get with Cs. Gas phase atoms are also attractive in quantum optics for their spectrally narrow near-IR transitions; the lines are narrow in large part because these gas-phase neutral atoms interact only weakly with their environment. The transition utilized here has an excited state lifetime of 30.4ns, or, equivalently, a mean excited state decay rate of $2\gamma_{\perp} = 2\pi \times 5.2\text{MHz}$. The main trade-off with

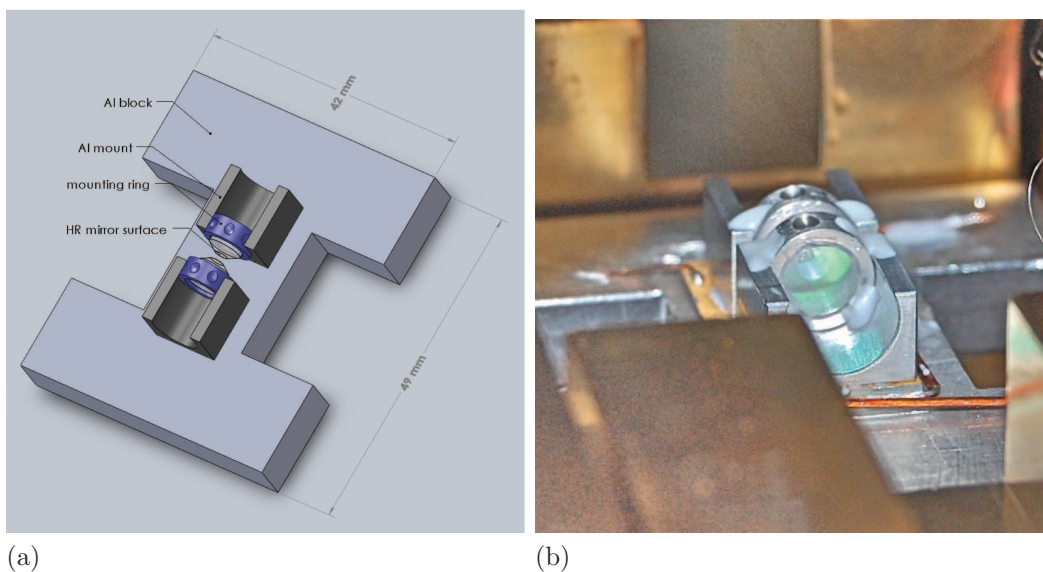


Figure 5.1: (a) Schematic of the Fabry-Perot cavity assembly, down to the first level of the vibration isolation stack. The shear mode piezo plates between the Al mounts and Al block are not shown and the separation between the high reflecting mirror surfaces (HR) is greatly exaggerated. (b) Photo of the experimental cavity in the UHV chamber, on the multi-level (and gold-plated) vibration isolation stack.

working with an atomic system with such nice coherence properties is that Cs (and any neutral atom) requires bulky, complicated, and fussy vacuum and laser cooling systems just to put the atoms where we want them. For additional spectroscopic information of the relevant states of Cs, I refer the reader to Dan Steck's excellent notes [Ste].

5.2 The cavity

Although we are pretty much stuck with Cs's spectral and coherence properties (nice as they are), our optical cavity has a flexible design. The resonator is formed by two identical, slightly curved, ultra-high reflecting dielectric mirrors facing each other, forming a Fabry-Perot cavity [Sie86]. Cavities very much like these have been used in single atom, strong coupling cQED experiments from the beginning [ORX⁺87, RTB⁺91, TRK92, MTCK96, HCLK98].

The primary design consideration in single-atom cQED experiments is to construct a cavity that gives the desired atom-coupling and cavity field decay rates, g and κ (section 3.1). The coupling rate for a given resonator can be calculated from [Car93a]

$$g = \frac{d}{\hbar} \left(\frac{\hbar\omega_a}{2\epsilon_0 V} \right)^{1/2} \quad (5.1)$$

where ω_a is the angular frequency of the atomic transition, d is the transition's dipole moment [Ste], and V is the 'mode volume' of the cavity, essentially the volume the intracavity photons occupy. For our near-planar, Fabry-Perot cavity, the fundamental TEM₀₀ mode has roughly the volume of a cylinder with the length of the cavity and radius of half the mode waist [Sie86]. Thus, single-atom cQED systems tend to be made with as small a cavity as possible, to minimize V . Small cavities also tend to have fast field decay rates (the smaller the cavity, the more frequently photons reflect off the cavity boundaries), and so high construction quality to minimize intracavity optical loss is also essential. Our cQED system is about at the state-of-the-art in its single atom cooperativity [BMB⁺04, PSK08], and it's not far from the best achievable with comparable technologies [HKY01].

The mirrors are a $\lambda/4$ dielectric stack (of about 40 layers) on a 10cm radius of curvature super-polished glass surface (5mm dia. x 4mm cylindrical substrate) special ordered from A(dvanced) T(hin) F(ilms). As the diameter of ATF's substrate and curvature of the mirror surfaces limit the minimum cavity length achievable, the mirrored end of the substrate is coned down by ATF to 2mm dia, see Fig. 5.1. These mirrors were designed for 8ppm transmission at 852nm at normal incidence, with a measured absorption/scattering loss of 2ppm. The cavity eventually constructed (more on that shortly) had a length of $27\mu\text{m}$ corresponding to a free spectral range (FSR) of 5521GHz, a finesse $\mathcal{F} = 300,000 \pm 5\%$, and minimum TEM₀₀ waist of $18\mu\text{m}$ – I refer the reader unfamiliar with Fabry-Perot characterization to Michael Armen's thesis [Arm09] and [Sie86]. Given this cavity length, the curvature of the mirrors, the cavity finesse, and the targeted atomic transition, the cQED parameters achieved by the fundamental TEM₀₀ optical mode in the this system are calculated to be $\kappa = 2\pi \times 9.3\text{MHz}$ and a maximal coupling rate of $g = 2\pi \times 56.8\text{MHz}$ with the atom

positioned at a cavity mode anti-node.

The mirrors themselves were each mounted in slightly oversized aluminum rings and held in the rings by three, 15mil thick strips of RTV655 symmetrically placed in the small gap between the mirror substrate and ring. The rings were then each placed in the half-pipe slots of two $\sim 1\text{cm}^3$ Al mounts. Each mirror-mount was then glued (with Torr Seal) to the top of a double stack of shear-mode piezoelectric plates, the stacks themselves glued (with conductive epoxy) to the top of a cracker-sized Al block, see Fig. 5.1. The stacks were placed within 1mm of each other with the mirror surfaces nearly touching, and oriented such that they shear either towards or away from each other, for the same applied bias voltage (externally supplied from UHV-compatible electrical leads). The cavity was then aligned by hand, optically characterized, and finally each ring was glued with Torr Seal to their Al mounts. Again, I am deeply in Mike's debt here as he made the cavity used in these experiments. Once prepared, the Al-block carrying the cavity was placed inside the UHV chamber on a multi-stage vibration isolation stack, the piezo leads stripped down to single strands (to minimize mechanical coupling to the cavity through the wires) and connected to electrical UHV feedthroughs, and the vacuum chamber resealed.

Ultra-high finesse cavities are extremely sensitive to minute intracavity optical phase shifts. If we require the cavity resonance frequency to be stabilized to a small fraction of the cavity linewidth, κ , then we have to control the optical phase inside the cavity to within much less than π/\mathcal{F} [Arm09, Sie86]. First, this means that our cavity length must be stabilized to within $\ll \lambda/2\mathcal{F} \approx 1\text{pm}$! Second, ultra-high finesse cavities can easily exhibit strong optical birefringence, with the resonance frequencies of orthogonal linear polarized cavity modes separated by $\gtrsim \kappa$. The origin of this birefringence is usually minute stresses in the dielectric mirror stack applied by the mirror mounting that give different polarizations a slightly different phase shift upon reflection. As the atomic transition we attempt to drive is circularly polarized, this linear birefringence is problematic for several reasons [Arm09]. Some groups solve this issue by using mirrors formed on very long cylindrical substrates, and glue the mirror as far away from the dielectric stack as possible to minimize the stresses on the mirrors [Moo05]. In this experiment we attempted the symmetric and relatively

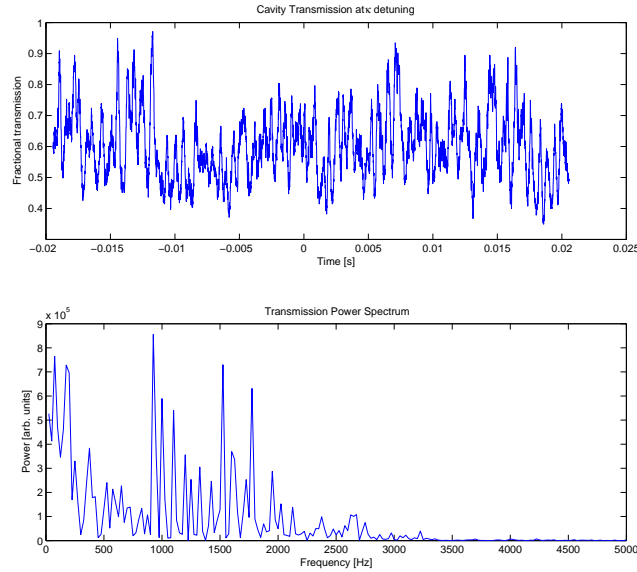


Figure 5.2: Using only a 300V battery to tune the empty cavity resonance $\approx \kappa$ from the optical probe frequency, and despite passive stabilization, cavity instability is significant even on kHz timescales. The transmitted power was measured with direct detection (top). Bottom plot shows the power spectrum of the transmission signal, with instability noise out to 2kHz.

weak mounting with the RTV strips.

This solution yielded a cavity with no perceptible birefringence, but unfortunately had far greater mechanical stability issues than the previous cQED experiment. The finesse of the cavity used in this work is more than twice that of the first cavity ($\mathcal{F} = 130,000$) [Arm09, AMM09], meaning the stability constraints are also more than twice as stringent. The relative floppiness of the RTV mounting probably also contributed to the instability issues. For example, using only a battery voltage to supply the piezo bias to define the mirror separation and the cavity resonance κ -detuned from the the optical probe, the cavity-transmitted power is seen to fluctuate by almost 50% on ms-timescales, Fig. 5.2. We are still unsure of the origin of this instability noise, but it is suspected to be mechanical vibrations in the piezo stack wires ‘short circuiting’ the vibration isolation stack [Arm09], despite efforts to mechanically decouple these wires from the cavity mount. Efforts to actively compensate for these

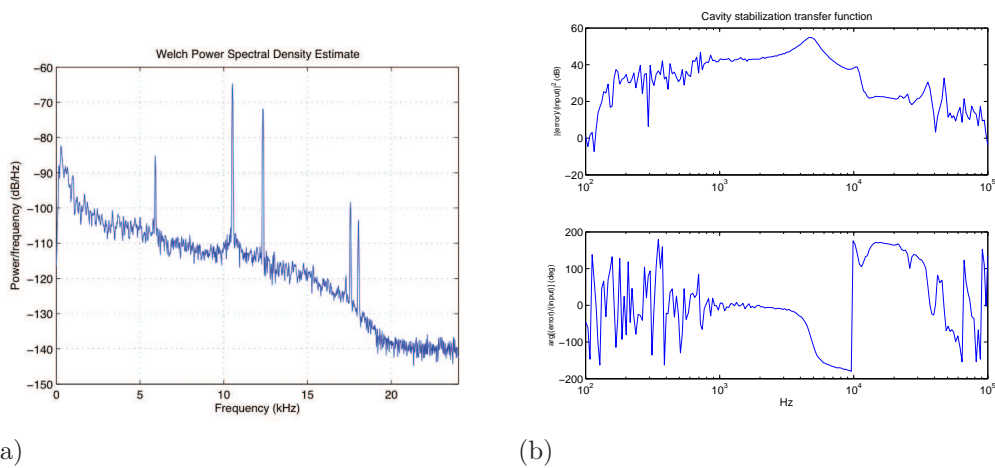


Figure 5.3: (a), Mechanical resonances in the Al block on which the cavity was mounted, measured by microphone and tapping the bare, suspended block. The largest resonances appeared to be near-fundamental flexure modes, with an antinode right where the cavity was placed. (b), Electro-optical Bode plot of the cavity as seen by its stabilization circuit. With the cavity length stabilized with only a ~ 100 Hz bandwidth servo, the AC piezo voltage to PDH error signal was mapped out, with apparent resonances corresponding to the modes of the Al block.

mechanical fluctuations using the standard Pound-Drever-Hall (PDH) cavity locking technique [DHK⁺83] were hindered by 5, 10, 12kHz and mechanical resonances in the Al block, see Fig. 5.3a, which appeared to be near-fundamental, drumhead flexure modes. Although eventually minimized with strategically placed (mechanically lossy) Viton tabs and a complex PID controller, these cavity instabilities were a constant technical difficulty; the cavity construction design could still be improved.

5.3 A tour of the apparatus

5.3.1 Science cavity locking and probing

Again, the apparatus used in this experiment was inherited from our group’s earlier cQED work [Arm09, AMM09], and largely constructed by Mike Armen and Tony Miller. Although significant structural re-arrangement of the optics, overhauls of many supporting electronics, and more sophisticated modulation of the cavity probes

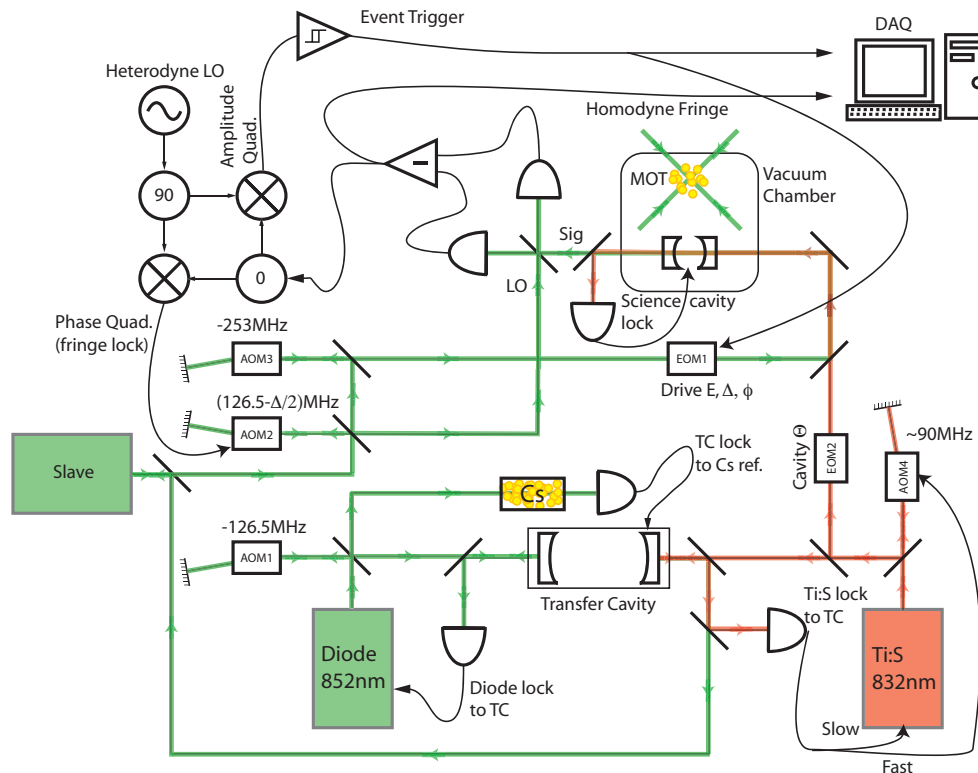


Figure 5.4: A schematic of the major components involved in cavity stabilization and probing, and homodyne detection of the cavity-transmitted field.

occurred in the course of this work, the vast majority of the hardware (and software) was in existence, if not in place, long before I arrived on the scene. As most of the apparatus is so similar to what is described in Mike's thesis, in this section I largely step through the new optical probe generation and mention the other modifications of note since 2009. Both his and my descriptions barely scratch the surface of the technical details required to make the whole apparatus work, but they provide some guidance for navigating the structural overview.

A Toptica DL Pro laser operating at 852nm wavelength and 70mW cw optical power acts as the master light source in this experiment. A double-passed acoustic optic modulator (AOM1, see Fig. 5.4) operating at -126.5MHz allows us to frequency stabilize the DL Pro 253MHz to the blue of a TEM_{00} mode of a 25cm long,

mechanically-stable ‘transfer cavity’ (TC) using the PDH method and a servo bandwidth of $\sim 500\text{kHz}$. A small fraction of the DL Pro’s output power is also used in a Cs modulation transfer spectrometer to measure the laser’s frequency deviation from the $(6S_{1/2}, F = 4) \leftrightarrow (6P_{3/2}, F = 5)$ atomic transition, producing an error signal that is servo’ed at $\sim 100\text{Hz}$ to lock the transfer cavity resonance to this atomic reference.

The primary purpose of the transfer cavity is to provide a stable frequency reference for the ‘science’ 852nm lasers and a ‘science cavity locking’ laser system operating at 832nm. The 832nm laser is sourced from a titanium-sapphire (Ti:S) monolithic block resonator that is also frequency locked to the transfer cavity via PDH, with feedback to the Ti:S etalon and a double passed AOM (operating at $\sim 90\text{MHz}$). As the transfer cavity is 25cm long, $FSR = 797\text{MHz}$, the available resonant modes are far denser in frequency than in the $27\mu\text{m}$ -long science cavity. Despite this, it is impossible to pick a TC configuration such that the TC-locked DL Pro and Ti:S lasers are also co-resonant with the science cavity. A Photline waveguide electro-optic modulator (EOM2) is used to put broadband-tunable frequency sidebands on the Ti:S carrier frequency that provide the needed additional degree of freedom. One of these sidebands serves as the ‘laser’ for a transmission-PDH lock of the science cavity length. While the Ti:S carrier is ultimately referenced to the Cs line via the TC, EOM2 can produce an optical frequency exactly two science cavity FSR away from the desired $\sim 852\text{nm}$ resonance frequency (thus setting the probe-cavity detuning Θ in the experiment).

The secondary purpose of the transfer cavity is to spectrally ‘scrub’ the 852nm laser. As our measurements rely on sensitive optical homodyne measurements, and the science cavity effectively adds several meters of delay in one of the arms of the ‘interferometer,’ laser phase noise was significantly above the local oscillator shot noise in the critical 1-10MHz band of our measurements for large science-cavity drive powers (several nW). The solution to this difficulty was to use the dramatically narrower 852nm laser transmitted by the 8kHz-linewidth TC as the optical reference in the experiment, see Fig. 5.5. As only a few μW were transmitted by the narrow-line TC, it is used to seed a homemade slave diode laser. Remarkably, the narrow line of the TC-transmitted DL Pro laser was perfectly replicated by the $\sim 100\text{mW}$ slave laser,

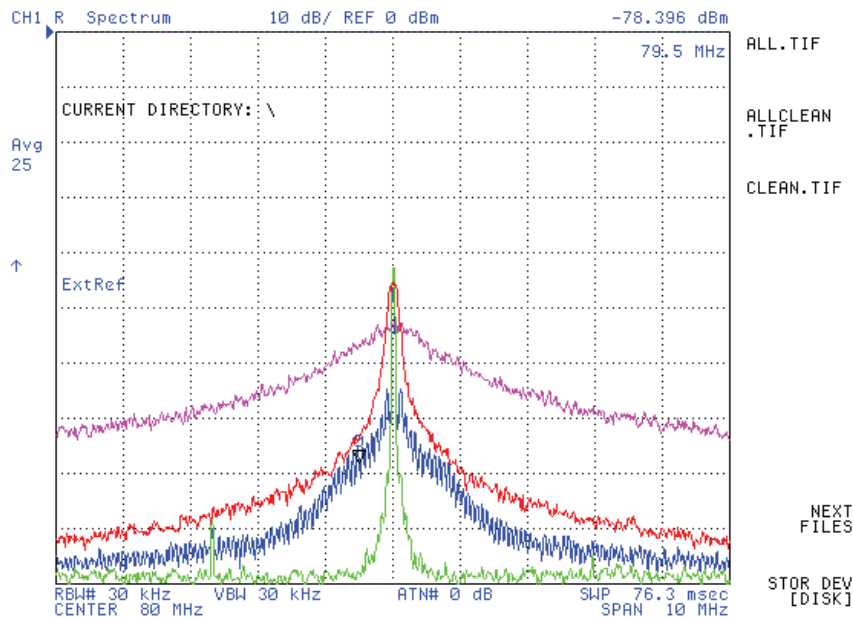


Figure 5.5: Frequency noise spectrum of various laser components, as measured by a 1km (80MHz) self-heterodyne apparatus borrowed from the Kasevich group. Red, free-running DL Pro operating at 852nm. Blue, DL Pro frequency stabilized to the transfer cavity. Purple, slave laser output without DL Pro seed. Green, DL Pro as transmitted by the transfer cavity *and* slave laser output when seeded by TC-transmitted DL Pro. Note that the horizontal axis is linear in frequency (10MHz span) and the vertical axis is logarithmic in frequency noise power.

see Fig. 5.5.

The output of the slave laser provides both the probe for the science cavity and the optical local oscillator (LO) for the hetero/homodyne detection. The $\sim 1\text{mW}$ LO was produced from a pick-off beamsplitter and a double-passed AOM2 set in the vicinity of $+126.5\text{MHz}$, variable to perfectly frequency match the Δ detuned probe emanating from the science cavity. The probe beam is first further red-shifted by another double-passed AOM3 at -253MHz , before entering another Photline EOM1 that is used to provide dynamic sidebands to the probe carrier, one of which becomes the single, saturating ‘laser’ that near-resonantly drives the science cavity. The probe

transmitted by the science cavity is carefully mode-matched to the LO beam and interfered on a 50/50 beamsplitter. The two outputs of the beamsplitter are then detected by a DC-80MHz balanced photodetector (New Focus model #1807), providing a broadband homodyne detection of the science cavity-transmitted field with typical fringe visibility of 80%.

5.3.2 Delivering the atoms

The laser cooling optical system is fairly standard [MvdS99]. Roughly $\sim 60\text{mW}$ of power from the slave laser is picked off and after some more frequency modulation seeds a homebuilt tapered amplifier. The $\sim 200\text{mW}$ amplified beam then enters a custom-built $2 \rightarrow 6$ PM-fiber splitter. The other fiber input receives a few mW of the light from a completely separate, homebuilt ‘repumper’ diode laser locked to the $F = 3 \leftrightarrow F' = 4$ D2 transition. The 6 fiber outputs are polarized, collimated into $1''$ -spot sized modes of roughly 8mW each, and directed to orthogonally intersect roughly 1cm above the science cavity in the vacuum chamber. A large anti-Helmoltz and smaller Helmholtz coils outside the chamber form a quadrapole magnetic field directly above the $10\mu\text{m}$ gap in edges of the cavity mirrors. A Cs getter run at $\sim 3\text{A}$ fills the 10^{-9}Torr vacuum chamber with cesium, which then forms a $< 100\mu\text{K}$ ensemble of perhaps 10^6 atoms (MOT) 1cm directly above the cavity in a few seconds.

The loading of atoms into the cavity is accomplished by simply turning off the trapping anti-Helmholtz coils and cooling lasers (in a choreographed fashion) and letting them fall under gravity toward the cavity mode. The atom cooling is enough such that after falling 1cm , the free-fall velocity dominates any residual thermal motion of atoms in the cloud. Because of the very narrow acceptance angle for atoms to make it through both the top gap in the cavity mirrors and into the fundamental TEM_{00} mode, the imperfect, 1° vertical tilt in the cavity mode was almost too much for any atoms to ever get into our cavity! Amazingly, positioning the MOT close to 2° from the vertical, and relying on the thermal transverse velocity to put some atoms on the right ballistic trajectory yielded a few atom transits per MOT-drop (more or less as monte carlo simulations of atom deliveries suggested). The most frustrating aspect

of the atom delivery was actually the fiber splitter. Despite taking good care of the polarization of the injected light and thermal stabilization, the power balance in the splitter was off by a factor of 2 in some places, and changed slowly in time. Moreover, the polarization exiting the PM fibers was hardly stable, and it typically took a few hours of repeated MOT-dropping for the entire splitter to thermalize to the switching beams before the polarization (and thus MOT) stabilized to something serviceable. Thankfully, the fiber-splitter has since been replaced with a free-space beam delivery system.

5.3.3 Transit detection and homodyne measurements

While the entire MOT cloud takes only a few ms to pass by the cavity, each individual atom that interacts with the cavity mode in free-fall spends only $40\mu\text{s}$ in a coupled state. With only a few atoms near-maximally coupled per MOT-drop, it's essential that we trigger our experiment on maximal-coupling events.

With the science cavity locked to the appropriate resonance frequency for the experiment, and while the MOT is loading, the probe is detuned from its experimental frequency by a few MHz and attenuated to a power such that the cavity without any atom has a mean intracavity intensity below the atomic saturation point. In this non-saturation regime, the semiclassical MBE (3.17) predict that the steady state intracavity field with an atom-position dependent coupling is

$$\langle a \rangle_{\text{unsat}} = \frac{\mathcal{E}'(\gamma_{\perp} + i\Delta')}{(\kappa + i\Theta')(\gamma_{\perp} + i\Delta') + g^2(\mathbf{r})} \quad (5.2)$$

where $\{\mathcal{E}', \Theta', \Delta'\}$ are the cQED drive amplitude and detuning parameters for this weak probe. Thus, for a near-resonant probe, a minimum in the cavity transmission corresponds to a near-maximally coupled atom. With the weak, detuned optical probe, continuous heterodyne detection of the transmitted field can reveal the presence or absence of individual atoms in the cavity mode in real time with a high signal to noise ratio. Fig. 5.6 shows four individual atom transits with near maximal coupling (and a few with lesser coupling) from one MOT drop, measured from the demodulated amplitude quadrature of a continuous heterodyne measurement trace.

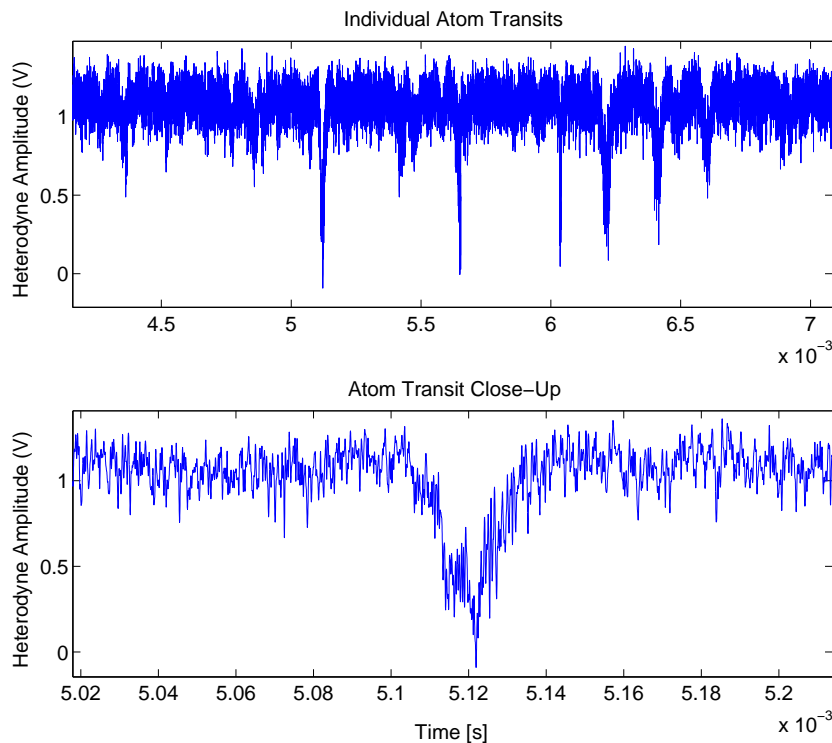


Figure 5.6: Individual atom transits during a single MOT-drop, as seen with amplitude quadrature heterodyne detection of the field transmitted by the cavity with a weak and off-resonant probe. Near-maximally coupled atoms are signaled by the near-extinction of the measurement signal. Top, several-ms long, real-time measurement record showing at least four, near-maximally coupled atom transits (and a few less-coupled transits). Bottom, close up of the first near-maximally coupled transition.

The continuous, weak heterodyne probe serves another important purpose. The eventual homodyne detection critically depends on the relative optical phase between the signal emanating from the cavity and the LO. However, over the several meters of free-space propagation, the length of the LO and signal paths fluctuate by more than an optical wavelength due to slow mechanical and thermal drifts. While the amplitude quadrature of the heterodyne signal is used to identify atom transits, the phase quadrature is continuously feedback to the FM-modulation input of the RF generator that drives the LO-shifting AOM2, locking the phase-quadrature signal to

zero with a $\sim 1\text{kHz}$ unity gain bandwidth and thus also locking the relative optical phase of the signal and LO beams. As the atom transits and the experiment itself last for a small fraction of a ms, this slow feedback loop guarantees that the homodyne measurement experiments may be performed with a known optical phase-reference.

Rather than record the atom transits, as in Fig. 5.6, the amplitude quadrature of the demodulated heterodyne signal is fed into a fast Schmitt trigger that compares the transmitted optical signal to a low voltage threshold deemed to signify the presence of a maximally-coupled atom. The firing of the Schmitt trigger causes the cavity probe to be frequency, phase, and amplitude shifted to the appropriate settings for measuring the dynamical response of the cQED system with a saturating drive. Its firing is also recorded by the fast, 200MS/s GageScope card used for data acquisition. As the signal produced by the balanced photodetector is recorded over the entire period that the MOT cloud is expected to be in the vicinity of the cavity, this signal from the Schmitt trigger is critical to mark the point in time that the experiment actually began. In some experiments, the experimental probe drive was amplitude modulated at relatively fast $\sim 1\text{MHz}$ frequencies, achieved by driving EOM1 with the AM-modulated RF signal. Giving an RF signal such fast AM was a bit tricky. First, a fixed amplitude RF-signal at the desired carrier frequency was sent to the L-port of a standard RF mixer. Using an arbitrary function generator (also triggered by the Schmitt) to drive the I-port, the envelope of the RF signal was modulated on the R-port output, essentially driving the mixer “backwards.” In experiments that required two laser drives within 1GHz of the cQED resonances, two RF generators drove EOM1 separably, producing four optical sidebands on the probe beam, of which two served as the coherent drives in the experiment.

Chapter 6

Observations of optical ‘bistability’ in single-atom cavity QED

Conceptually, the experiments described in this chapter are straightforward. A high-finesse, Fabry-Perot cavity containing an atomic TLS strongly coupled and near-resonant with one of its modes is optically driven at and past the point of TLS saturation. A constant quadrature of the optical field transmitted by the Fabry-Perot cavity is continuously monitored with optical homodyne detection, as depicted in Fig. 6.1. Both static and dynamic drives were implemented.

The principle cQED parameters realized in these experiments [KAPM11, KAM10] are $\{g, \kappa, \gamma_{\perp}\} = 2\pi \times \{56.8, 9.3, 2.6\}$ MHz. Although we do our best to minimize variation, the atom-cavity coupling rate g is expected to fluctuate dynamically due to atomic motion in the cavity. Nonetheless, we were able to observe optical ‘bistability’ phenomenon in good quantitative agreement with theoretical predictions assuming a static and near-maximal coupling rate.

6.1 Amplitude ‘bistability’

As analyzed in section 4.1, we made various measurements of the field transmitted by the cavity with atom-drive and cavity-drive detunings such that dynamical switching of the output field would be expected in the amplitude quadrature, a quantum

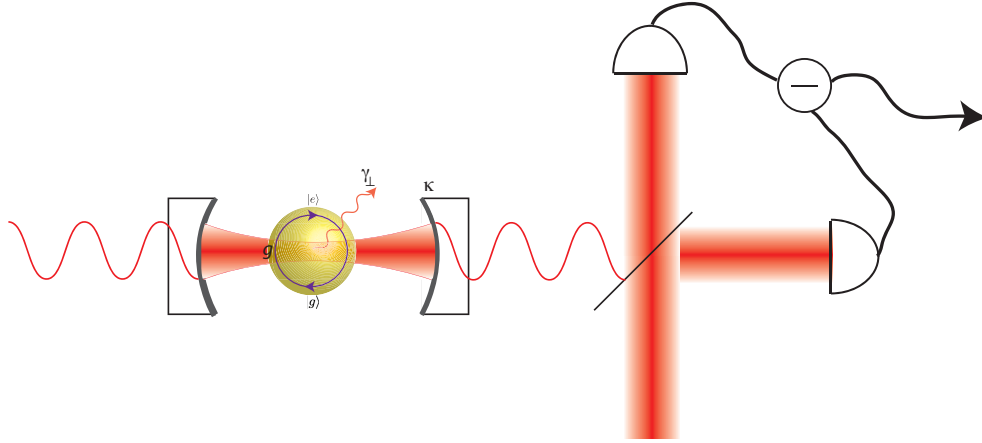


Figure 6.1: A cartoon depiction of the experiments described in this section. The optical field transmitted by a driven cQED system is continuously monitored with high bandwidth optical homodyne detection.

mechanical phenomenon evocative of the I/O dynamics of the analogous ‘semiclassical’ system [KAM10], section 4.1. For example, choosing $\{\Theta, \Delta\} = \{-1.1, .7\}\kappa$, the semiclassical MBE predict a bistable response to a static drive in the $\mathcal{E} = [1.5, 2.3]\kappa$ interval, largely along the ‘+45°’ quadrature, as in Fig. 6.2. For these parameters, the quantum mechanical model, however, predicts a bimodal field steady state distribution along the amplitude quadrature (0°) over a similar range of drive strengths.

Tuning the drive amplitude to the middle of the bimodal regime, and performing homodyne detection of the transmitted field’s amplitude quadrature, we observe photocurrent signals such as in Fig. 6.2c. At $2\mu\text{s}$ (relative to the Schmitt trigger-indicated detection of a maximally coupled atom) the cavity is driven with $\mathcal{E} = 2.6\kappa$ (this, and all subsequent data has been analog post-filtered to 20MHz bandwidth for clarity). The measured photocurrent immediately begins to switch between high and low values, until at $14\mu\text{s}$ the photocurrent abruptly settles down to the intermediate amplitude and shot-noise variance expected for the transmission of an empty cavity. The clear interpretation of these traces is that the large variance signals (both higher and lower than the empty cavity-transmission) are due to the presence of a near-maximally coupled atom in the cavity (section 4.1). The abrupt transition from a high- to a low-variance signal occurs when the atom is lost to the system, either

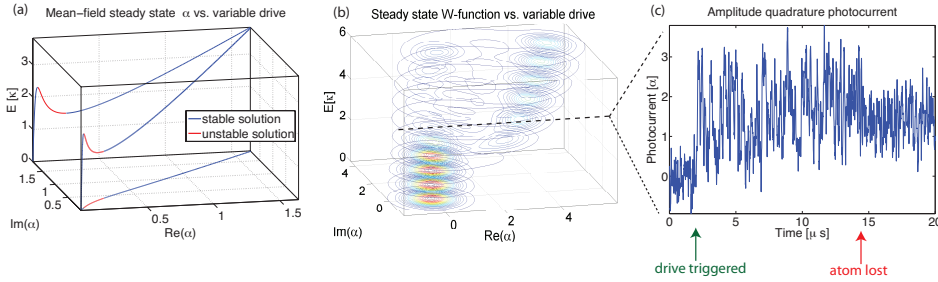


Figure 6.2: (from [KAM10]) (a), Steady-state intracavity field amplitude α from the MBE as a function of the cavity drive amplitude \mathcal{E} for the experimental system with $\{\Theta, \Delta\} = \{-1.1, .7\}\kappa$. The dynamical stability of the steady-state solutions is depicted in red and blue. (b), Wigner functions of the steady-state cavity field from the quantum model as a function of drive amplitude for the same parameters as (a). (c), Sample trace of amplitude quadrature homodyne measurement of the transmitted field during an atom transit, as described in the text, with the drive turned on at $t = 2\mu\text{s}$ and held at $\mathcal{E} = 2.6\kappa$.

because of pumping into the Cs $F = 3$ ‘dark’ ground state or the atom exiting the cavity. In fact, in this representative trace, the switching variance appears to slowly decrease from a maximal value at $2\mu\text{s}$ before the abrupt loss at $14\mu\text{s}$. This is consistent with the expectation that the atom coupling is also a dynamic variable, with smaller effective g ’s typically yielding less splitting between the steady state intracavity lobes, and thus also lower variance homodyne signals.

By taking the largest variance, few- μs sections of photocurrent signals from various experimental configurations, we can compare our data to the steady state I/O response predicted by the quantum mechanical model. With $\{\Theta, \Delta, \mathcal{E}\} = \{-1.1, .7, 2.6\}\kappa$ (using the 20MHz bandwidth and calibrated detection efficiency that would vary from 10% to 20% – due to free-space mode-matching drifts in the homodyne detector), a Wigner-function representation of the cavity-transmitted field appears as a amplitude-quadrature ($\theta = 0$) bimodal distribution in Fig. 6.3a (section 2.1.3). Thus, for this cw drive, steady state amplitude quadrature homodyne photocurrents should be sampled from a bimodal distribution and phase quadrature ($\theta = \pi/2$) measurements should be sampled from a normal distribution, as in Fig. 6.3d. The distribution of accumulated, maximum variance photocurrent data from both quadrature measurements

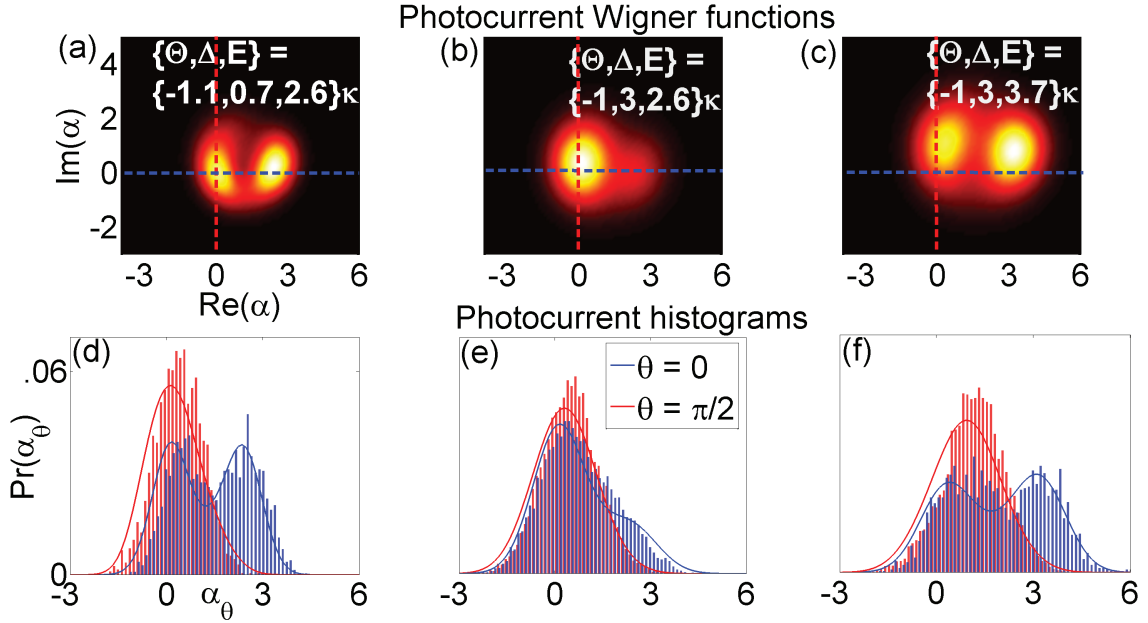


Figure 6.3: (from [KAM10]) (a-c), Wigner function representations of the expected steady state photocurrent distributions, using calibrated detection efficiencies and bandwidths, for three sets of detuning and drive parameters. (d-f), Histograms representing the phase- ($\alpha_{\pi/2}$) and amplitude-quadrature (α_0) photocurrent distributions from ensembles of the highest-variance segments, for the same drive parameters. The histograms are compared with theoretically expected distributions obtained from corresponding Wigner functions (a-c), respectively.

matches the expected distributions calculated from the Wigner representation. Exploring other parameter ranges, further detuning the probe from the atom such that $\{\Theta, \Delta, \mathcal{E}\} = \{-1, 3, 2.6\}\kappa$, rather than an equal-bimodal distribution, the steady state population is expected to be biased toward the low-amplitude state, as the drive threshold for atomic saturation increases with $|\Delta|$. Again, measurements of both quadratures correspond well with the predicted marginal distributions in Fig. 6.3e. Finally, increasing the drive into the saturation regime to $\{\Theta, \Delta, \mathcal{E}\} = \{-1, 3, 3.7\}\kappa$, an even, bimodal distribution in the amplitude quadrature is both expected and observed in Fig. 6.3f. All the data in Fig. 6.3 are in agreement with quantum theoretical predictions despite the use of a somewhat idealized model that assumes a static coupling rate g (whereas g actually depends upon atomic position and Zeeman

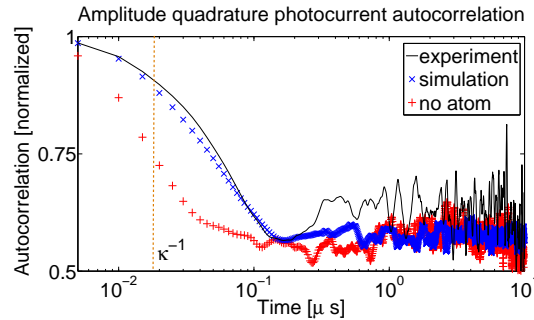


Figure 6.4: (from [KAM10]) The autocorrelation function for the same amplitude quadrature photocurrent data presented as a histogram in Fig. 6.3d is displayed in black. Blue crosses represent the autocorrelation of photocurrents simulated by quantum trajectory methods for identical parameters. The autocorrelation of these quasi-bistable signals is enhanced relative to normalized experimental empty cavity transmission data (red pluses), also presented here with a 20MHz analog bandwidth, and the $\kappa^{-1} = 17\text{ns}$ cavity decay time (dashed orange line).

sub-state, and can vary within a photocurrent segment because of atomic motion and optical pumping). Although it may be possible to apply quantum smoothing techniques [Tsa09] to estimate time-varying atomic coupling trajectories on a shot-by-shot basis from the data, I used a simple fixed effective value $g = .8 \times g_0$ in the analysis for all three parameter sets (the only fit in Fig. 6.3). Quantum trajectory simulations further suggest that this approximation of fixed g and the finite (20 MHz) bandwidth of the presented homodyne signals account for slight mismatches between theory and experiment in the amplitude quadrature splitting and phase-quadrature mean in the three data sets.

As predicted in section 4.1, even in the single-atom, ~ 10 photon regime, distinct high- and low-amplitude states of the output field are expected. Signatures of this remnant optical bistability are visible in the bimodal output photocurrents of Fig. 6.3. Similarly, we see from the same data in Fig. 6.4 that although the output field switches spontaneously when an atom is present in the cavity, it remains correlated over timescales much longer than that of light transmitted through an empty cavity. This atom-induced memory effect can be seen as a quantum remnant of semiclassical optical bistability, where classically the high- and low-amplitude states are truly stable (due to negligible fluctuations in the system) and would therefore exhibit infinite

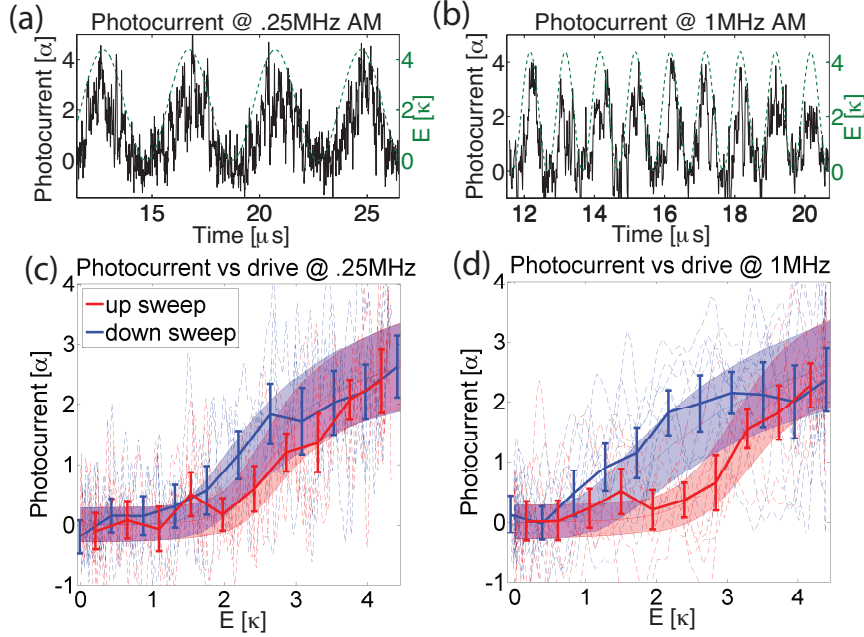


Figure 6.5: (from [KAM10]) (a-b), Single-shot, amplitude quadrature measurements as the drive amplitude is swept at .25MHz and 1MHz, respectively. Black traces are 20MHz bandwidth photocurrents while the green, dashed traces represent the instantaneous drive amplitude. (c-d), dashed red (blue) traces portray the same photocurrent data in (a) and (b), respectively, as a function of the instantaneous increasing (decreasing) drive amplitude. Error bars represent sample mean and variance of the same photocurrents within non-overlapping drive amplitude intervals. Red and blue regions represent theoretically expected photocurrent mean and sample variance as a function of instantaneous drive (section 2.1.3).

correlation time. Consequently, it should also be possible to observe the hysteretic amplitude response characteristic of semiclassical optical bistability by modulating the system drive slowly compared to the timescale for relaxation of the intracavity field (set in our case by the cavity decay time) but rapidly compared to the ‘metastable’ memory timescale indicated in Fig. 6.4. Accordingly, the data in Fig. 6.5 were obtained by recording amplitude-quadrature homodyne photocurrents while sweeping the drive strength sinusoidally at 0.25MHz or 1MHz. Figs. 6.5a and 6.5b depict representative single-shot photocurrent segments with $\{\Theta, \Delta\} = \{-1.1, .7\}\kappa$ encompassing several cycles of sinusoidal drive amplitude modulation (AM) spanning the steady state bimodal region. Increases in both the mean and variance of the output

photocurrent, largely in phase with the drive amplitude, can be discerned in both of these real-time plots. However, plotting the photocurrent as a function of the instantaneous drive amplitude (Figs. 6.5c and 6.5d) reveals a significant hysteresis in the system response at 1MHz AM that is barely noticeable at the more adiabatic .25MHz AM rate. Whereas the response of the empty cavity is linear and non-hysteretic with fixed (shot-noise) output photocurrent variance at these modulation frequencies, nonlinear increases in the signal mean and variance are evident in both traces at mid-sweep. At 1MHz AM, a hysteresis loop appears to open between the upward and downward drive amplitude sweeps, with the low (high) state persisting over a wider range of increasing (decreasing) drive amplitudes than at .25MHz AM. These data are in agreement with theoretical predictions again assuming a fixed value of $g = .8 \times g_0$. It can also be shown that the slight elevation of the experimental high-amplitude branch in Fig. 6.5d is also consistent with slight fluctuation in g over the entire sequence, as in Fig. 6.3d.

6.2 Phase ‘bistability’

If we drive the cQED system harder and on-resonance [KAPM11], we move into a different I/O response regime, physically distinct from the absorptive ‘bistability’ behavior. As described in section 4.2.2, in the strong-driving limit, the atom becomes fully saturated and is forced to choose a dipole orientation either in- or completely-out of phase with the laser drive. The orientation of the dipole determines the phase of the field the atom re-radiates into the cavity, either $\pm 90^\circ$ out of phase with the drive (i.e. in phase with the ‘velocity’ of the electric dipole).

Rather than drive the cQED system completely on resonance, we found that significantly improved data could be obtained by tuning both the drive and the cavity resonance slightly to the red of the atomic transition (i.e. $\Theta = 0$, $\Delta \approx \kappa > 0$). We attribute this signal enhancement to an attractive optical dipole force that tends to draw the atom towards the maximally-coupled cavity anti-node positions. Luckily, this opto-mechanical effect on the atom is apparently significant for $\Delta \approx \kappa$, but the population distribution of the low- and high-phase states is barely perturbed,

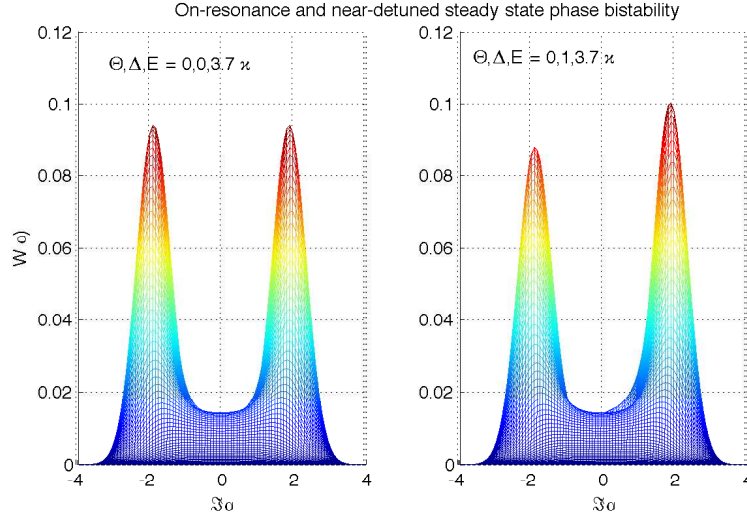


Figure 6.6: Phase quadrature perspective of the steady state intracavity field Wigner function for the drive parameters $\{\Theta, \Delta, \mathcal{E}\} = \{0, 0, 3.7\}\kappa$ (Left) and $\{\Theta, \Delta, \mathcal{E}\} = \{0, 1, 3.7\}\kappa$ (Right).

so that the I/O response is nearly identical to the on-resonance case, see Fig. 6.6. Taking the parameters $\{\Theta, \Delta, E\} = \{0, 1, 3.7\}\kappa$, the phase quadrature photocurrent measured during an atom transit show clear, binary switching between positive and negative phase-shifted states in Fig. 6.7. The photocurrent segment (again, recorded at 200MS/s but displayed with 20MHz bandwidth for clarity) resembles a random telegraph with added Gaussian noise, featuring sporadic jumps between levels indicating positive and negative phase shifts of the transmitted optical beam. Such signals stand as a marked improvement over our previous observations of TLS-induced phase *noise* (as opposed to clear, binary phase switching) in Mike Armen’s thesis work [Arm09], and more convincingly support long-standing theoretical predictions [AC91] summarized in section 4.2.2. For example, the photocurrent histogram in Fig. 6.7b suggests a dual-Gaussian distribution in this single shot segment, whereas only “flat-top” distributions were previously visible after averaging many single-shot signals in [AMM09]. Although a complex physical model is required to describe the TLS-cavity system (section 3.2), the output of a device that possibly could function as a random binary phase modulator should also be well described by a two-state,

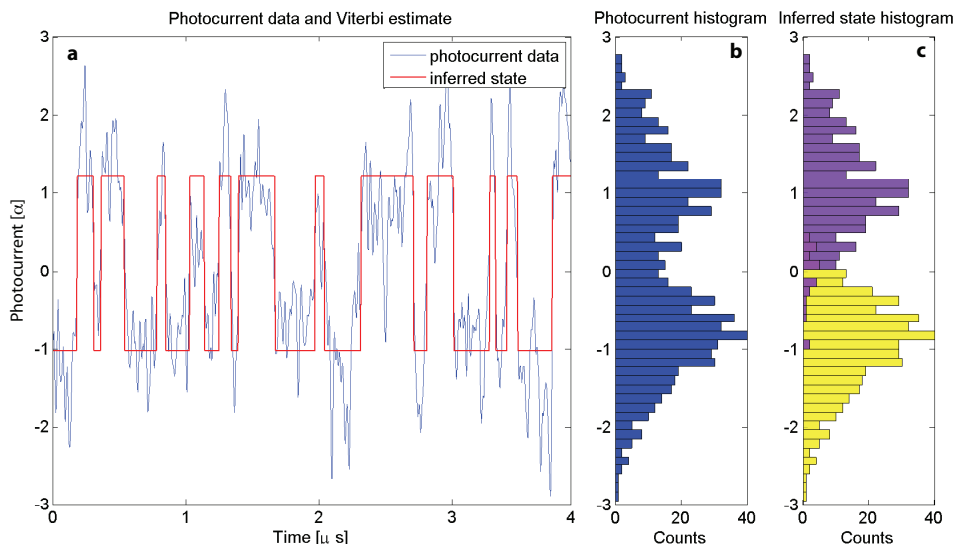


Figure 6.7: (from [KAPM11]) (a), An experimental phase-quadrature homodyne photocurrent segment taken with $\{\Theta, \Delta, E\} = \{0, 1, 3.7\}\kappa$ is shown in blue. The red overlay is the decoded binary signal produced by the Viterbi algorithm with hidden Markov model parameters obtained via expectation maximization for this segment. (b), A histogram of the photocurrent data segment from (a), displaying a dual-Gaussian distribution consistent with binary phase modulation. (c), Dual histograms of the photocurrent data, each taking counts only when the Viterbi path occupies the positive or negative state.

time-invariant hidden Markov model (HMM) [CMR05]. Allowing for unequal transition rates between the two HMM states and assuming only that each state produces normally-distributed (but otherwise unspecified) photocurrent, it is possible to apply a standard expectation maximization (EM) algorithm [Wel03, CMR05] to full-bandwidth photocurrent data segments to find HMM parameters that best fit the data. The red trace overlay in Fig. 6.7a represents the decoded binary signal produced by the Viterbi algorithm [Vit67, CMR05] using optimal parameters from the EM procedure applied to the same trace. The histograms in Fig. 6.7c were constructed by segregating the photocurrent according the Viterbi path, which apparently results in two near-normal distributions, confirming the quality of the binary decoding. I emphasize that these conditional distributions mainly reflect optical shot-noise but are broadened by random variation of $g(r)$.

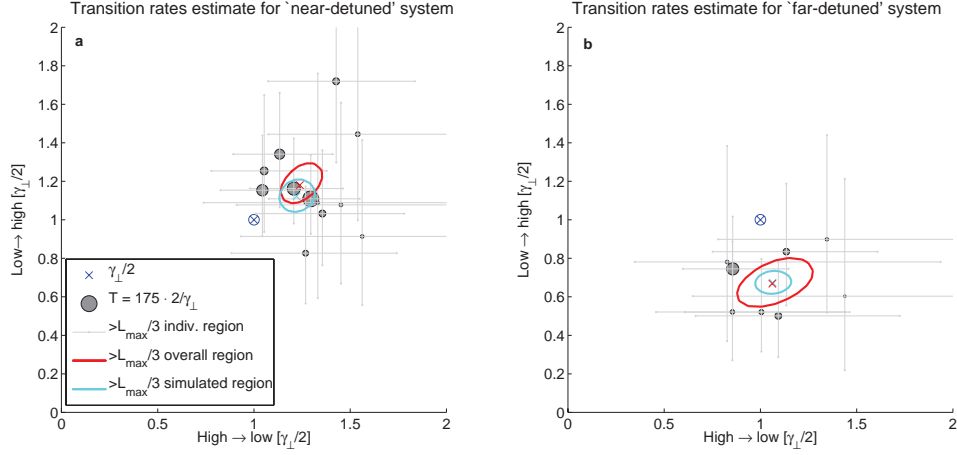


Figure 6.8: (from [KAPM11]) Both plots depict contours of the likelihood functions of hidden Markov model transition rates for low \leftrightarrow high switching. The most likely rate-pairs inferred from data taken from individual atom transit segments are indicated by grey dots, with the diameter of each dot representing the duration of the corresponding data segment. The grey bars represent the intervals over which the likelihood of the individual transits’ rate-pairs are at least 1/3 of their maximum. The red cross locates the most likely rate-pair, given an aggregated segment formed from the individual transit measurements, with the red oval enclosing the region of rate-pair likelihoods that are at least 1/3 of the maximum. The teal cross and oval represent the same likelihood contours produced from simulated data. (a), Likelihood contours for $\{\Theta, \Delta, E\} = \{0, 1, 3.7\}\kappa$. (b), $\{\Theta, \Delta, E\} = \{0, 3, 3.7\}\kappa$.

With the good visibility of the switching states, we can also confirm that binary decoding of the experimental photocurrent segments yields transition rate estimates that match predictions of the full quantum model (section 3.2). The plots in Fig. 6.8 depict contours of the likelihood functions of HMM parameters estimated from individual and aggregated atom transits, obtained under two different input conditions. Fig. 6.8a reflects data acquired from a ‘near-detuned’ system with the same parameters as in Fig. 6.7. The high likelihood of a symmetric switching model apparent here is both theoretically predicted (section 4.2.2) and consistent with the symmetric photocurrent histograms in Fig. 6.7. The slightly greater than $\gamma_{\perp}/2$ switching rates of the most likely models (as opposed to exactly $\gamma_{\perp}/2$, which occurs in the strong-driving limit) is due to the moderate power of the probe. Fig. 6.8b reflects data taken

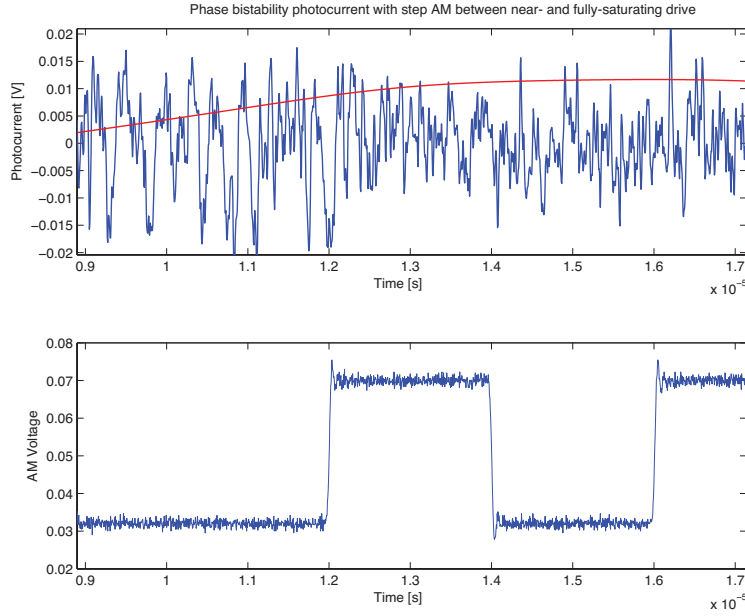


Figure 6.9: Raw photocurrent data from a run in which the drive was amplitude step-modulated between $\mathcal{E} = 3.7\kappa$ and $\mathcal{E} = 7.6\kappa$ with the detunings fixed at $\{\Theta, \Delta\} = \{0, 1\}\kappa$ is shown in the top plot in blue with a 100kHz-10MHz analog bandwidth (the red trace gives the DC-100kHz signal). Bottom, the amplitude modulation voltage that defines the drive amplitude, proportional to \mathcal{E} .

with cavity and probe held 40MHz below atomic resonance. A significant asymmetry in the transition rates is expected and inferred from the likelihood contours. Both figures compare parameter estimates obtained from experimental data to estimates from simulated photocurrent data of comparable aggregate duration and detection efficiency (using quantum trajectory simulations assuming no atomic motion). For both detunings, the likelihood contours for the experimental and simulated signals largely overlap, indicating that the device physics model (section 3.2) also accounts well for the observed binary switching rate statistics, but with no fit parameters.

In principle, the phase ‘bistability’ response simply saturates once the drive is in the $\mathcal{E} \gg g/2$ regime, producing a constant splitting in the bimodal distribution for arbitrary drives (e.g. Fig. 4.8). Unfortunately, in contrast to our group’s first attempt to observe this behavior, atom-induced phase switching was increasingly

rare to see, per atom transit event for drives $E > .8g = 5\kappa$. In contrast to drive amplitudes below this regime (e.g. for $E = .6g = 3.7\kappa$), where phase bistability effects were observed for several to tens of μs , in a majority of atom triggering events in the very high saturation regime, phase bistable effects were rarely seen, and if seen, only persisted for a few μs . We attribute this lack of high-drive data to the strong drive mechanically expelling the atoms from the cavity mode with dipole force effects. The significantly larger atom-cavity coupling in this experiment, $g = 2\pi \times 56.8\text{MHz}$, compared to the earlier iteration, $g = 2\pi \times 16\text{MHz}$ [Arm09, AMM09], means that the same opto-mechanical forces $\propto \nabla g(\mathbf{r})\sqrt{\bar{n}}$ present in this experiment occurred at ~ 13 times greater intracavity photons in the previous experiment. As the quality of the phase bistability data in that experiment began to peter out at about $\bar{n} \approx 110$, with shorter and shorter visible phase noise segments [Arm09], the limitations of both systems seem compatible (note too, that the the earlier iteration was also likely effected by faster dark state-pumping due to large cavity birefringence). Importantly, amplitude step-modulating the drive strength between near- and far-saturating regimes, we see that the high drive state causes the atom-induced phase bistability to be lost, as in Fig. 6.9, rather than phase-bistable effects simply not existing for very large drives. As the drive amplitude is step-modulated between $\bar{n} = 14$ and $\bar{n} = 58$, phase switching is apparent for the initial, low-drive state, but abruptly disappears when the drive is increased, and does not reappear when the drive is switched low again.

Finally, despite our atomic system’s large g/κ ratio, which is unfavorable for the control method simulated in Fig. 4.9, we attempted exert an external, optical control of the switching rate experimentally using the ‘near-detuned’ system. Fig. 6.10 shows inferred ‘total’ transition rates (the mean rate at which switching in either direction occurs) as a function of the power of the control beam, for three different control beam frequencies. In the strong driving limit the optimum control detuning would be 425MHz, but given our moderate signal power the effective coupling energy (and therefore optimal control detuning) should be somewhat smaller. The statistical significance of the data displayed in Fig. 6.10 is marginal, but the data do show consistent trends that match expectations: data taken with -375MHz and -425MHz

control detuning induce higher transition rates with higher power, with -375MHz consistently higher, while the -525MHz detuning induced essentially no net transition increase over the accessible range of control powers (limited by opto-mechanical effects on the high end). Linear fits to data obtained from trajectory simulations reproduce these general trends of the data and confirm the limited degree of control achievable in our experimental system. We thus infer an apparent control energy requirement of only $\sim 1\text{fJ/edge}$ even in our atomic implementation (with unfavorable parameters for efficient control) of the dressed-state binary phase modulator. I’d also like to point out that the data presented in Fig. 6.10 was the last data ever taken in our group’s Varian-Astro era, obtained the night before the lab tear-down for the Nano move!

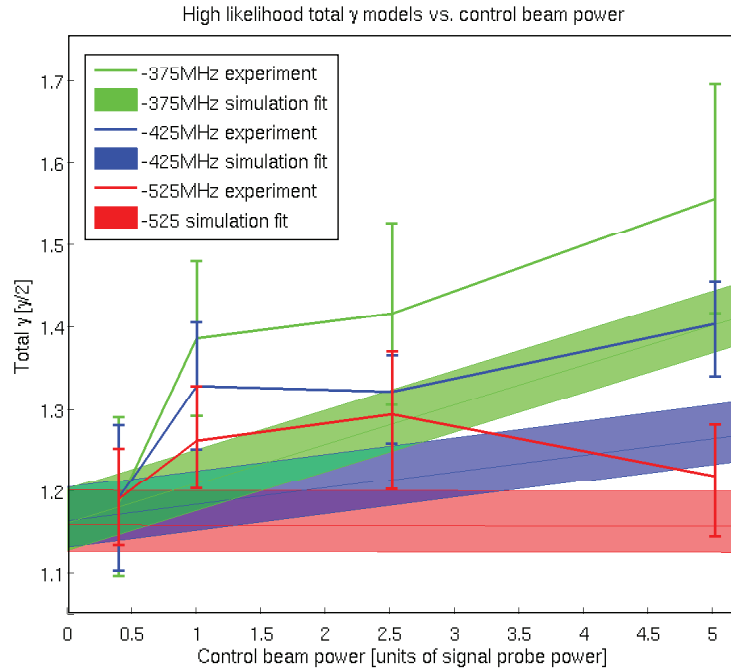


Figure 6.10: (from [KAPM11]) Data points represent inferred ‘total γ ’ for various control beam parameters. The thin lines track the most likely total γ and the confidence intervals represent the range of γ values with at least 1/3 the maximum likelihood. The green, blue and red data points depict the total γ as a function of control power for a control probe detuned by -375MHz, -425MHz, and -525MHz from the signal probe, respectively. The colored shaded regions represent linear best fits of the corresponding confidence intervals based on a simulated data set with perfect detection efficiency and duration several times that of the experimental data. The apparent positive, constant bias in the experimental γ relative to simulation for control powers at least equal to the probe’s is perhaps due to enhanced opto-mechanical motion induced by a strong control beam.

Part III

Autonomous Nanophotonic Quantum Memories

Introduction

Traditional approaches to quantum information theory [NC00] are non-committal to any particular implementation. Instead, the basic concepts are framed in terms of the axiomatic laws of quantum mechanics. This generality is a testament to the simple power of the ideas, and allows for an impossibly large range of experiments to get into the game, from trapped ion-computation [Win09] to liquid state NMR [VSB⁺01]. The fundamentals of quantum information can be explained using the same abstract formalism of quantum mechanics taught to undergraduates, and usually are [NC00].

Because of this, there is a sense that experiments simply have to ‘catch up’ with the established theory of quantum information, that qubits, gates, and measurements that better approximate these simple ideals simply have to be realized. While this is no doubt true, theoretical approaches framed in the natural laws of promising systems are also lacking. It might be inappropriate that next generation quantum information systems with trapped ions implement the same protocols as those made from superconducting microwave circuits. But guided by equivalent, basic models, it’s perhaps inevitable that all breeds of quantum information hardware have so far been driven towards equivalent demonstrations [RRH⁺04, DCG⁺09, CLS⁺04, DRS⁺10, VSB⁺01, PMO09].

In this final part, I describe some of our efforts to develop a method for designing protected quantum memories out of networks of nanophotonic components [KNPM10, KPCM11]. Modeling these systems with a framework based on a *circuit description* of quantum optics, in applying basic quantum error correcting (QEC) concepts we are naturally led to designs that are continuous and stationary in time

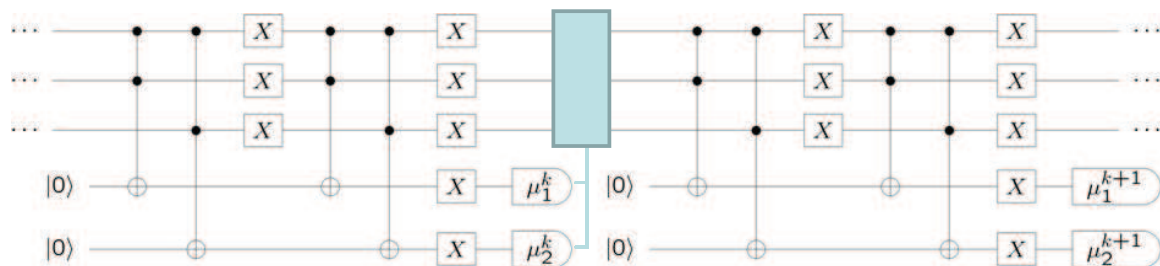


Figure 6.11: An example of a traditional quantum ‘circuit’ that depicts a traditional discrete time version of the 3 qubit bit-flip code described in section 7.1.1.

and operate autonomously. This approach is in contrast to the traditional description of quantum error correction (QEC) [Got09, NC00] involving discrete operations, clocked execution, instantaneous measurement and external corrections. These designs are communicated through circuit schematics, with each ‘block’ representing a physical device, with its own internal dynamics, and each connection between them representing a physical optical field (e.g. Fig. 8.3). The continuous time dynamics of this system are constructed from these diagrams simply by describing them in the quantum circuit formalism based on quantum stochastic differential equations (QSDEs) (part I). Again, we like to contrast these schematics with traditional, so-called ‘quantum circuit’ diagrams composed of blocks representing discrete operations, not devices, and the connections between them defining a chronology, not a physical coupling (e.g. Fig. 6.11) [NC00]. Our designs are much more like an electrical schematic that represents a specific hardware construction, while the traditional schematic representation is more like a high-level programming language.

Moreover, these all-optical network designs naturally sidestep the difficulty of having to build a distinct, *classical* apparatus operating in parallel with the quantum memory, constantly monitoring and maintaining it. Typically, the mechanics of this essential half of a quantum memory system are hardly considered at all, taking a back seat in the analysis to the qubits in which the information is stored. This assumption of a perfect, classical overseer glosses over the inherent technological mismatch of typically fast, nanoscale and cold quantum systems with slow, mesoscopic, and/or hot classical ones. The extreme performance demands for quantum information processing should motivate solutions that weigh classical and quantum resources

wholistically and utilize system models as close to physical mechanics as possible. Not only do our photonic networks model both the memory and controller on equal footing, but they do so in a technologically homogenous context.

Chapter 7

Preliminary Models

The focus of the work described in this final part has been the design of nanophotonic networks that could form a protected quantum memory element and require a minimum of external maintenance. Before we can get to the full designs, though, basic concepts of quantum error correction, and the intuition behind and continuous-time models of the nanophotonic components need to be introduced.

7.1 Quantum error correction

Quantum error correction (QEC) addresses the problem of how to do ‘nothing’ [Got09, NC00]. Simply staying in the same state for an extended period of time is difficult for quantum objects, especially for highly entangled, many body systems. Uncontrolled, unmonitored interactions between a quantum state we’d like to preserve and its environment generally ruin the utility of the stored state. While noise is a problem in classical memory banks too, of course, the problem of preserving a single *qubit* of quantum information is more subtle. For instance, we can’t simply copy a state to protect it through redundancy; measuring quantum states to diagnose errors will perturb the states in general; and errors on spin-1/2 qubits are usually continuous rotations, not discrete operations [NC00]. Rather than summarize the general theories of stabilizer QEC [Got09], I will directly explain the operation of three basic quantum codes our networks emulate.

7.1.1 The bit-flip and phase-flip codes

A qubit is a two-level system (TLS) whose state represents a quantum informational resource. The general qubit state is

$$|\tilde{\psi}\rangle = \alpha|1\rangle + \beta|0\rangle, \quad |\alpha|^2 + |\beta|^2 = 1. \quad (7.1)$$

This qubit state may be easily corrupted, for example, by an arbitrary X -rotation induced, perhaps, by a stray magnetic field:

$$e^{i\theta X}|\tilde{\psi}\rangle = \cos(\theta)(\alpha|1\rangle + \beta|0\rangle) + i\sin(\theta)(\alpha|0\rangle + \beta|1\rangle) \quad (7.2)$$

While a known interaction like $e^{i\theta X}$ may be reversed perfectly, the continuum of available “errors” that could occur renders a simple TLS extremely vulnerable to such disturbances. As perfect calibration of the environment is impossible, the exact angle of rotation cannot be known for sure and perfect compensation for these types of errors is impossible.

A qubit need not be a single object, however, but simply a two-dimensional subspace in, perhaps, a multi-body system. For instance, the *logical qubit*

$$|\tilde{\psi}\rangle = \alpha|1\rangle + \beta|0\rangle, \quad (7.3)$$

may be encoded in the two-dimensional, completely symmetric subspace of a physical memory element composed of three TLSs:

$$|\tilde{\psi}\rangle \rightarrow |\psi\rangle = \alpha|111\rangle + \beta|000\rangle, \quad (7.4)$$

where $|111\rangle$ ($|000\rangle$) refers to the state of all three TLS jointly in their $|1\rangle$ ($|0\rangle$) state. The particular state of the logical qubit is sometimes referred to as the *codeword*.

Now suppose during a brief storage period there is a $p_i \ll 1$ probability that each TLS i is ‘bit-flipped’ by an environmental disturbance, inducing the transformation

Z_1Z_2 result	Z_2Z_3 result	syndrome subspace
+1	+1	$\text{span}\{ 111\rangle, 000\rangle\}$
-1	+1	$\text{span}\{ 011\rangle, 100\rangle\}$
+1	-1	$\text{span}\{ 110\rangle, 001\rangle\}$
-1	-1	$\text{span}\{ 101\rangle, 010\rangle\}$

Table 7.1: Right column, the possible subspaces that a 3-TLS system may project into as a result of pair-wise bit-parity measurements. The left two columns list the corresponding Z_1Z_2 and Z_2Z_3 parity measurement results that project the system into each subspace.

$|1\rangle \leftrightarrow |0\rangle$. Thus, after the storage period the (unmonitored) state of the system is

$$|\psi\rangle\langle\psi| \equiv \rho_\psi \rightarrow \rho_\psi \left(1 - \sum_{i=1}^3 p_i\right) + \sum_{i=1}^3 p_i X_i \rho_\psi X_i \quad (7.5)$$

where X_i acts as the X -Pauli operator on TLS i , and we consider the probability of multiple bit-flips negligible. It may look like we're in more trouble than we were with a single TLS, but we're actually better off. If we now measure the two-TLS *parity operator* Z_1Z_2 , a +1 result will mean that the system either suffered no error (ρ_ψ) or an X_3 -type error ($X_3\rho_\psi X_3$), while a -1 result will mean we know the system suffered a X_1 or X_2 error. Further measuring the Z_2Z_3 parity operator will fully specify the error *syndrome*, according to table 7.1. For example, if we get a +1 result for Z_1Z_2 and a -1 result for Z_2Z_3 , we learn that the system is in the state $X_3\rho_\psi X_3$. Now, to recover the state ρ_ψ , we simply apply another 'bit-flip' to the third TLS ($X_3^2\rho_\psi X_3^2 = \rho_\psi$). This is parity measurement and recovery strategy is known as the *three-qubit bit-flip code* [Got09, NC00].

In a classical, majority-rule bit-flip error correcting code we can simply measure the state of each bit and if most are '1' we rule that the originally encoded state was probably '111.' In a quantum code, we cannot simply measure each qubit separably because while doing so will specify the type of bit-flip error that occurred (if any), the information-carrying quantum superposition in the original state, $\alpha|111\rangle + \beta|000\rangle$, will be destroyed. It is thus critical that we only measure qubit parities, which do not reveal if the TLSs are either 'up' or 'down.'

In the above bit-flip code example we presumed a very specific error model, either TLS bit-flips occurred or they didn't, which may seem a serious limitation if our errors are more likely to be continuous rotations. However, one of the most powerful concepts in QEC is that if a code can correct for the random application of error operators $\{E\}$, then it can also correct for the random application of arbitrary linear combinations of $\{E\}$ [NC00]. Thus, since the bit-flip code works in the above $p_i \ll 1$ example where $\{E\} = \{I, X_1, X_2, X_3\}$, it also works when $\{E\} = \exp[i\theta\{I, X_1, X_2, X_3\}]$. This remarkable result can be understood as a consequence of the measurement procedure *discretizing* 'analog' errors. Even if a possible bit-rotation acting on TLS i is not $\theta = \pi/2$, measuring Z_1Z_2 and Z_2Z_3 forces the system into either $|\psi\rangle$ or $X_i|\psi\rangle$. Thus, although continuous error models are appropriate in quantum information systems, QEC has more in common with digital classical error correction than (famously impractical) analog error correction.

However, what about the finite possibility in the bit-flip example that multiple bit-flip errors occur? In these cases, the strategy fails: if the first two TLSs flip, the algorithm will erroneously determine that the third TLS flipped and apply the wrong correction. Hence, the general notion is that QEC has to be done repeatedly and rapidly enough such that the likelihood of multiple, independent single-TLS errors is negligible. Moreover, what if the errors are of a different sort, such as Z -rotations? Z -errors map $|1\rangle \rightarrow |1\rangle$ and $|0\rangle \rightarrow -|0\rangle$, and are consequently known as *phase errors*. Again, the bit-flip code is helpless against such error types. However, if these are the only type of error affecting each TLS, we can apply an analogous strategy and encode

$$|\tilde{\psi}\rangle \rightarrow |\psi\rangle = \alpha|+++ \rangle + \beta|--- \rangle, \quad (7.6)$$

where $|\pm\rangle = \frac{1}{\sqrt{2}}(|1\rangle \pm |0\rangle)$, and measure the phase-parity operators X_1X_2 and X_2X_3 , performing the analogous error decoding and recovery. This *three qubit phase-flip code* is related to the bit-flip code via a simple basis change, and shares the analogous advantages and limitations.

While very promising, both codes are also very limited, only capable of protecting against a narrow class of errors. To make more powerful, general QEC codes, a

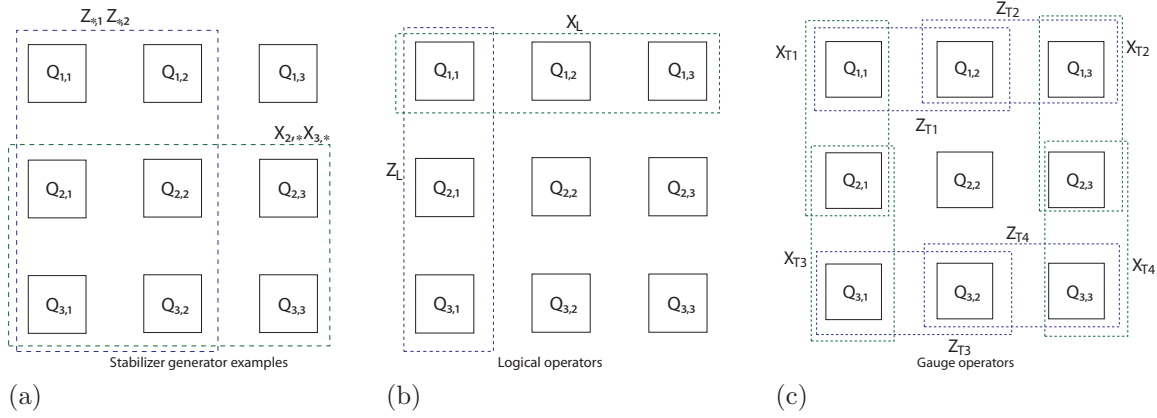


Figure 7.1: (a), Two of the stabilizer generators in the 9 qubit Bacon-Shor code. One stabilizer generator acts as the Z operator on all qubits in the first two columns, the other generator shown acts as X on all qubits in the last two rows (the remaining two stabilizer generators are not shown for clarity). (b), Logical operators that act on the 2D subsystem \mathcal{L} in the no-error subspace: boxes again indicate Z (blue) and X (green) acting on all enclosed qubits. (c), One choice for the remaining gauge operators that act on the remaining, 4-qubit \mathcal{T} subsystem in the no error subspace.

memory element composed of more TLSs is needed.

7.1.2 The 9 qubit Bacon-Shor code

Abstractly, the three-qubit codes in the previous section took the strategy of decomposing a multibody Hilbert space into

$$\mathcal{H} = \mathcal{L} \oplus \mathcal{E} \quad (7.7)$$

where \mathcal{L} is a 2-dimensional ‘logical space’ in which the logical qubit is encoded. Any states in \mathcal{E} are deemed errorful. A generalization of this subspace-coding strategy is a *subsystem* code [KLP05] in which a multibody Hilbert space is decomposed into

$$\mathcal{H} = (\mathcal{L} \otimes \mathcal{T}) \oplus \mathcal{E} \quad (7.8)$$

where now information is encoded in the \mathcal{L} subsystem and any state in \mathcal{E} is in error. Thus, while a valid logical state has the form

$$\rho_\psi = (\rho_{\mathcal{L}} \otimes \rho_{\mathcal{T}}) \oplus 0 \quad (7.9)$$

the state of the ‘gauge subsystem’ $\rho_{\mathcal{T}}$ carries no information, and may be scrambled without consequence. This general strategy is exploited by another famous code, the 9 qubit Bacon-Shor subsystem QEC code [Bac06], which is the smallest of a class of naturally fault-tolerant QEC codes [Got09, NC00] capable of protecting a single logical qubit from *arbitrary* single-TLS errors.

In this code, 9 TLSs are arranged in a 3×3 grid, as in Figs. 7.1. In this configuration, a non-Abelian operator group is the set of operators generated by pairs of X operators acting on adjacent-row TLSs and pairs of Z operators acting on adjacent-column TLSs

$$\mathcal{T} = \langle X_{i,j} X_{i+1,j}, Z_{j,i} Z_{j,i+1} | i \in \mathbb{Z}_2, j \in \mathbb{Z}_3 \rangle, \quad (7.10)$$

where $X_{i,j}$ and $Z_{i,j}$ act as Pauli operators on the TLS in row i , column j and as the identity on all others. An Abelian subgroup $\mathcal{S} \subset \mathcal{T}$ known as the ‘stabilizer’ group is generated by X operators acting on all TLSs in two adjacent rows and Z operators acting on all TLSs in two adjacent columns

$$\mathcal{S} = \langle X_{i,*} X_{i+1,*}, Z_{*,i} Z_{*,i+1} | i \in \mathbb{Z}_2 \rangle, \quad (7.11)$$

as depicted in Fig. 7.1a. These generators of the stabilizer group play the same role as the parity operators $Z_1 Z_2$ and $Z_2 Z_3$ in the three qubit bit-flip code: measuring them reveals which errors have occurred to the 9 TLS system. That is, the ± 1 eigenvalues of the generators of \mathcal{S} may be used to label subspaces of the $\mathcal{H} = (\mathbb{C}^2)^{\otimes 9}$ system Hilbert space

$$\mathcal{H} = \bigoplus_{\vec{a}} \mathcal{H}_{\vec{a}}, \quad (7.12)$$

where \vec{a} is a string of the four binary eigenvalues of the stabilizer generators and each $\mathcal{H}_{\vec{a}}$ represents a 2^5 -dimensional space. Each $\mathcal{H}_{\vec{a}}$ may be further decomposed into

subsystems

$$\mathcal{H}_{\vec{a}} = \mathcal{H}_{\vec{a}}^{\mathcal{L}} \otimes \mathcal{H}_{\vec{a}}^{\mathcal{T}} \quad (7.13)$$

where elements from \mathcal{T} (which commute with \mathcal{S}) act non-trivially on some $\mathcal{H}_{\vec{a}}^{\mathcal{T}}$, and as the identity on $\mathcal{H}_{\vec{a}}^{\mathcal{L}}$, encoding four ‘gauge’ qubits, modulo \mathcal{S} . This action leaves the $\mathcal{H}_{\vec{a}}^{\mathcal{L}}$ as single-qubit subsystems, in one of which our logical qubit is stored. We can choose this logical qubit to be the one encoded by the operators $X_L = X_{1,*}$ and $Z_L = Z_{*,1}$ in the $\vec{a} = \{+1, +1, +1, +1\}$ subspace (such that, for example, $X_L|1_{\mathcal{L}}, \psi_{\mathcal{T}}\rangle = |0_{\mathcal{L}}, \psi_{\mathcal{T}}\rangle$), as shown in Fig. 7.1b. The other four gauge qubits that live in this subspace’s $\mathcal{H}_{\vec{a}=1^{\otimes 4}}^{\mathcal{T}}$ subsystem may be specified by four commuting pairs of anticommuting operators in \mathcal{T} : $\{X_{Ti}, Z_{Ti}|i \in \mathbb{Z}_4\}$, as in Fig. 7.1c. Again, although a valid code state will define some state on these gauge qubits, they will have no information encoded in them and may be scrambled in the QEC procedure without consequence.

In the 9 qubit code, the encoded codeword may be rendered impervious to arbitrary single-TLS rotations of any of the nine TLSs, although the state of the gauge qubits may be depolarized. Measurement of the four stabilizer generators “discretizes” any partial qubit rotations, projecting the system state into some error space $\mathcal{H}_{\vec{a}}$, with $\vec{a} = \{+1, +1, +1, +1\}$ being the “no error” space. The results of these syndrome measurements localize Pauli- X errors down to the column in which they occurred, Pauli- Z down to the row, and Pauli- Y errors down to the TLS. Although the precise location of the error is not known generally, codeword recovery is achieved by applying a Pauli- X ($-Z$) to *any* qubit in the same column (row) as a detected bit-flip (phase-flip) error. For example, if a partial Pauli- Y rotation occurs to TLS $Q_{2,2}$ (the middle TLS in the 3×3 grid), syndrome measurement may project the system into the $\vec{a} = \{-1, -1, -1, -1\}$ subspace, digitizing and indicating the error. The encoded codeword may be recovered by then applying the operator $X_{3,2}Z_{2,1}$, as the net, recovery-error operator, $X_{3,2}Z_{2,1}Y_{2,2}$, commutes with \mathcal{S} , X_L and Z_L . However, $X_{3,2}Z_{2,1}Y_{2,2} \in \mathcal{T}$ and thus the recovery operation disturbs the state of the gauge qubits. Moreover, remarkably, the error syndrome need not be acquired by directly measuring the 6-body operator generators. Separably measuring the 2-body generators of \mathcal{T} yields the same syndrome information as the generators of \mathcal{S} and

although such measurements perturb the gauge qubits, they commute with X_L and Z_L and thus preserve the codeword [AC07].

7.2 cQED parity networks

From the previous sections, it is apparent that multibody parity measurements are at the heart of many QEC protocols. However, the physically abstracted models used above presume perfect and instantaneous projective measurements. This is an idealization: any actual measurement takes a certain amount of time, no measurement is perfect and perfect TLSs do not exist. Physical systems operate according to continuous time laws. Moreover, *weak measurement*, in which partial information is gained incrementally in time, is usually (if not always) a more accurate physical description of a measurement process.

We are interested in modeling how a system of nanophotonic devices could emulate the key concepts of QEC in the context of their own, natural dynamics. One motivator, the binary TLS model leads us to consider nanophotonic systems with ‘atoms,’ while another, the desire for a physical, continuous time description of these systems and their measurement process immediately leads us to consider quantum stochastic differential equation (QSDE) models (chapter 1).

7.2.1 Physical model of a cQED TLS

The central object in our nanophotonic QEC networks are cQED devices that should increasingly approximate a continuously measurable TLS as the volume of the device vanishes [KBSM09]. The physical intuition of these devices is represented in Fig. 7.2. If an optical pulse encounters an ultra-high reflector, the pulse is simply reflected with a π phase flip. If that same mirror is matched with a perfect reflector, so that an optical resonator is formed between them, when a resonant optical pulse reflects off the front mirror, it will instead be reflected with no net phase shift (in the limit that the duration of the pulse is greater than the inverse of the field decay rate of the resonator). If that same resonator contains a TLS with a degenerate and

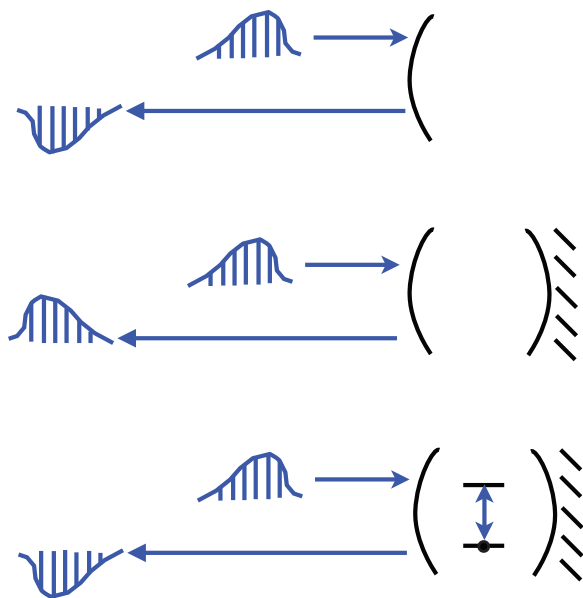


Figure 7.2: Top, when an optical pulse scatters from a high reflector, it does so with a π optical phase shift. Middle, when the same pulse scatters off of a resonant, single-sided cavity (with a fast field decay rate), it scatters with no net phase shift. Bottom, if that same cavity also contains a strongly coupled atom (and the pulse isn't too strong), the optical pulse does not excite the cavity and again reflects off the front reflector with a π phase shift.

strongly coupled optical transition between the two states, then (in the limit that the coupling is also very large) the coupled TLS will prevent an applied optical pulse from entering the resonator. Therefore, the cQED system looks like a simple high reflector to the pulse, and it will reflect off with a π phase flip. By probing a cavity containing a multilevel atom with a resonant pulse and measuring the phase of the reflection, we can determine whether or not the atom is in a strongly coupled state [DK04, KBSM09]. Note that this argument implies that the system parameters need to simply respect a certain hierarchy, rather than finely tuned ratios: the field decay rate and atom coupling need to be fast, while the pulse should be slow (the atom, cavity and pulse should all be roughly co-resonant, however).

In our cQED TLSs [KBSM09], the single-sided resonators contain multilevel ‘atoms’ or comparable solid-state emitters. As represented by the blue transitions in Fig.

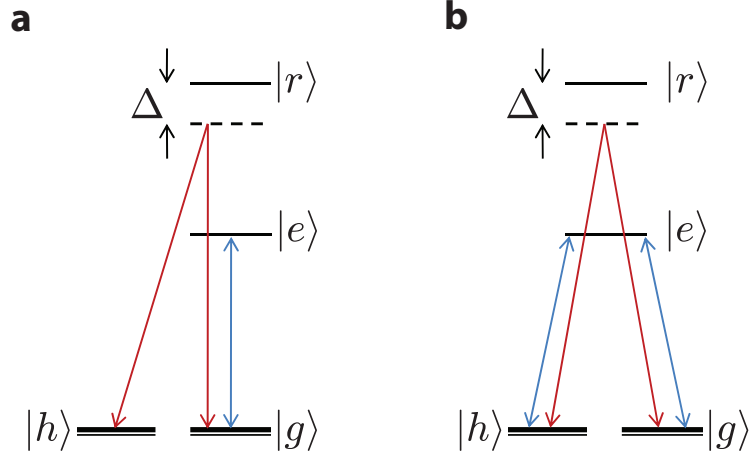


Figure 7.3: (from [KNPM10]) Atomic level diagrams of (a), Z probe interaction, (b) X probe interaction.

7.3, Z and X probe interactions emerge from a three level atomic system in a λ -configuration interacting with a quantized mode of a single-sided cavity. In the case of the Z probe, the $|g\rangle \leftrightarrow |e\rangle$ transition is strongly coupled and on resonance with the cavity mode, while the $|h\rangle$ state is fully uncoupled. In the case of the X probe, both $|g\rangle \leftrightarrow |e\rangle$ and $|h\rangle \leftrightarrow |e\rangle$ transitions are simultaneously coupled and on resonance with the cavity mode. The X probe configuration could be realized with a degenerate spin ± 1 ground state pair coupled to an excited spin-0 state via a linearly polarized cavity mode, for example. Thus, in a properly rotating frame and applying the usual rotating wave approximation, the familiar Jaynes-Cummings Hamiltonian interaction for both systems is (section 3.1)

$$H_i = ig_c(\sigma^\dagger a - \sigma a^\dagger) \quad (7.14)$$

where a is the cavity mode annihilation operator, the atomic ‘lowering operators’ act as $\sigma = |g\rangle\langle e|$ on the atomic states in the Z -probe device, $\sigma = \frac{1}{\sqrt{2}}(|g\rangle + |h\rangle)\langle e|$ in the X -probe device, and the coupling rate g_c may be taken real without loss of generality. The remaining red optical transitions shown in Fig. 7.3 are for Raman interactions discussed in the next chapter.

However, the cavity mode and atom also interact with the free fields that surround

them: the cavity photons will decay out of the resonator and the excited atomic state will spontaneously emit photons into the environment. These interactions are included in a QSDE description of the dynamics with the inclusion of two coupling operators ¹:

$$L_1 = \sqrt{2\kappa}a; \quad L_2 = \sqrt{2\gamma_\perp}\sigma \quad (7.15)$$

where κ and γ_\perp are the cavity field and atomic dipole decay rates, respectively. As there is no direct coupling between the cavity and atomic decay channels, the scattering matrix for this system is the identity. Thus, the QSDE descriptions of the dynamics for the Z and X systems *with vacuum inputs* are characterized by the operator coefficients (see section 1.5)

$$Q = \left(I, \begin{bmatrix} \sqrt{2\kappa}a \\ \sqrt{2\gamma_\perp}\sigma \end{bmatrix}, ig_c(\sigma^\dagger a - \sigma a^\dagger) \right). \quad (7.16)$$

I will eventually use the limiting evolution of these ‘vacuum’ cQED systems in the network model, but note that familiar, *driven* cQED dynamics may be derived with the inclusion of a Weyl operator (Eq. 1.33) in series product with the vacuum system (representing an on-resonance, cw laser input to the cavity mode)

$$\begin{aligned} Q^\alpha &= Q \triangleleft \left(I, \begin{bmatrix} \alpha \\ 0 \end{bmatrix}, 0 \right) \\ &= \left(I, \begin{bmatrix} \sqrt{2\kappa}a + \alpha \\ \sqrt{2\gamma_\perp}\sigma \end{bmatrix}, ig_c(\sigma^\dagger a - \sigma a^\dagger) + \right. \\ &\quad \left. \frac{i\sqrt{\kappa}}{2}(\alpha^\dagger a - \alpha a^\dagger) \right), \end{aligned} \quad (7.17)$$

followed by the application of the master equation from section 1.3.

Rather than use the entire physical model for the cQED TLS given by Eq. (7.16) in the network, I implement an adiabatic elimination procedure [BvHS08] (see section

¹The physical system suggested for the X probe should actually include three coupling operators, as the state $|e\rangle$ may spontaneously emit right- or left-handed photons in a given direction. However, the proper inclusion of this additional decay channel leads to an equivalent limiting evolution.

1.6) on Q to obtain the very simple limiting dynamics of a measurable TLS, which will be used in the network model. The physical intuition of the derived dynamics is as follows. As described above and in [KBSM09, KNPM10], in a bad cavity limit ($\kappa \rightarrow \infty$), with the atom in a uncoupled state, a coherent probe resonant with the cavity will enter the cavity and exit ‘immediately’ (due to the large κ), picking up no additional phase shift. However, if the atom is in a coupled state, and the system is also in a ‘small volume’ coupling limit ($g_c, \kappa \rightarrow \infty$ is expected as the device volume vanishes), then the same probe will simply reflect from the off-resonant, atom-*and*-cavity system, picking up an additional π phase shift. Thus, in these limits, the cQED system acts as a simple scattering object with no internal dynamics, but which imparts a phase shift on a cavity-incident coherent probe, as determined by the binary ground state.

Following the mathematical formalism of [BvHS08], I redefine and relabel Q with a scaling parameter k , which is assumed to take the limit $k \rightarrow \infty$, and write the component as a *left* QSDE (essentially the Hermitian conjugate of Q)

$$\begin{aligned} dQ_{l,t}^{(k)} = Q_{l,t}^{(k)} \left\{ -k\sqrt{2\kappa}adB_t^{1\dagger} + k\sqrt{2\kappa}a^\dagger dB_t^1 - \right. \\ \left. \sqrt{2\gamma_\perp}\sigma dB_t^{2\dagger} + \sqrt{2\gamma_\perp}\sigma^\dagger dB_t^2 - k^2\kappa a^\dagger a dt - \gamma_\perp\sigma^\dagger\sigma dt - \right. \\ \left. k^2g_c(\sigma^\dagger a - \sigma a^\dagger)dt \right\}. \end{aligned} \quad (7.18)$$

Note that with the scaling, the cavity field decay and coupling rates take the limits described above (with g_c/κ constant).

In the notation of [BvHS08], the operator coefficients of the above left QSDE are

$$\begin{aligned} K^{(k)} &= -k^2\kappa a^\dagger a - \gamma_\perp\sigma^\dagger\sigma - k^2g_c(a^\dagger\sigma - a\sigma^\dagger), \\ L^{(k)} &= \begin{pmatrix} k\sqrt{2\kappa}a^\dagger \\ \sqrt{2\gamma_\perp}\sigma^\dagger \end{pmatrix}, \quad N^{(k)} = I. \end{aligned} \quad (7.19)$$

Through the adiabatic elimination procedure, a set of limiting operator coefficients (denoted without the ‘ (k) ’) are derived, which define another, limiting propagator, $Q_{l,t}$, to which $Q_{l,t}^{(k)}$ strongly converges (see section 1.6). It is this limiting propagator

that will be used in the eventual network model in place of the physical cQED model.

For the adiabatic elimination we use (see section 1.6)

$$\begin{aligned} Y &= -\kappa a^\dagger a - g_c (a^\dagger \sigma - a \sigma^\dagger), \quad A = 0, \quad B = -\gamma_\perp \sigma^\dagger \sigma, \\ F &= \begin{pmatrix} \sqrt{2\kappa} a^\dagger \\ 0 \end{pmatrix}, \quad G = \begin{pmatrix} 0 \\ \sqrt{2\gamma_\perp} \sigma^\dagger \end{pmatrix}, \quad W = I. \end{aligned} \quad (7.20)$$

In the Z probe case for the bit-flip network, $H_0 = \text{span}\{|g, 0\rangle, |h, 0\rangle\}$ is the domain of the ‘slow’ dynamics the adiabatic elimination procedure isolates and we define

$$\begin{aligned} \tilde{Y} \{|g, 0\rangle, |h, 0\rangle\} &= 0, \\ \tilde{Y} |h, n\rangle &= -\frac{1}{\kappa n} |h, n\rangle, \quad n \geq 1; \\ \tilde{Y} |e, (n-1)\rangle &= -\frac{g_c \sqrt{n}}{\kappa^2 n (n-1) + g_c^2 n} |g, n\rangle - \\ &\quad \frac{\kappa n}{\kappa^2 n (n-1) + g_c^2 n} |e, (n-1)\rangle, \quad n \geq 1; \\ \tilde{Y} |g, n\rangle &= -\frac{\kappa (n-1)}{\kappa^2 n (n-1) + g_c^2 n} |g, n\rangle + \\ &\quad \frac{g_c \sqrt{n}}{\kappa^2 n (n-1) + g_c^2 n} |e, (n-1)\rangle, \quad n \geq 1. \end{aligned} \quad (7.21)$$

which provides $Y\tilde{Y} = \tilde{Y}Y = P_1$, the projector onto the complement of H_0 (see section 1.6). Then by [BvHS08], the limiting operator coefficients are,

$$K = 0, \quad L_1 = L_2 = 0, \quad M_1 = M_2 = 0, \quad (7.22)$$

and (with $\Pi_{in} = |i, n\rangle\langle i, n|$)

$$\begin{aligned}
N_{11} &= P_0 W_{11} \left(F_1^\dagger \tilde{Y} F_1 + \delta_{11} \right) P_0 \\
&= P_0 + 2\kappa P_0 a \tilde{Y} a^\dagger (\Pi_{g0} + \Pi_{h0}) \\
&= P_0 + 2\kappa P_0 a \tilde{Y} (|g1\rangle\langle g0| + |h1\rangle\langle h0|) \\
&= P_0 + 2\kappa P_0 a \left(\frac{1}{g_c} |e0\rangle\langle g0| - \frac{1}{\kappa} |h1\rangle\langle h0| \right) \\
&= P_0 - 2 |h0\rangle\langle h0| \\
&= \Pi_{g0} - \Pi_{h0} \equiv Z, \\
\\
N_{12} &= P_0 W_{11} \left(F_1^\dagger \tilde{Y} F_2 + \delta_{12} \right) P_0 = 0, \\
N_{21} &= P_0 W_{22} \left(F_2^\dagger \tilde{Y} F_1 + \delta_{21} \right) P_0 = 0, \\
\\
N_{22} &= P_0 W_{22} \left(F_2^\dagger \tilde{Y} F_2 + \delta_{22} \right) P_0 = 1, \tag{7.23}
\end{aligned}$$

Collecting the results, the limiting system (as a usual *right-acting* QSDE) is characterized by the operator coefficients

$$Q = \left(\left[\begin{array}{cc} Z & 0 \\ 0 & I \end{array} \right], \left[\begin{array}{c} 0 \\ 0 \end{array} \right], 0 \right), \tag{7.24}$$

to which the physical cQED system, $Q^{(k)}$ from Eq. (7.16), strongly converges in the limit $k \rightarrow \infty$. For the X probe case in the phase-flip network, the analogous follows, but with the Pauli- X spin operator eventually replacing Z in equation (7.24).

7.2.2 Continuous parity measurement in a nanophotonic network

Employing the series concatenation product (section 1.4), we can construct a QSDE representation of a nanophotonic network in which two of these cQED TLSs are placed

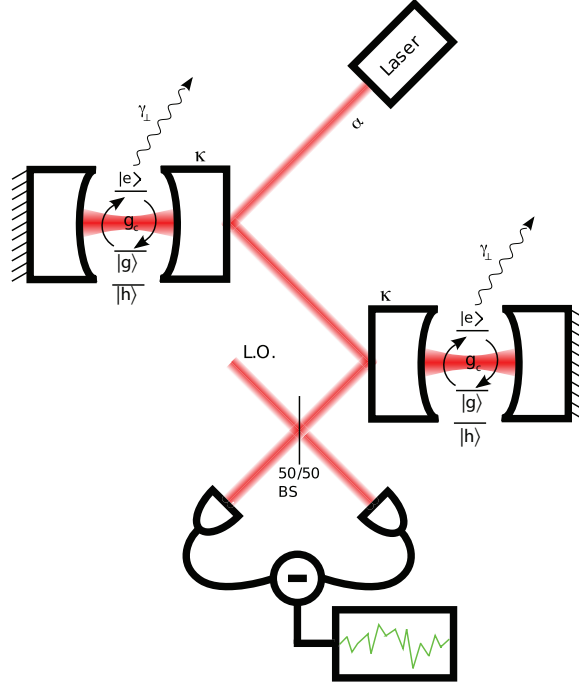


Figure 7.4: (from [KBSM09]) Cartoon of a nanophotonic bit-wise parity measurement network with two Z-probe cQED TLSs.

sequentially along a single mode waveguide, as in Fig. 7.4 [KBSM09]. Simply driving the network with an on-resonant cw laser and performing amplitude-quadrature homodyne measurement of the field that exits the network will effect a continuous, weak parity measurement on the state of the two cQED systems. We can construct a network model utilizing either the complete, physical model of the cQED devices

$$N = (Q_2 \boxplus_2 I) \triangleleft (Q_1 \boxplus I) \triangleleft (W_\alpha \boxplus I_2) \quad (7.25)$$

using the full physical Eq. (7.16) or limiting Eq. (7.24) version of Q (\boxplus_2 is a “padding operator” related to the concatenation product [KNPM10], necessary for proper field indexing) – the mathematical consistency of the series product and similar limiting models was recently shown [GNW10].

Given the QSDE model N , we can derive the conditional evolution of network variables affected by our continuous measurement of the output field (section 2.2.1). A stochastic Schrödinger equation can be used to propagate a conditional quantum

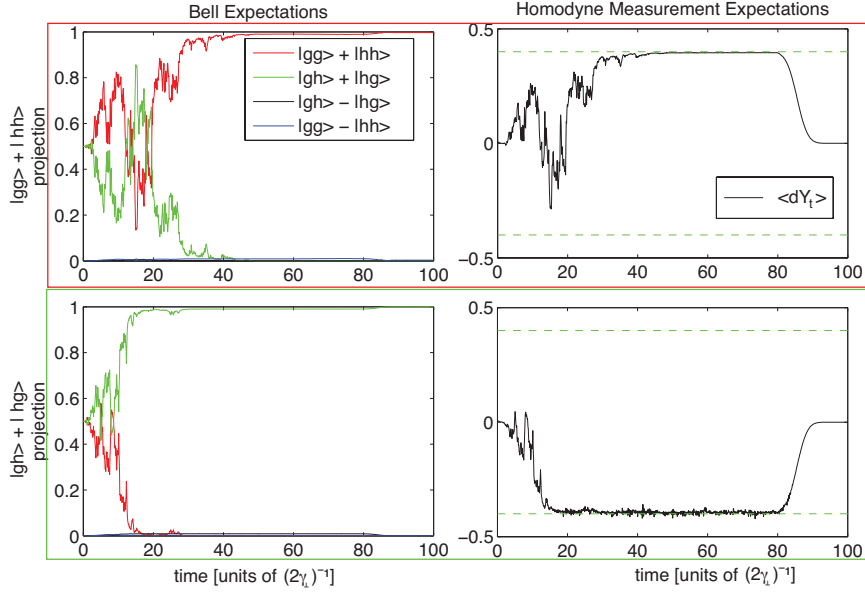


Figure 7.5: (from [KBSM09]) Two independent simulations of atomic Bell-state preparation in a realistic system (see text). The top pair of graphs show a simulation in which the system happened to reduce to even parity; the bottom pair shows an odd-parity example.

state derived from the continuous measurement records $M_t^{(i)}$ (where index (i) specifies the observed output channel). If the conditional state remains pure for all times we may represent it by a vector $|\psi_t\rangle$. As complete purity of the conditional state can only be achieved if all output channels are monitored with perfect efficiency, this is not a realistic assumption in any actual implementation. However the equations so derived are very useful for simulation and analysis; analogous equations for imperfect/incomplete observation with a mixed conditional state (density operator) are easily derived as required for more practical purposes.

If we assume a Z-probe construction for Q and homodyne detection of the amplitude quadrature observable of the field that scatters off of both cavities $Y_t^{(0)} = N_t^\dagger (B_t + B_t^\dagger) N_t = j_t (B_t + B_t^\dagger)$, using N_t , the QSDE integral represented by the full physical version of Eq. (7.25), and separate photon counting of each of the atomic radiation modes $Y_t^{(k)} = j_t (\Lambda_t^{(kk)})$ $k = \{1, 2\}$, the ‘physical’ pure-state propagator derived

from (7.25) is (section 2.2.1)

$$\begin{aligned}
d|\psi_t\rangle = & \left\{ (\sqrt{2\kappa}a_1 + \sqrt{2\kappa}a_2 + \alpha)dY_t^{(0)} + g \sum_{i=1}^2 (\sigma^{(i)\dagger} a_i - \sigma^{(i)} a_i^\dagger) dt \right. \\
& - (a_1^\dagger a_1 + a_2^\dagger a_2) \kappa dt - 2a_2^\dagger a_1 \kappa dt - \alpha \sqrt{2\kappa} (a_1 + a_2)^\dagger dt \\
& \left. + \sum_{i=1}^2 \left((\sqrt{2\gamma_\perp} \sigma^{(i)} - I) dY_t^{(i)} - \gamma_\perp \sigma^{(i)\dagger} \sigma^{(i)} dt \right) \right\} |\psi_t\rangle. \quad (7.26)
\end{aligned}$$

For simulation purposes Eq. (7.26) can be used to generate realistic homodyne measurement records $dY_t^{(0)}$ by driving the innovations and gauge processes with appropriate pseudo-random numbers (section 2.2.1 and [Tan99]). Similarly, if we define $\bar{j}_t(X) = \bar{N}_t^\dagger X \bar{N}_t$ using the QSDE integral \bar{N}_t represented by the limiting version of Eq. (7.25) we can construct the ‘idealized’ pure state propagator assuming homodyne measurement of $\bar{Y}_t = \bar{j}_t(B_t + B_t^\dagger)$ as

$$d|\bar{\psi}_t\rangle = \left\{ \alpha Z_1 Z_2 d\bar{Y}_t - \frac{|\alpha|^2}{2} dt \right\} |\bar{\psi}_t\rangle, \quad |\bar{\psi}_0\rangle \in H_0 \quad (7.27)$$

where $Z_i = |h\rangle\langle h| - |g\rangle\langle g|$ on TLS i (note that for the limiting model for Q Eq. (7.24), we don’t need to monitor the atomic radiation channels to maintain state purity). It is straightforward to show that the idealized filter (7.27) represents a finite-time unraveling of an ideal $Z_1 Z_2$ projective measurement as discussed in [SvHM04]. As a side note, it is interesting to point out that we can alternatively think of (7.27) as a *reduced filter* for analyzing the homodyne photocurrent in a two-cavity setup, which exploits adiabatic elimination for a reduction in the number of system variables. In particular we could track the parity of the two ‘physical’ TLSs (approximately, but with little computational effort) by driving (7.27) with an experimentally measured homodyne photocurrent in place of $d\bar{Y}_t$ (see section 2.2.1). Below we will examine the results of driving (7.27) with simulated ‘experimental’ photocurrents generated by the physical Eq. (7.26).

To demonstrate that the physical model does realize an approximate parity measurement, we can use (7.26) to simulate Bell-state entanglement generation from separable initial states of the atom-cavity systems [NC00], using parameters that should be achievable in a Fabry-Perot cavity/cold Cs atom system with mm-scale dielectric mirrors, $\{g, \kappa, \gamma_{\perp}, \alpha\} = \{20, 4.5, 0.5, 0.2\}$. We numerically integrate (7.26) from the initial state $|\psi_0\rangle = 2^{-1}(|g\rangle + |h\rangle) \otimes |0\rangle^{\otimes 2}$ (that is, both cQED systems separably in a superposition of the ground states and no photons in the cavity). As can be seen in Fig. 7.5, the system begins with equal projections on the $2^{-1/2}(|gg\rangle + |hh\rangle)$ and $2^{-1/2}(|gh\rangle + |hg\rangle)$ joint atomic states and the expected homodyne photocurrent vanishes. The laser is then adiabatically switched on and the conditional state gradually projects into an atomic parity subspace with the corresponding $\langle dY_t^{(0)} \rangle \approx \pm 2\alpha$. After a fixed time $\gamma_{\perp}t = 40$ the probe is adiabatically switched off, but the projected state persists. While the probe is on, the non-zero overlap with atomic Bell states not present in the initial state is caused partially by entanglement with the cavity mode states, but the residual expectation of such Bell states after the laser is switched off is wholly due to the accumulation of weak measurements performed *within* the atomic parity subspaces by the radiation field modes.

Finally, we compare the physical (7.26) and limiting (7.27) by two different computational procedures. First, we compare independent simulations of the idealized projective measurement represented by Eq. (7.27) and the approximate projections represented by Eq. (7.26). To this end, we construct trajectories of the variance of parity operators: $\text{Var}(\sigma_Z^{(1)}\sigma_Z^{(2)})$ from $|\psi_t\rangle$ in simulations of Eq. (7.26) (with $\sigma_Z = |e\rangle\langle e| + |g\rangle\langle g| - |h\rangle\langle h|$ distinguishing cavity-coupled and -uncoupled states), and $\text{Var}(Z_1Z_2)$ from $|\bar{\psi}_t\rangle$ in independent simulations of Eq. (7.27). Some summary statistics from these simulations are depicted in Fig. 7.6. The integrations of the idealized filter are initialized with $|\bar{\psi}_0\rangle = 2^{-1}(|g\rangle + |h\rangle)^{\otimes 2}$. At $t = 0$ we begin with $\text{Var}(\sigma_Z^{(1)}\sigma_Z^{(2)}) = \text{Var}(Z_1Z_2) = 1$, and both variances decrease in time as the systems randomly project into one parity subspace or the other. Indicative of their similar statistics, the $\text{Var}(\sigma_Z^{(1)}\sigma_Z^{(2)})$ and $\text{Var}(Z_1Z_2)$ trajectory ensembles largely overlap at all times. Moreover, it can be shown that the excited state population remains small at all times, $(\frac{\alpha\sqrt{2\kappa}}{g})^2$, and that the atomic dynamics are principally constrained to the

two ground states.

Second, following up on our side note, we assess how well (7.27) performs as a reduced filter for analyzing the physical system. In this case, we construct trajectories of $\text{Var}_{rf}(Z_1 Z_2)$ by integrating $|\bar{\psi}_t\rangle$ with photocurrents simulated from Eq. (7.26). A representative $\text{Var}_{rf}(Z_1 Z_2), \text{Var}(\sigma_Z^{(1)} \sigma_Z^{(2)})$ trajectory pair in Fig. 7.6 suggests the accuracy of the reduced parity estimate. Underlying this are the statistics of the fractional residual error from 1000 such pairs: $|\text{Var}(\sigma_Z^{(1)} \sigma_Z^{(2)}) - \text{Var}_{rf}(Z_1 Z_2)| / \text{Var}(\sigma_Z^{(1)} \sigma_Z^{(2)})$. Although the range of $\text{Var}(\sigma_Z^{(1)} \sigma_Z^{(2)})$ spans 5 orders of magnitude, the reduced filter performs well, tracking this physical parity estimate to within a factor of 2 in every shot.

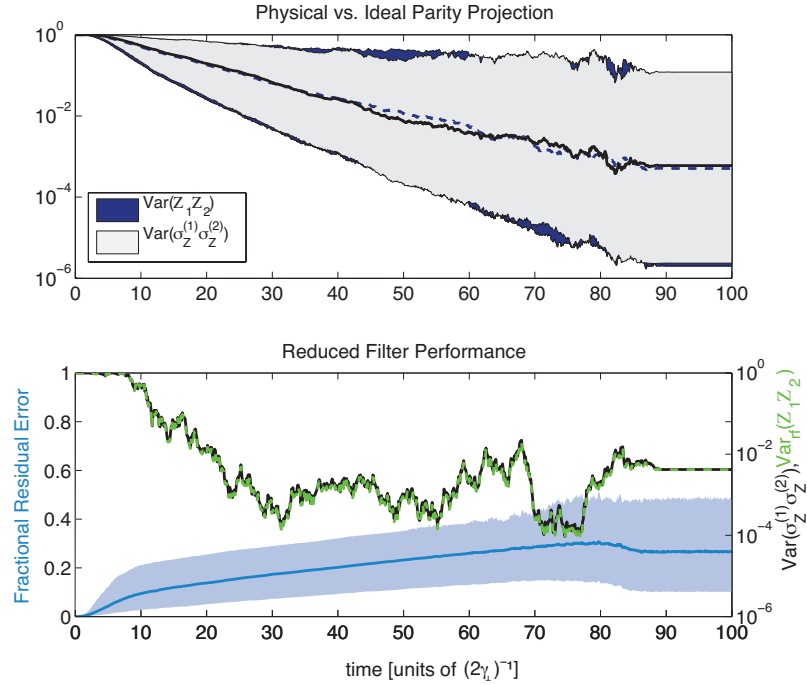


Figure 7.6: (from [KBSM09]) Summary of 1000 Bell-state projection simulations. The top graph compares the statistics of the ideal and physical parity variance. The mean of the $\text{Var}(\sigma_Z^{(1)}\sigma_Z^{(2)})$ trajectories is shown as a solid, black line; grey shading indicates the one-standard deviation range of trajectories above and below the mean. The mean and standard deviation range of $\text{Var}(Z_1Z_2)$ are shown by the dotted line and blue shading. The bottom graph highlights the performance of the reduced filter. Referenced to the right axis, a representative $\text{Var}(\sigma_Z^{(1)}\sigma_Z^{(2)})$, $\text{Var}_{rf}(Z_1Z_2)$ trajectory pair are shown in solid black and dotted green, respectively. The blue-grey line and shading, referenced to the left axis, depicts the mean and standard deviation range of the fractional residual error over all trajectories.

Chapter 8

Autonomous QEC nanophotonic networks

It's well-established that quantum error correction (QEC) is critical to quantum information processing [NC00], but the usual formulation of error correction (e.g. see section 7.1) entails a substantial overhead of classically controlled quantum operations that is cumbersome to accommodate. In this section, I present a novel approach to designing elementary QEC memory cells [KNPM10, KPCM11], in which all control operations are performed autonomously by an embedded optical feedback loop. The approach is natural for nanophotonic or superconducting microwave implementations and in fact is expected to generally approach the ideal operation as the overall volume of the system shrinks. The feedback network is entirely on-chip, requiring no external clocking or control, and during steady-state operation would only need to be powered by the injection of constant-amplitude coherent fields.

While the designs presented here are not yet possible to build, the network is built from passive components such as optical waveguides, beamsplitters and cQED devices, which have all shown rapid improvement in recent solid-state optical research and should eventually be natural to integrate into large scale networks [PLP⁺11, SBF⁺10, KMV⁺10, HKD⁺09, FFE⁺08]. Moreover, the details of the device implementation are of secondary importance. The specific designs were conceived of by considering basic trends in device fabrication and the theoretical models available at

this time. There are many different designs that could achieve these general goals. I feel that the emphasis on designing quantum networks that control themselves and the use of continuous-time physical modeling will be essential in developing actual quantum technologies [JNP08, NJD09, Mab08a, IYY⁺11, Mab11]. With QEC, even in the abstract, this approach is also attractive for design and analysis because it can connect the goal of quantum decoherence suppression with formal optimization methods of classical control theory [ADL02, Mab09b].

While our approach exploits rigorous theoretical results derived using techniques from quantum fields theory and coherent-feedback quantum control (part I), I first give an intuitive presentation of a network that comprises five cavity QED devices and emulates bit- or phase-flip QEC codes, depending on the configuration. That such networks are naturally communicated both intuitively and formally (in the language of QSDEs) suggests their general ability to bridge the gap between abstract quantum information formulations and specific hardware implementations. The final section builds off of the bit-/phase-flip network to propose a more powerful network capable of protecting an encoded qubit from arbitrary single-TLS errors, demonstrating the generalizability of the approach.

8.1 An autonomous bit-/phase-flip network

8.1.1 Intuitive operation

The photonic circuit shown in Fig. 8.1 implements continuous QEC [ADL02, Mab09b, OLB08] based on the bit-flip or phase-flip code (section 7.1.1). Recall that in the bit-flip code a single logical qubit is encoded in the joint state of three physical TLSs and is protected against independent bit-flip errors on any of these register TLSs. The logical state $|\tilde{0}\rangle$ is encoded by the physical state $|000\rangle$ (all three register TLSs jointly in the ‘0’ state), while $|\tilde{1}\rangle$ is encoded by $|111\rangle$. The analogous phase-flip code associates $|\tilde{0}\rangle$ with $|+++ \rangle$ and $|\tilde{1}\rangle$ with $|- - - \rangle$ (where $|\pm\rangle \equiv (|0\rangle \pm |1\rangle)/\sqrt{2}$) and the logical qubit is protected against independent register phase-flip errors. In Fig. 8.1 Q1, Q2 and Q3 represent the register TLSs; the blue signal lines indicate the routing

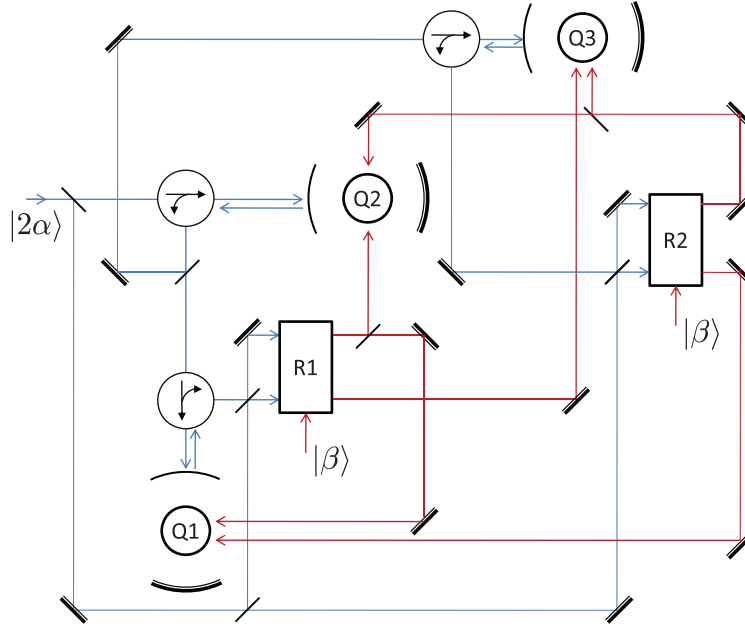


Figure 8.1: (from [KNPM10]) Schematic diagram of an autonomous nanophotonic quantum memory showing TLSs in cavities (Q1, Q2 and Q3), circulators, beamsplitters, steering mirrors and relays.

of a laser beam (injected in the coherent state $|2\alpha\rangle$, where $|\alpha|^2$ has units photons time^{-1}) used for error detection (following principles described in section 7.2.1); $R1$ and $R2$ represent two qubit-based photonic relays (as analyzed in [Mab09a]); and the red signal lines indicate pathways for optical feedback using two additional laser beams (injected in the coherent state $|\beta\rangle$) for corrective Raman bit- or phase-flips. The constant Hamiltonian interactions among the elementary physical systems along the syndrome measurement pathway (blue signal lines) in Fig. 8.1 cause the $|2\alpha\rangle$ field to be scattered into the inputs of the control relays $R1$ and $R2$ in such a way that the relays correctly switch the routing of the optical power in the $|\beta\rangle$ feedback fields (red signal lines) to perform a Raman bit flip or phase flip on any register qubit that needs one. In this scheme α and β take the place of the usual discrete time interval between executions of the circuit that implements syndrome measurement and unitary restoration. Clocked execution of a special measurement/restoration circuit is not required in this approach—with the physical component models described below, the operation of the coherent controller is stationary in the sense that α , β and all

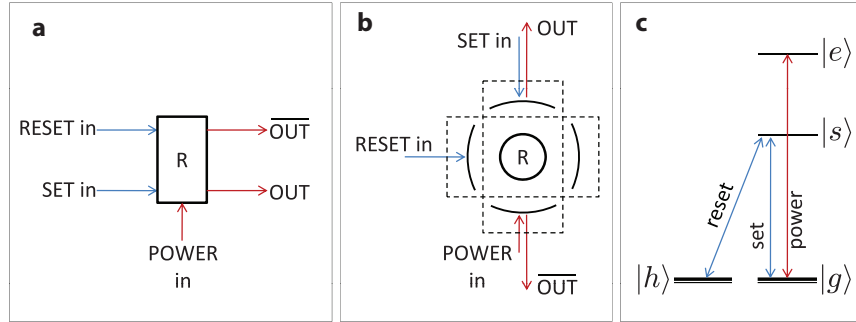


Figure 8.2: Details of the cQED relay component model (modified from [KNPM10, Mab09a]): (a) input and output ports, (b) coupling of input and output fields to resonant modes of the two cavities, and (c) relay internal level diagram.

Hamiltonian coupling strengths are constant in time. Other than the coherent field inputs no interfacing to external detectors or electronics is required. As long as the relays can be implemented in the same hardware platform as the register qubits, the coherent controller can be entirely ‘on-chip.’ Much like an electronic operational amplifier with a feedback impedance network, together the memory and controller devices represent an integrated, self-stabilizing system that simply requires DC power to function.

The quantitative performance of such a quantum memory will of course depend on physical parameters such as the qubit-cavity coupling strengths and the cavity decay rates, but as shown in section 7.2 and [Mab09b] this approach does not require any fine-tuning of the parameters and requires only that certain ratios be large. It is interesting to note that these ratios become large in a *small volume limit* for the optical resonators, which is a natural limit to consider in nanophotonic implementations. Passage to the small volume limit also gives rise to drastic simplifications of the quantum input-output models for the components in the QEC circuit, and thus emerges as a significant new abstraction principle for the analysis of nanophotonic signal-processing networks.

The physical qubits Q1, Q2 and Q3 are assumed to be multilevel ‘atoms’ in resonators whose internal states may be continuously probed, as in section 7.2.1. The central component in the network’s QEC ‘controller’ is a proposed cavity-QED relay [Mab09a], some details of which are presented in Fig. 8.2. Three cavity modes are

resonant with various transitions in an intra-cavity atom, as shown in Fig. 8.2 (b) and (c). In a similar small volume limit [Mab09a], the atomic dynamics are limited to only the ground states, and when the atom is in state $|h\rangle$ ($|g\rangle$) the cavity's POWER input is connected to the OUT ($\overline{\text{OUT}}$) output port. A probe signal driving the SET input port (in the absence of signal at the RESET input) causes the relay state to decay to $|h\rangle$, while driving only the RESET input induces decay to $|g\rangle$. Through these internal dynamics, a probe signal entering either the SET or RESET port of the relay routes the POWER input out either the OUT or $\overline{\text{OUT}}$ port, respectively.

I now trace through the circuit dynamics of Fig. 8.1 in more detail, assuming a bit-flip code implementation. A coherent input $|2\alpha\rangle$ is split into probe and reference beams. The probe beam first reflects from the cavity containing Q2, gaining a π or 0 phase shift depending on the state of that atom, putting the probe signal into a coherent state with amplitude $\sqrt{2}\alpha Z^{(Q2)}$ (where $Z^{(Q2)} = |h\rangle\langle h| - |g\rangle\langle g|$ on Q2 and the identity operation on all other Hilbert spaces is implied). The probe signal is again split and the two resulting fields separately probe the cavities containing Q1 and Q3, resulting in signals with coherent amplitudes $\alpha Z^{(Q1)} Z^{(Q2)}$ and $\alpha Z^{(Q2)} Z^{(Q3)}$. These are interfered with copies of the reference beam, producing four signals with amplitudes $\alpha(I \pm Z^{(Q1)} Z^{(Q2)})/\sqrt{2}$ and $\alpha(I \pm Z^{(Q2)} Z^{(Q3)})/\sqrt{2}$. The '+' signals are sent to the SET inputs of relays R1 and R2, the '-' to the RESET inputs. In this way, the SET (RESET) input to R1 receives a coherent input signal if Q1 and Q2 have even (odd) parity, while the RESET (SET) receives only a vacuum input. Similarly for R2 and qubits Q2 and Q3. The POWER inputs to R1 and R2 are two more coherent fields, each with amplitude β and frequency and polarization that drive the remaining, far-detuned atomic transitions depicted in Fig. 7.3. The $\overline{\text{OUT}}$ port of R1 (R2) is directed to both Q1 and Q2 (Q2 and Q3). The OUT port of R1 (R2) is directed to Q3 (Q1). When a qubit is simultaneously illuminated by two of these feedback beams, Raman resonance conditions are satisfied, inducing a coherent Rabi oscillation between the states of that single qubit. When only one feedback beam illuminates an atom, the beam is assumed to be sufficiently detuned such that it only imparts an AC Stark shift to one of the atomic ground states. Remarkably, a proper choice of the ground state each feedback beam targets prevents Stark shift-induced

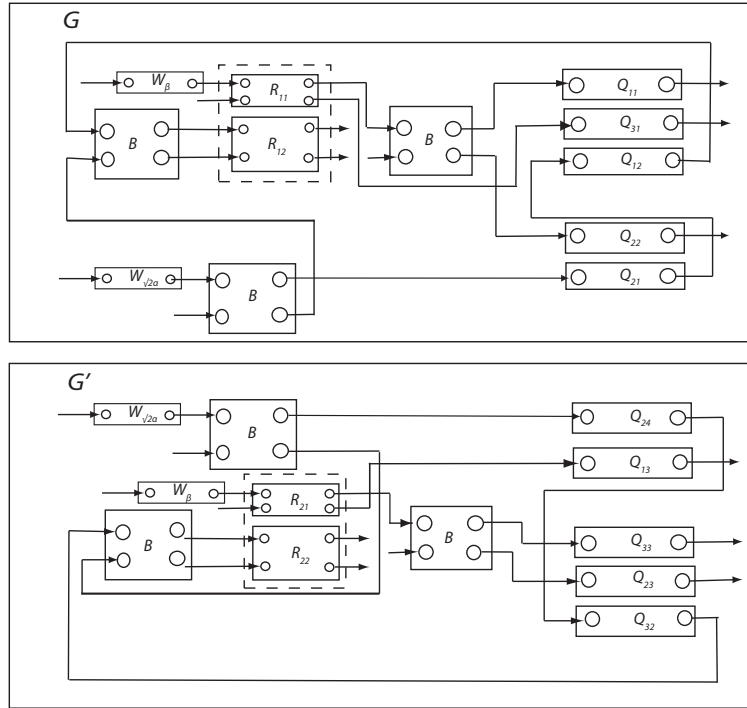


Figure 8.3: (from [KNPM10]) QSDE circuit representation of the autonomous network depicted in Fig. 8.1.

dephasing of the stored codeword *in any error state* [KNPM10].

Assuming the register qubits are initialized in a proper bit-/phase-flip codeword, this network will self-stabilize against bit/phase-flip errors without any external input other than the coherent probe and Raman fields (α , β , and all Hamiltonian coupling constants are constant in time). For an intuitive understanding of the network, note that if no flip errors occur, the SET inputs to the relays are activated, Q1 and Q3 only receive one feedback signal each and no corrective dynamics occur. If for example Q2 flips, the RESET inputs on both R1 and R2 are activated, Q2 receives both feedback signals, while Q1 and Q3 again get only one each. A corrective flipping Hamiltonian is thus implemented on Q2 until a flip is ‘complete,’ which drives the relays back to the ‘no-error’ state, which extinguishes the flipping Hamiltonian.

8.1.2 Network model and dynamics

A more schematic depiction of Fig. 8.1 appropriate for a QSDE representation of the network is shown in Fig. 8.3. Static devices are now shown as labeled blocks, with multiple I/O ports, while the fields connecting them are directional connections between these ports. The QSDE component models are defined in the supplement of [KNPM10], but W_α are coherent inputs (Weyl operators, section 1.4), B are beam-splitters, Q_{ij} are the probe and Raman interaction subsystems of qubits Q_i , and R_{ij} are subsystems of relay R_i .

The network considered in this section, shown schematically in 8.3 is slightly different from the network shown in Fig. 8.1. This is because in this more formal section, the cavity for Q_2 is taken to be two sided with a coherent probe laser impinging on each side, allowing a decomposition of the network into two (symmetric) parts as shown in Fig. 8.3 and simplifying the calculations for the overall network parameters. On the other hand, in Fig. 8.1 all qubit cavities are identical and one sided, which would be probably more suited in actual cQED implementations. Similar effects can be achieved with either a double sided cavity for Q_2 or a single sided cavity that is followed by a 50/50 beamsplitter. Although the two networks are slightly different, they only differ in the overall network scattering matrix, and a slightly modified repeat of the lengthy calculations, with Q_2 one-sided and followed by a beamsplitter, show that the network coupling vector and Hamiltonian will be the same for both networks. As a consequence, I emphasize that *the two networks will have the same network master equation*. Since, the main interest here is the network master equation, to derive this equation it is more convenient to work with the slightly modified network of Fig. 8.3.

The unconditional master equation that describes the dynamics of the autonomous network is immediately constructed after deriving the component model for $G \boxplus G'$,

according to Fig. 8.3. First, following Fig. 8.3, the parts of G are

$$\begin{aligned}
G_p &= R_{12} \triangleleft B \triangleleft ((Q_{12} \triangleleft Q_{21}) \boxplus (I, 0, 0)) \triangleleft \\
&\quad B \triangleleft (W_{\sqrt{2}\alpha} \boxplus (I, 0, 0)), \\
G_f &= (Q_{11} \boxplus Q_{31} \boxplus Q_{22}) \triangleleft (B \boxplus_2 (I, 0, 0)) \triangleleft \\
&\quad (R_{11} \boxplus (I, 0, 0)) \triangleleft (W_\beta \boxplus (I_2, 0, 0)),
\end{aligned} \tag{8.1}$$

representing the ‘probe’ and ‘feedback’ network subsystems of $G = G_p \boxplus G_f$, respectively, and \boxplus_2 is a “padding operator” related to the concatenation product [KNPM10] (necessary for proper field indexing). Correspondences in G' :

$$\begin{aligned}
R_{22} &\leftrightarrow R_{12}, \quad R_{21} \leftrightarrow R_{11}, \quad Q_{23} \leftrightarrow Q_{11}, \quad Q_{33} \leftrightarrow Q_{22}, \\
Q_{13} &\leftrightarrow Q_{31}, \quad Q_{24} \leftrightarrow Q_{21}, \quad Q_{32} \leftrightarrow Q_{12}.
\end{aligned} \tag{8.2}$$

The overall structure of the network is (with a trivial rearrangement of field indices)

$$\begin{aligned}
N &= \left(\text{diag}(S^{(p)}, S'^{(p)}, S^{(f)}, S'^{(f)}), \begin{bmatrix} L^{(p)} \\ L'^{(p)} \\ L^{(f)} \\ L'^{(f)} \end{bmatrix}, \right. \\
&\quad \left. H^{(p)} + H'^{(p)} + H^{(f)} + H'^{(f)} \right).
\end{aligned} \tag{8.3}$$

In this calculation, the network components representing the bit- or phase-flips errors, $E_{X,Z}^{(Q_i)}$, may be simply concatenated to the ‘correction’ network N immediately before the derivation of the full system’s master equation.

A full, physical model for the network then follows from plugging in the physical models for each of the W , B , Q , and R subsystems and applying the series and concatenation products to obtain a single triplet, $N = (S, L, H)$ network model. This symbolic calculation may be done tediously by hand, but may also be automated using symbolic matrix manipulation scripts. As the physical model utilizing both

the Q models derived in 7.2.1 for the probing component of Q1, Q2 and Q3 and the full model for the Raman interactions are too cumbersome to analyze and too large to simulate, we make use of the same adiabatic elimination theorem [BvHS08] to consider instead the limiting dynamics as parameters are appropriately scaled. The small volume limit may be taken before the network construction [GNW10], and so the limiting version of Q model derived in section 7.2.1 (Eq. (7.24)) may be simply plugged into N . The Raman interaction eliminates the excited state r in each qubit (see Fig. 7.3) in the limit of large feedback amplitude and detuning. As the limiting dynamics require input from both G_f and G'_f components, this procedure may only be done after N is at least partly constructed (see the supplemental of [KNPM10]).

After interconnecting simplified (small-volume) models for the bit-flip components according to the bit-flip circuit diagram, including individual bit-flip error processes, and adiabatically eliminating of all but the qubit and relay ground states, one obtains [KNPM10] the closed-loop master equation

$$\dot{\rho}_t = -i[H, \rho_t] + \sum_{j=1}^7 \left(L_j \rho_t L_j^* - \frac{1}{2} \{L_j^* L_j, \rho_t\} \right), \quad (8.4)$$

where

$$\begin{aligned} H &= \Omega \left(\sqrt{2} X^{(Q1)} \Pi_g^{(R1)} \Pi_h^{(R2)} + X^{(Q2)} \Pi_g^{(R1)} \Pi_g^{(R2)} - \sqrt{2} X^{(Q3)} \Pi_h^{(R1)} \Pi_g^{(R2)} - \right. \\ &\quad \left. \Pi_g^{(R1)} (\Pi_g^{(Q1)} + \Pi_h^{(Q2)}) - 2 \Pi_h^{(R1)} \Pi_g^{(Q3)} - \Pi_g^{(R2)} (\Pi_g^{(Q2)} + \Pi_h^{(Q3)}) - 2 \Pi_h^{(R2)} \Pi_h^{(Q1)} \right), \\ L_1 &= \frac{\alpha}{\sqrt{2}} \left(\Pi_g^{(R1)} O^{(12)} + \sigma_{hg}^{(R1)} E^{(12)} \right), \quad L_2 = \frac{\alpha}{\sqrt{2}} \left(-\sigma_{gh}^{(R1)} O^{(12)} - \Pi_h^{(R1)} E^{(12)} \right), \\ L_3 &= \frac{\alpha}{\sqrt{2}} \left(\Pi_g^{(R2)} O^{(32)} + \sigma_{hg}^{(R2)} E^{(32)} \right), \quad L_4 = \frac{\alpha}{\sqrt{2}} \left(-\sigma_{gh}^{(R2)} O^{(32)} - \Pi_h^{(R2)} E^{(32)} \right), \\ L_5 &= \sqrt{\Gamma} X^{(Q1)}, \quad L_6 = \sqrt{\Gamma} X^{(Q2)}, \quad L_7 = \sqrt{\Gamma} X^{(Q3)} \end{aligned} \quad (8.5)$$

where $X^{(C)} = |h\rangle\langle g| + |g\rangle\langle h|$, $\sigma_{jk}^{(C)} = |j\rangle\langle k|$ and $\Pi_j^{(C)} = |j\rangle\langle j|$ on component C , $E^{(ij)} = Z^{(Qi)} Z^{(Qj)} + 1$ and $O^{(ij)} = Z^{(Qi)} Z^{(Qj)} - 1$, each qubit suffers random flips at a rate Γ , and the ‘feedback parameter’ Ω is proportional to $|\beta|^2/\Delta$ (note that several L_j terms corresponding to strong dephasing of the relay states have been omitted

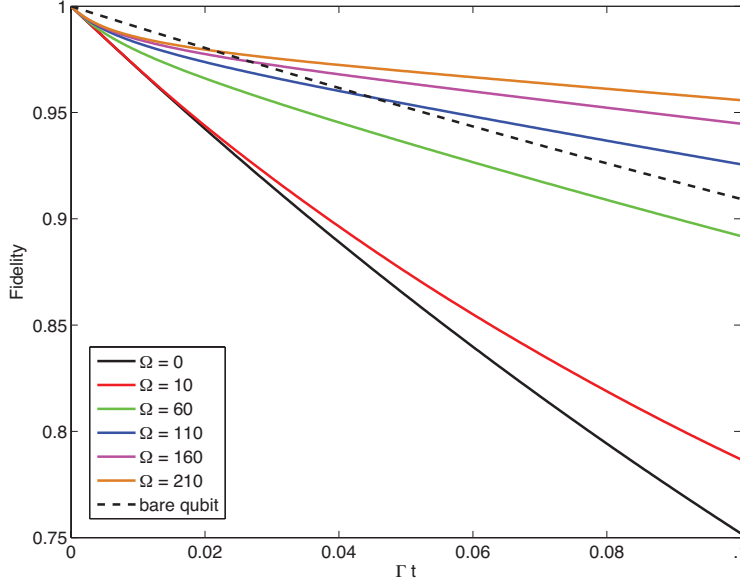


Figure 8.4: (from [KNPM10]) Decay of fidelity, $\langle \Psi_0 | \rho_t | \Psi_0 \rangle$, for several values of the feedback parameter $\Omega = |\beta|^2 \gamma_{\perp} / 2\Delta$ (see the supplemental of [KNPM10]), $\alpha = \Omega/8$, and $\Gamma = 0.1$. The fidelity decay of a single, bare qubit also suffering bitflip errors at rate $\Gamma = .1$ is also shown.

as they have no appreciable effect on the dynamics). An analogous procedure using the phase-flip component models leads to a master equation with the substitutions $Z^{(Q_i)} \leftrightarrow X^{(Q_i)}$, $2\Pi_h^{(Q_i)} \rightarrow 1 \pm X^{(Q_i)}$. While L_5 through L_7 drive the corrupting bit-flip processes, the first three terms of the Hamiltonian (H) and remaining ‘collapse operators’ work in concert to implement the corrections: L_1 through L_4 chiefly drive the states of the two relays to reflect the qubit parities, and each bit-flipping term in the Hamiltonian is only active for a particular ‘syndrome state’ [Got09], as indicated by the relays. The remaining Hamiltonian terms physically correspond to AC Stark shifts, whose effects have been minimized by design [KNPM10].

In Fig. 8.4 we display some illustrative numerical integrations [Tan99] of Eq. (8.4) for the bit-flip scenario. With the flip rate set to $\Gamma = 0.1$, the feedback amplitude is varied from $\Omega = 0$ (no feedback) to $\Omega = 210$, with the probe amplitude kept at $\alpha = \Omega/8$. The initial state of the qubit register is chosen as $|\Psi_0\rangle = (|ggg\rangle - i|hhh\rangle)/\sqrt{2}$,

$\rho_0 = |\Psi_0\rangle\langle\Psi_0|$, and the fidelity decay $\langle\Psi_0|\rho_t|\Psi_0\rangle$ is computed to quantify the decoherence suppression achieved by the coherent feedback loop. With $\Omega = 0$ the fidelity decay is identical to that of the three-qubit register without any measurement or feedback, while for larger values of Ω and longer storage times, the fidelity of the encoded qubit is clearly improved relative to what it would be for a bare qubit. Variable performance with $|\Psi_0\rangle$ simply reflects the different susceptibilities of codewords to bit-flip errors. Because of the small probability that additional errors accrue before the correction of a single flip, fidelity is gradually lost for finite probe/feedback strengths, as in conventional QEC with finite correction time intervals.

8.2 The autonomous subsystem QEC network

While the network described in the previous section is able to emulate the bit- or phase-flip QEC codes, such codes are severely limited: they can only protect the encoded logical qubit against either single-qubit bit-flip or single-qubit phase-flip errors. To emphasize how straightforwardly the approach scales to more powerful QEC codes, in this final section I describe, model and simulate an autonomous nanophotonic network that emulates the 9 qubit Bacon-Shor subsystem code [Bac06, AC07], the smallest of a class of naturally fault-tolerant QEC codes capable of protecting a single logical qubit from arbitrary single-qubit errors (see 7.1.2 for a description of this code).

Using the same components and the intuition gained in section 8.1, it's in fact immediately clear how one could design a self-correcting nanophotonic network that emulates the 9 qubit Bacon-Shor QEC code [Bac06]. In addition, one may also immediately write down the full master equation that governs the internal dynamics of all memory and controller devices of this network without having to resort to a quantum circuit model, suggesting the general applicability of the approach (a laborious, but straightforward network calculation confirms the master equation; see below). In figure 8.5 we sketch the nanophotonic design. Two probe laser inputs first travel down the middle row and column of a 3×3 grid of memory qubits. At the end of the middle row or column, both probes are split on a beamsplitter with each

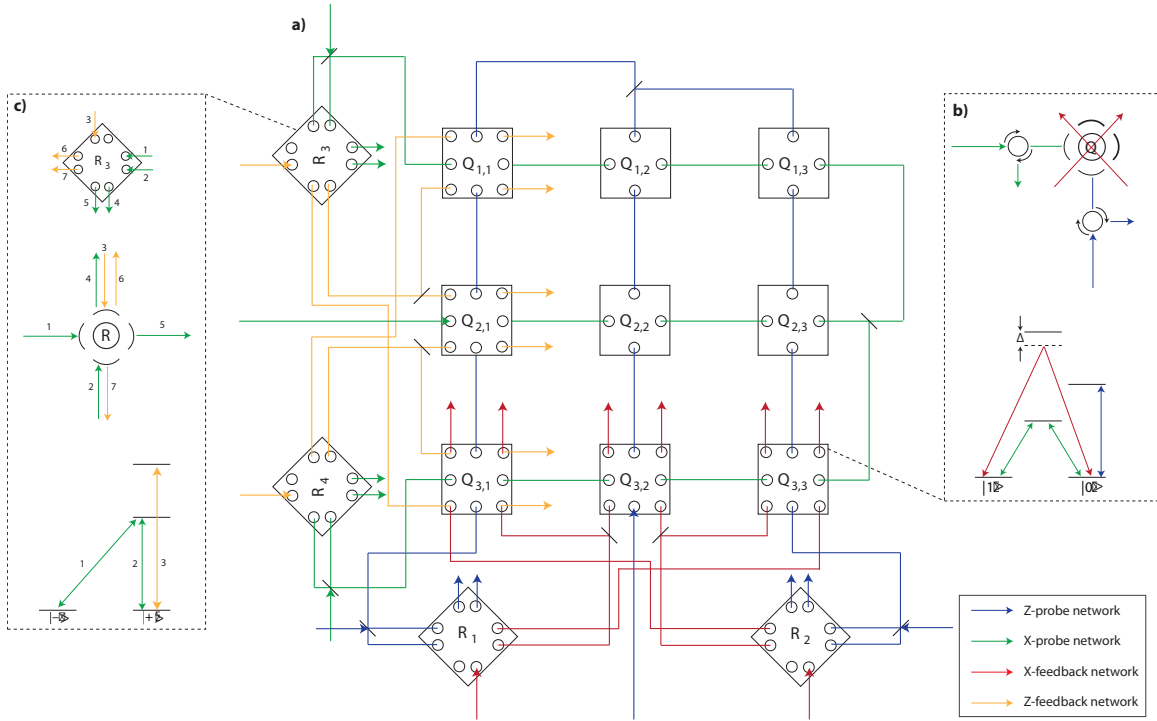


Figure 8.5: (from [KPCM11]) **a)** Schematic of nanophotonic network capable of implementing the 9 qubit Bacon-Shor QEC code. CW coherent field inputs that probe the “Z” and “X” syndromes of the memory qubits, $Q_{i,j}$, enter from the middle of the bottom and left-hand side, in blue and green, respectively. After traversing the memory qubits, the phases of these fields represent measurements of the four syndrome generators. Through interference with four more cw “local oscillator” laser inputs on beamsplitters and interaction with four “relay controller” qubits, R_i , these phases effectively control the relays’ internal states. The relay internal states then direct four “feedback” cw inputs towards the memory qubits. When two red (orange) feedback beams simultaneously illuminate a memory qubit, coherent Pauli-X (-Z) rotations occur until a “no-error” syndrome state is recovered, at which point the corrective feedback dynamics automatically shut off. **b)** & **c)** Example memory and relay cQED input-output, internal level structure, and coupled atomic transition schematics, adapted from [KNPM10].

of the now four probe beams traveling back along the remaining rows and columns, respectively. The frequency and polarization of the laser probe traversing the rows (columns) is such that upon reflection from each memory cQED device, the probe picks up either a π or 0 phase shift according to the atomic ground state in a Pauli-X

(Pauli-Z) basis. Thus after traversing the memory qubits, the phases of the four probe lasers become entangled with the memory qubits via controlled-NOT interactions (in a qubit Z- or X-basis) – essentially as four ancilla qubits would be to extract the error syndrome in a measurement-based QEC scheme [Got09, NC00, AC07]. By interfering with four local oscillator lasers, the phases of the four probes set the internal state of four relays, which thus play the role of the classical register in a measurement-based scheme; the four relay states together represent the quantum memory’s error syndrome [Got09, NC00]. As in [KNPM10], these relays control the routing of four more input “feedback” lasers that perform corrective, unitary rotations on the ground state of the memory qubits via Raman interactions: when a single qubit is simultaneously illuminated by feedback beams emitted by both “Z-syndrome” (“X-syndrome”) relays, it undergoes coherent Pauli-X (Pauli-Z) rotations between its ground states (for simplicity in this much larger network, we assume Stark-shift compensation mechanisms are in place [KNPM10]) until the memory qubits – followed by the controllers – recover their “no-error” state, and automatically shut off the corrective feedback. Although errors may occur to any of memory qubits, corrective feedback is applied to only a small subset of the memory qubits, as in figure 8.5, due to the subsystem structure of the code [KLP05, Bac06] (see 7.1.2). Moreover, as the internal states of the relays are continually reinforced by the cw probes, errors in the relays’ atomic states should be self-corrected by the network.

The subsystem structure of the Bacon-Shor code [KLP05, Bac06] may be further leveraged in a slightly modified network configuration. Although doing so would require a significantly more intricate waveguide network and/or cQED devices, instead of threading the probe fields directly along rows and columns, a zig-zag configuration, as in figure 8.6, should aid network robustness against optical waveguide loss. Whereas photon loss almost anywhere in error-probe waveguide depicted in figure 8.5 effectively causes network-induced “errors” (which sometimes can be ameliorated by the correction network), logical fidelity in the “zig-zag” network should be immune to any waveguide loss in half of the probe network connections [AC07] (see 7.1.2). We will consider these losses and other critical robustness concerns in depth a later publication, however, and so for my purposes here, both networks represented in figures

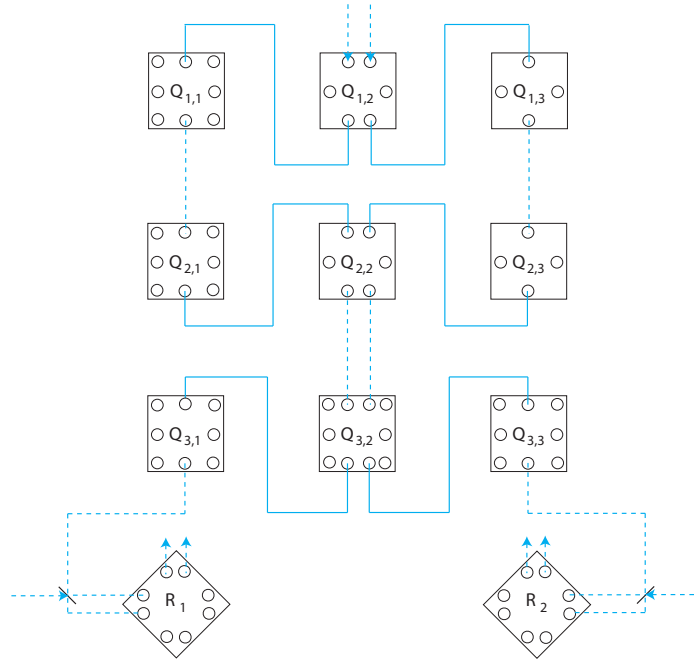


Figure 8.6: (from [KPCM11]) Schematic of the “zig-zag” configuration of the Z-probe network only. Due to the subsystem structure of the code, dotted connections are capable of suffering calibrated waveguide loss without disruption to the logical information stored in the memory qubits (section 7.1.2). The “zig-zag” configuration for the X-probe network follows analogously, essentially rotated by 90° .

8.5 and 8.6 have equivalent dynamics.

The quantum circuit model approach to deriving the master equation dynamics of the network depicted in figure 8.5 proceeds by appropriately “connecting” individual quantum optical device models in series (section 1.4) and parallel (section 1.5) along freely-propagating optical field modes. In an equivalent procedure as in section 8.1, the entire closed loop QSDE model for our 9 qubit Bacon-Shor network may be

constructed from

$$\begin{aligned}
G_p^Z &= (R_1^c \boxplus R_2^c) \triangleleft (B \boxplus B) \triangleleft \\
&\quad \left((Q_{3,1}^Z \triangleleft Q_{2,1}^Z \triangleleft Q_{1,1}^Z) \boxplus I_1 \boxplus (Q_{3,3}^Z \triangleleft Q_{2,3}^Z \triangleleft Q_{1,3}^Z) \right) \triangleleft \\
&\quad \left((B \boxplus_2 I_1) \boxplus I_1 \right) \triangleleft \left((Q_{1,2}^Z \triangleleft Q_{2,2}^Z \triangleleft Q_{3,2}^Z \triangleleft W^{\sqrt{2}\alpha}) \boxplus W^\alpha \boxplus I_1 \boxplus W^\alpha \right) \\
G_{f1} &= (Q_{3,3}^{X1} \boxplus Q_{3,1}^{X1} \boxplus Q_{3,2}^{X1}) \triangleleft (I_1 \boxplus B) \triangleleft \left((R_1^f \triangleleft (W^\beta \boxplus I_1)) \boxplus I_1 \right) \\
G_{f2} &= (Q_{3,1}^{X1} \boxplus Q_{3,3}^{X1} \boxplus Q_{3,2}^{X1}) \triangleleft (I_1 \boxplus B) \triangleleft \left((R_2^f \triangleleft (W^\beta \boxplus I_1)) \boxplus I_1 \right) \\
G_p^X &= (R_3^c \boxplus R_4^c) \triangleleft (B \boxplus B) \\
&\quad \triangleleft \left((Q_{1,1}^X \triangleleft Q_{1,2}^X \triangleleft Q_{1,3}^X) \boxplus I_1 \boxplus (Q_{3,1}^X \triangleleft Q_{3,2}^X \triangleleft Q_{3,3}^X) \right) \triangleleft \\
&\quad \left((B \boxplus_2 I_1) \boxplus I_1 \right) \triangleleft \left((Q_{2,3}^X \triangleleft Q_{2,2}^X \triangleleft Q_{2,1}^X \triangleleft W^{\sqrt{2}\alpha}) \boxplus W^\alpha \boxplus I_1 \boxplus W^\alpha \right) \\
G_{f3} &= (Q_{3,1}^{Z1} \boxplus Q_{1,1}^{Z1} \boxplus Q_{2,1}^{Z1}) \triangleleft (I_1 \boxplus B) \triangleleft \left((R_3^f \triangleleft (W^\beta \boxplus I_1)) \boxplus I_1 \right) \\
G_{f4} &= (Q_{1,1}^{Z1} \boxplus Q_{3,1}^{Z1} \boxplus Q_{2,1}^{Z1}) \triangleleft (I_1 \boxplus B) \triangleleft \left((R_4^f \triangleleft (W^\beta \boxplus I_1)) \boxplus I_1 \right) \\
G_{network} &= G_p^Z \boxplus G_{f1} \boxplus G_{f2} \boxplus G_p^X \boxplus G_{f3} \boxplus G_{f4} \tag{8.6}
\end{aligned}$$

where G_p^Z (G_p^X) describes the “Z” (“X”) syndrome extraction network, G_{fi} describes the feedback network controlled by relay i , and $G_{network}$ represents the (S, L, H) triple of the entire system, describing all but the error dynamics. As in the previous section, the final step in the calculation, which yields a relatively low-dimensional total network $G_{network}$, is the application of an algorithmic adiabatic elimination procedure [BvHS08] that restricts the Raman interaction dynamics to the ground states of the memory qubits only.

Including arbitrary single-qubit dephasing of each memory qubit to $G_{network}$ through simple concatenation products, the closed loop dynamics of ρ_t , the density matrix for all 9 memory and 4 relays qubits (physically representing the entire system’s dynamics after tracing over the field degrees of freedom), is read off from the entire system’s

(S, L, H) triple [KNPM10, Car93a], giving:

$$\begin{aligned}
\dot{\rho}_t &= -i[H, \rho_t] + \sum_{j=1}^{35} \left(L_j \rho_t L_j^* - \frac{1}{2} \{L_j^* L_j, \rho_t\} \right), \quad \text{with} \\
H &= \Omega \left(\sqrt{2} X_{3,1} \Pi_1^- \Pi_2^+ + X_{3,2} \Pi_1^- \Pi_2^- - \sqrt{2} X_{3,3} \Pi_1^+ \Pi_2^- + \right. \\
&\quad \left. \sqrt{2} Z_{1,1} \Pi_3^- \Pi_4^+ + Z_{2,1} \Pi_3^- \Pi_4^- - \sqrt{2} Z_{3,1} \Pi_3^+ \Pi_4^- \right), \\
L_1 &= \frac{\alpha}{\sqrt{2}} (\Pi_1^- O_{1&2}^Z + \sigma_1^{+-} E_{1&2}^Z), \quad L_2 = \frac{\alpha}{\sqrt{2}} (-\sigma_1^{-+} O_{1&2}^Z - \Pi_1^+ E_{1&2}^Z), \\
L_3 &= \frac{\alpha}{\sqrt{2}} (\Pi_2^- O_{3&2}^Z + \sigma_2^{+-} E_{3&2}^Z), \quad L_4 = \frac{\alpha}{\sqrt{2}} (-\sigma_2^{-+} O_{3&2}^Z - \Pi_2^+ E_{3&2}^Z), \\
L_5 &= \frac{\alpha}{\sqrt{2}} (\Pi_3^- O_{1&2}^X + \sigma_3^{+-} E_{1&2}^X), \quad L_6 = \frac{\alpha}{\sqrt{2}} (-\sigma_3^{-+} O_{1&2}^X - \Pi_3^+ E_{1&2}^X), \\
L_7 &= \frac{\alpha}{\sqrt{2}} (\Pi_4^- O_{3&2}^X + \sigma_4^{+-} E_{3&2}^X), \quad L_8 = \frac{\alpha}{\sqrt{2}} (-\sigma_4^{-+} O_{3&2}^X - \Pi_4^+ E_{3&2}^X), \\
L_{9-17} &= \sqrt{\Gamma} X_{i,j}, \quad L_{18-26} = \sqrt{\Gamma} Z_{i,j}, \quad L_{26-35} = \sqrt{\Gamma} Y_{i,j} \quad i, j \in \mathbb{Z}_3, \quad (8.7)
\end{aligned}$$

where $\{X_{i,j}, Z_{i,j}\}$ are the Pauli- $\{X, Z\}$ operators on the memory qubit in row i and column j , Π_i^\pm is the projector onto state $|\pm\rangle$ of relay i , $\sigma_i^{\pm\mp} = |\pm\rangle\langle\mp|$ for relay i , and $\{-O_{i&j}^Z, E_{i&j}^Z, -O_{i&j}^X, O_{i&j}^X, \} = 1 + \{-Z_{*,i} Z_{*,j}, Z_{*,i} Z_{*,j}, -X_{i,*} X_{j,*}, X_{i,*} X_{j,*}\}$ with index $*$ signifying the operator product of all operators acting on some row or column. Γ is the mean error rate of each type of single-qubit error, α is the coherent amplitude of the (eventual) four probe lasers (where $|\alpha|^2$ has units photons time^{-1}), and Ω is proportional to the optical power in each feedback beam. Comparison with the master equation derived in the previous section Eq. (8.4), reveals that these dynamics for the 9 qubit QEC subsystem code appear as an almost trivial expansion of that simple bit-/phase-flip network.

Despite the idealized description of all cQED systems as simple qubits, Eq. (8.7) still represents complex dynamics on a (sparse) density matrix with dimensions $2^{9+4} \times 2^{9+4}$. Due to the size of the problem, multi-threaded numerical integration of Eq. (8.7) was carried out on a multicore computational server using BLAS routines with OpenMP. Figure 8.7 depicts the time-evolution of the fidelity of the logical information stored in the system, initialized with the logical qubit in the $+1 Y_L$ eigenstate, the

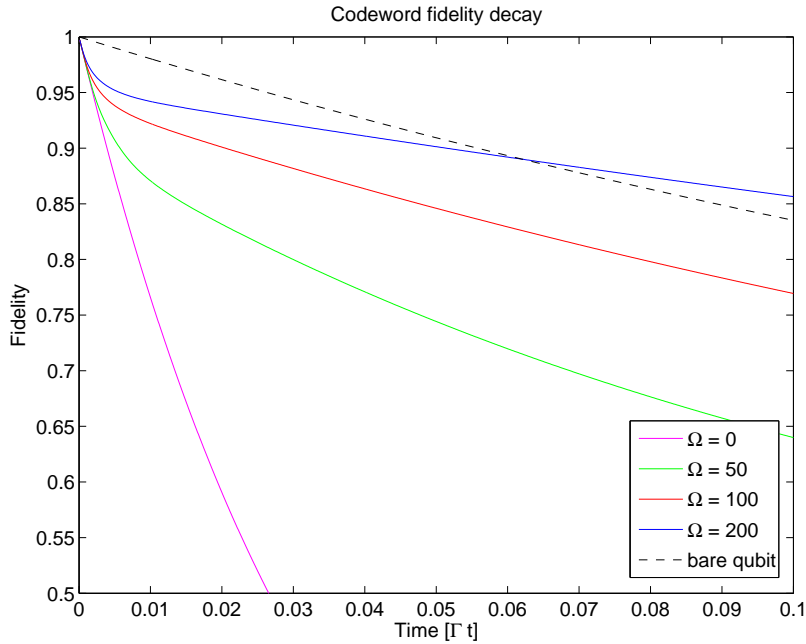


Figure 8.7: (from [KPCM11]) Decay of the logical codeword fidelity (see 7.1.2) in time for several feedback parameters. In the simulation, single-memory qubit X-, Y- and Z-errors occur each at average rate $\Gamma = .1$ per qubit. While the amplitude of the probes, are fixed at $\alpha = \Omega/8$, the feedback “strength” Ω is varied from 0 (no feedback) to 200. For large feedback strengths, the logical storage fidelity is eventually superior to that of a single, bare qubit suffering arbitrary dephasing.

four gauge qubits in $+1 Z_{T_i}$ eigenstates (see 7.1.2), and the four relays each in their “no error” $|+\rangle$ state. The bitwise-error rate was fixed at $\Gamma = .1$, the probe strength kept at $\alpha = \Omega/8$, and the “feedback strength” Ω varied from 0 to 200. Initially, all fidelity curves drop steeply, representing a network “latency” before both probe and feedback networks begin to correct errors. Thereafter, fidelity still drops due to the finite probability that multiple errors irrecoverably accumulate before correction, but at a retarded rate that decreases with increasing feedback strength. For $\Omega > 100$, despite the initially steep fidelity loss, the decay is slow enough to eventually achieve superior storage fidelity than a single, uncorrectable qubit suffering X-, Y-, and Z-errors at the same bit-wise rate.

Finally, we may break down the dynamics of this particular network by calculating

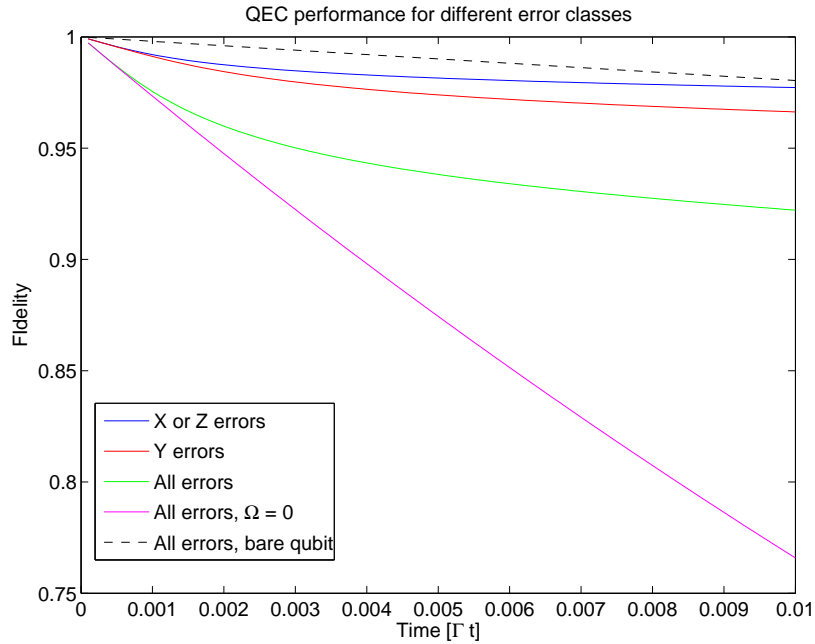


Figure 8.8: (from [KPCM11]) Comparison of network storage fidelity between systems suffering different types of errors. All solid curves are simulated with $\{\Gamma, \alpha, \Omega\} = \{.1, 100/8, 100\}$, except for the magenta curve, which has no feedback, as indicated. The blue curve represents the storage fidelity when only X- or only Z-errors occur to each memory qubit. The only slightly lower red curve comes from a system suffering only Y-errors, which require coordination between all aspects of the network. The green curve represents a system suffering all three types of error, each at the same bit-wise rate, and has roughly the same fidelity decay as a sum of the decays from each type of error acting alone. The dashed black line again represents the logical fidelity of a single, bare qubit suffering all three types of errors at mean rate $\Gamma = .1$ each.

its performance in response to different types of errors. In figure 8.8, we plot the fidelity decay in time with $\{\Gamma, \alpha, \Omega\} = \{.1, 100/8, 100\}$, but with the memory qubits suffering only single-qubit X-, Z-, or Y-errors. Systems suffering only X- or Z-errors require only “half” of the feedback network to function well and achieve the best storage fidelity. The system responds slightly worse to Y-errors. This is expected as Y-flip errors (i.e. simultaneous bit-flip *and* phase-flip errors on a single qubit) requires the two halves of the correction network to work in concert to correct the error. That

such coordination occurs without too much additional fidelity loss suggests that the apparatus is fairly unbiased towards the types of errors it corrects. Similarly, when all three errors are acting simultaneously, each at mean rate $\Gamma = .1$ per qubit, the additional fidelity loss scales roughly linearly with the *total* error rate in this strong feedback regime, as one would expect for an efficiently operating system.

Bibliography

- [AC91] P Alsing and H J Carmichael. Spontaneous dressed-state polarization of a coupled atom and cavity mode. *Quantum Optics: Journal of the European Optical Society Part B*, 3(1):13, 1991. Available from: <http://stacks.iop.org/0954-8998/3/i=1/a=003>. 52, 55, 58, 60, 91
- [AC07] Panos Aliferis and Andrew W. Cross. Subsystem fault tolerance with the bacon-shor code. *Phys. Rev. Lett.*, 98(22):220502, May 2007. doi:10.1103/PhysRevLett.98.220502. 109, 132, 134
- [ADL02] Charlene Ahn, Andrew C. Doherty, and Andrew J. Landahl. Continuous quantum error correction via quantum feedback control. *Phys. Rev. A*, 65(4):042301, Mar 2002. doi:10.1103/PhysRevA.65.042301. 123
- [AM06] M. A. Armen and H. Mabuchi. Low-lying bifurcations in cavity quantum electrodynamics. *Phys. Rev. A*, 73(6):063801, Jun 2006. doi:10.1103/PhysRevA.73.063801. 37, 39, 44, 45, 46, 48, 49
- [AMM09] Michael A. Armen, Anthony E. Miller, and Hideo Mabuchi. Spontaneous dressed-state polarization in the strong driving regime of cavity qed. *Phys. Rev. Lett.*, 103(17):173601, Oct 2009. doi:10.1103/PhysRevLett.103.173601. 52, 55, 75, 76, 91, 95
- [Arm09] M. A. Armen. *Bifurcations in single-atom cavity QED*. PhD thesis, California Institute of Technology, 2009. 40, 41, 52, 55, 57, 58, 70, 73, 74, 75, 76, 91, 95

- [ASO⁺08] Peter A. Andrekson, Henrik Sunnerud, Shoichiro Oda, Takashi Nishitani, and Jiang Yang. Ultrafast, atto-joule switch using fiber-opticparametric amplifier operated in saturation. *Opt. Express*, 16(15):10956–10961, Jul 2008. Available from: <http://www.opticsexpress.org/abstract.cfm?URI=oe-16-15-10956>, doi:10.1364/OE.16.010956. 47, 69
- [Bac06] Dave Bacon. Operator quantum error-correcting subsystems for self-correcting quantum memories. *Phys. Rev. A*, 73(1):012340, Jan 2006. doi:10.1103/PhysRevA.73.012340. 107, 132, 134
- [Bar90] A Barchielli. Direct and heterodyne detection and other applications of quantum stochastic calculus to quantum optics. *Quantum Optics: Journal of the European Optical Society Part B*, 2(6):423, 1990. Available from: <http://stacks.iop.org/0954-8998/2/i=6/a=002>. 4, 6, 10, 14, 23, 24, 26, 28
- [BFSB09] Paul E. Barclay, Kai-Mei Fu, Charles Santori, and Raymond G. Beausoleil. Hybrid photonic crystal cavity and waveguide for coupling to diamond nv-centers. *Opt. Express*, 17(12):9588–9601, Jun 2009. Available from: <http://www.opticsexpress.org/abstract.cfm?URI=oe-17-12-9588>, doi:10.1364/OE.17.009588. 38
- [BMB⁺04] A. Boca, R. Miller, K. M. Birnbaum, A. D. Boozer, J. McKeever, and H. J. Kimble. Observation of the vacuum rabi spectrum for one trapped atom. *Phys. Rev. Lett.*, 93(23):233603, Dec 2004. doi:10.1103/PhysRevLett.93.233603. 36, 73
- [BvHJ07] Luc Bouten, Ramon van Handel, and Matthew R. James. An introduction to quantum filtering. *SIAM Journal on Control and Optimization*, 46(6):2199–2241, 2007. Available from: <http://link.aip.org/link/?SJC/46/2199/1>, doi:10.1137/060651239. 4, 6, 10, 13, 14, 15, 23, 24, 26, 31, 32, 33, 34

- [BvHS08] Luc Bouten, Ramon van Handel, and Andrew Silberfarb. Approximation and limit theorems for quantum stochastic models with unbounded coefficients. *Journal of Functional Analysis*, 254(12):3123 – 3147, 2008. Available from: <http://www.sciencedirect.com/science/article/B6WJJ-4S69SFK-1/2/1f6713358ce099d9ea560a15cbdf84eb>, doi:DOI:10.1016/j.jfa.2008.02.013. 4, 6, 20, 21, 112, 113, 114, 130, 136
- [Car93a] H. Carmichael. *An Open Systems Approach to Quantum Optics*. Springer Berlin / Heidelberg, 1993. 16, 23, 24, 31, 33, 36, 37, 39, 40, 42, 73, 137
- [Car93b] H. J. Carmichael. *Frontiers in Optics*. Springer-Verlag, Berlin, 1993. 44
- [CLS⁺04] J. Chiaverini, D. Leibfried, T. Schaetz, M. D. Barrett, R. B. Blakestad, J. Britton, W. M. Itano, J. D. Jost, E. Knill, C. Langer, R. Ozeri, and D. J. Wineland. Realization of quantum error correction. *Nature*, 432(7017):602–605, 12 2004. Available from: <http://dx.doi.org/10.1038/nature03074>. 99
- [CMR05] O. Cappé, E. Moulines, and T. Rydén. *Inference in Hidden Markov Models*. Springer, 2005. 92
- [CTDRG89] C. Cohen-Tannoudji, J. Dupont-Roc, and G. Grynberg. *Photons & Atoms: Introduction to Quantum Electrodynamics*. John Wiley & Sons, Inc., 1989. 38, 40
- [CTDRG92] C. Cohen-Tannoudji, J. Dupont-Roc, and G. Grynberg. *Atom-Photon Interactions: Basic Processes and Applications*. John Wiley & Sons, Inc., 1992. 38, 39
- [DCG⁺09] L. DiCarlo, J. M. Chow, J. M. Gambetta, Lev S. Bishop, B. R. Johnson, D. I. Schuster, J. Majer, A. Blais, L. Frunzio, S. M. Girvin, and

- R. J. Schoelkopf. Demonstration of two-qubit algorithms with a superconducting quantum processor. *Nature*, 460(7252):240–244, 07 2009. Available from: <http://dx.doi.org/10.1038/nature08121>. 99
- [DHK⁺83] R. W. P. Drever, J. L. Hall, F. V. Kowalski, J. Hough, G. M. Ford, A. J. Munley, and H. Ward. Laser phase and frequency stabilization using an optical resonator. *Applied Physics B: Lasers and Optics*, 31:97–105, 1983. 10.1007/BF00702605. Available from: <http://dx.doi.org/10.1007/BF00702605>. 76
- [DK04] L.-M. Duan and H. J. Kimble. Scalable photonic quantum computation through cavity-assisted interactions. *Phys. Rev. Lett.*, 92(12):127902, Mar 2004. [doi:10.1103/PhysRevLett.92.127902](https://doi.org/10.1103/PhysRevLett.92.127902). 110
- [DRS⁺10] L. DiCarlo, M. D. Reed, L. Sun, B. R. Johnson, J. M. Chow, J. M. Gambetta, L. Frunzio, S. M. Girvin, M. H. Devoret, and R. J. Schoelkopf. Preparation and measurement of three-qubit entanglement in a superconducting circuit. *Nature*, 467(7315):574–578, 09 2010. Available from: <http://dx.doi.org/10.1038/nature09416>. 99
- [EFF⁺07] Dirk Englund, Andrei Faraon, Ilya Fushman, Nick Stoltz, Pierre Petroff, and Jelena Vuckovic. Controlling cavity reflectivity with a single quantum dot. *Nature*, 450(7171):857–861, 12 2007. Available from: <http://dx.doi.org/10.1038/nature06234>. 55
- [EFZ⁺07] Dirk Englund, Andrei Faraon, Bingyang Zhang, Yoshihisa Yamamoto, and Jelena Vučković. Generation and transfer of single photons on a photonic crystal chip. *Opt. Express*, 15(9):5550–5558, Apr 2007. Available from: <http://www.opticsexpress.org/abstract.cfm?URI=oe-15-9-5550>, [doi:10.1364/OE.15.005550](https://doi.org/10.1364/OE.15.005550). 36, 38
- [Fag90] Franco Fagnola. On quantum stochastic differential equations with unbounded coefficients. *Probability Theory and Related Fields*, 86:501–516,

1990. 10.1007/BF01198172. Available from: <http://dx.doi.org/10.1007/BF01198172>. 4
- [FFE⁺08] Andrei Faraon, Ilya Fushman, Dirk Englund, Nick Stoltz, Pierre Petroff, and Jelena Vuckovic. Dipole induced transparency in waveguide coupled photonic crystal cavities. *Opt. Express*, 16(16):12154–12162, Aug 2008. Available from: <http://www.opticsexpress.org/abstract.cfm?URI=oe-16-16-12154>, doi:10.1364/OE.16.012154. 122
- [FMK⁺10] Andrei Faraon, Arka Majumdar, Hyochul Kim, Pierre Petroff, and Jelena Vučković. Fast electrical control of a quantum dot strongly coupled to a photonic-crystal cavity. *Phys. Rev. Lett.*, 104(4):047402, Jan 2010. doi:10.1103/PhysRevLett.104.047402. 67, 68
- [FSS⁺10] J. M. Fink, L. Steffen, P. Studer, Lev S. Bishop, M. Baur, R. Bianchetti, D. Bozyigit, C. Lang, S. Filipp, P. J. Leek, and A. Wallraff. Quantum-to-classical transition in cavity quantum electrodynamics. *Phys. Rev. Lett.*, 105(16):163601, Oct 2010. doi:10.1103/PhysRevLett.105.163601. 36, 55, 58
- [Gar04] C. W. Gardiner. *Handbook of Stochastic Methods*. Springer, 2004. 10, 11, 12, 16, 20, 21
- [GJ09a] J. Gough and M. James. Quantum feedback networks: Hamiltonian formulation. *Communications in Mathematical Physics*, 287:1109–1132, 2009. 10.1007/s00220-008-0698-8. Available from: <http://dx.doi.org/10.1007/s00220-008-0698-8>. 17
- [GJ09b] J. Gough and M.R. James. The series product and its application to quantum feedforward and feedback networks. *Automatic Control, IEEE Transactions on*, 54(11):2530–2544, nov. 2009. doi:10.1109/TAC.2009.2031205. 4, 6, 15, 17, 18, 19

- [GNH90a] Hu Gang, Cun-Zheng Ning, and H. Haken. Codimension-two bifurcations in single-mode optical bistable systems. *Phys. Rev. A*, 41(5):2702–2711, Mar 1990. doi:10.1103/PhysRevA.41.2702. 45, 46
- [GNH90b] Hu Gang, Cun-Zheng Ning, and H. Haken. Distribution of subcritical hopf bifurcations and regular and chaotic attractors in optical bistable systems. *Phys. Rev. A*, 41(7):3975–3984, Apr 1990. doi:10.1103/PhysRevA.41.3975. 45, 46
- [GNW10] John E. Gough, Hendra I. Nurdin, and Sebastian Wildfeuer. Commutativity of the adiabatic elimination limit of fast oscillatory components and the instantaneous feedback limit in quantum feedback networks. *Journal of Mathematical Physics*, 51(12):123518, 2010. Available from: <http://link.aip.org/link/?JMP/51/123518/1>, doi:10.1063/1.3520513. 116, 130
- [Got09] D. Gottesman. An Introduction to Quantum Error Correction and Fault-Tolerant Quantum Computation. *ArXiv e-prints*, April 2009. arXiv:0904.2557. 100, 102, 104, 107, 131, 134
- [GPZ92] C. W. Gardiner, A. S. Parkins, and P. Zoller. Wave-function quantum stochastic differential equations and quantum-jump simulation methods. *Phys. Rev. A*, 46(7):4363–4381, Oct 1992. doi:10.1103/PhysRevA.46.4363. 4, 6, 7, 8, 9, 10, 11, 12, 13, 14, 31
- [GZ04] C. W. Gardiner and P. Zoller. *Quantum Noise: A Handbook of Markovian and Non-Markovian Quantum Stochastic Methods with Applications to Quantum Optics*. Springer, 2004. 4, 6, 8, 9, 10, 11, 12, 14, 15, 16, 17, 23, 24, 26, 31, 33, 40, 42
- [HCLK98] C. J. Hood, M. S. Chapman, T. W. Lynn, and H. J. Kimble. Real-time cavity qed with single atoms. *Phys. Rev. Lett.*, 80(19):4157–4160, May 1998. doi:10.1103/PhysRevLett.80.4157. 51, 54, 55, 72

- [HKD⁺09] A. Houck, Jens Koch, M. Devoret, S. Girvin, and R. Schoelkopf. Life after charge noise: recent results with transmon qubits. *Quantum Information Processing*, 8:105–115, 2009. 10.1007/s11128-009-0100-6. Available from: <http://dx.doi.org/10.1007/s11128-009-0100-6>. 71, 122
- [HKY01] Christina J. Hood, H. J. Kimble, and Jun Ye. Characterization of high-finesse mirrors: Loss, phase shifts, and mode structure in an optical cavity. *Phys. Rev. A*, 64(3):033804, Aug 2001. [doi:10.1103/PhysRevA.64.033804](https://doi.org/10.1103/PhysRevA.64.033804). 73
- [HP84] R. L. Hudson and K. R. Parthasarathy. Quantum ito’s formula and stochastic evolutions. *Communications in Mathematical Physics*, 93:301–323, 1984. 10.1007/BF01258530. Available from: <http://dx.doi.org/10.1007/BF01258530>. 4, 12, 13
- [IYY⁺11] S. Iida, M. Yukawa, H. Yonezawa, N. Yamamoto, and A. Furusawa. Experimental demonstration of coherent feedback control on optical field squeezing. *ArXiv e-prints*, March 2011. [arXiv:1103.1324](https://arxiv.org/abs/1103.1324). 123
- [JNP08] M.R. James, H.I. Nurdin, and I.R. Petersen. h^∞ control of linear quantum stochastic systems. *Automatic Control, IEEE Transactions on*, 53(8):1787–1803, sept. 2008. [doi:10.1109/TAC.2008.929378](https://doi.org/10.1109/TAC.2008.929378). 4, 123
- [KAM10] J. Kerckhoff, M. A. Armen, and H. Mabuchi. Quantum remnants of absorptive bistability in the attojoule regime. *ArXiv e-prints*, December 2010. [arXiv:1012.4873](https://arxiv.org/abs/1012.4873). 37, 45, 48, 84, 85, 86, 87, 88, 89
- [KAPM11] Joseph Kerckhoff, Michael A. Armen, Dmitri S. Pavlichin, and Hideo Mabuchi. The dressed atom as binary phase modulator: towards attojoule/edge optical phase-shift keying. *Opt. Express*, 19(7):6478–6486, Mar 2011. Available from: <http://www.opticsexpress.org/abstract.cfm?URI=oe-19-7-6478>, [doi:10.1364/OE.19.006478](https://doi.org/10.1364/OE.19.006478). 37, 55, 61, 68, 84, 90, 92, 93, 97

- [KBSM09] Joseph Kerckhoff, Luc Bouten, Andrew Silberfarb, and Hideo Mabuchi. Physical model of continuous two-qubit parity measurement in a cavity-qed network. *Phys. Rev. A*, 79(2):024305, Feb 2009. doi:10.1103/PhysRevA.79.024305. 109, 110, 113, 116, 117, 121
- [KLP05] David Kribs, Raymond Laflamme, and David Poulin. Unified and generalized approach to quantum error correction. *Phys. Rev. Lett.*, 94(18):180501, May 2005. doi:10.1103/PhysRevLett.94.180501. 106, 134
- [KMV⁺10] H. S. Ku, F. Mallet, L. R. Vale, K. D. Irwin, S. E. Russek, G. C. Hilton, and K. W. Lehnert. Design and testing of superconducting microwave passive components for quantum information processing. *Applied Superconductivity, IEEE Transactions on*, PP(99):1–4, 2010. doi:10.1109/TASC.2010.2089403. 122
- [KNPM10] Joseph Kerckhoff, Hendra I. Nurdin, Dmitri S. Pavlichin, and Hideo Mabuchi. Designing quantum memories with embedded control: Photonic circuits for autonomous quantum error correction. *Phys. Rev. Lett.*, 105(4):040502, Jul 2010. doi:10.1103/PhysRevLett.105.040502. 4, 18, 19, 21, 99, 111, 113, 116, 122, 124, 125, 127, 128, 129, 130, 131, 133, 134, 137
- [KPCM11] J. Kerckhoff, D. S. Pavlichin, H. Chalabi, and H. Mabuchi. Design of nanophotonic circuits for autonomous subsystem quantum error correction. *ArXiv e-prints, to appear in New J. Phys. (special issue Integrated Quantum Optics)*, February 2011. arXiv:1102.3143. 21, 99, 122, 133, 135, 138, 139
- [LKH⁺10] Liu Liu, Rajesh Kumar, Koen Huybrechts, Thijs Spuesens, Gunther Roelkens, Erik-Jan Geluk, Tjibbe de Vries, Philippe Regreny, Dries Van Thourhout, Roel Baets, and Geert Morthier. An ultra-small, low-power, all-optical flip-flop memory on a silicon chip. *Nat Photon*,

- 4(3):182–187, 03 2010. Available from: <http://dx.doi.org/10.1038/nphoton.2009.268>. 47, 69
- [Lug84] L. A. Lugiato. *Progress in Optics*. North-Holland, Amsterdam, 1984. 44
- [Mab08a] Hideo Mabuchi. Coherent-feedback quantum control with a dynamic compensator. *Phys. Rev. A*, 78(3):032323, Sep 2008. [doi:10.1103/PhysRevA.78.032323](https://doi.org/10.1103/PhysRevA.78.032323). 123
- [Mab08b] Hideo Mabuchi. Derivation of maxwell-bloch-type equations by projection of quantum models. *Phys. Rev. A*, 78(1):015801, Jul 2008. [doi:10.1103/PhysRevA.78.015801](https://doi.org/10.1103/PhysRevA.78.015801). 45
- [Mab09a] Hideo Mabuchi. Cavity-qed models of switches for attojoule-scale nanophotonic logic. *Phys. Rev. A*, 80(4):045802, Oct 2009. [doi:10.1103/PhysRevA.80.045802](https://doi.org/10.1103/PhysRevA.80.045802). 124, 125, 126
- [Mab09b] Hideo Mabuchi. Continuous quantum error correction as classical hybrid control. *New Journal of Physics*, 11(10):105044, 2009. Available from: <http://stacks.iop.org/1367-2630/11/i=10/a=105044>. 123, 125
- [Mab11] H. Mabuchi. Coherent-feedback control strategy to suppress spontaneous switching in ultra-low power optical bistability. *ArXiv e-prints*, January 2011. [arXiv:1101.3461](https://arxiv.org/abs/1101.3461). 123
- [MD02] H. Mabuchi and A. C. Doherty. Cavity quantum electrodynamics: Coherence in context. *Science*, 298(5597):1372–1377, 2002. Available from: <http://www.sciencemag.org/content/298/5597/1372.abstract>, [arXiv:http://www.sciencemag.org/content/298/5597/1372.full.pdf](http://www.sciencemag.org/content/298/5597/1372.full.pdf), [doi:10.1126/science.1078446](https://doi.org/10.1126/science.1078446). 36, 37
- [Mil09] D. Miller. Device requirements for optical interconnects to silicon chips. *Proceedings of the IEEE*, 97(7):1166–1185, July 2009. [doi:10.1109/JPROC.2009.2014298](https://doi.org/10.1109/JPROC.2009.2014298). 48

- [Mil10a] David A. B. Miller. Are optical transistors the logical next step? *Nat Photon*, 4(1):3–5, 01 2010. Available from: <http://dx.doi.org/10.1038/nphoton.2009.240>. 48
- [Mil10b] David A. B. Miller. Optical interconnects to electronic chips. *Appl. Opt.*, 49(25):F59–F70, Sep 2010. Available from: <http://ao.osa.org/abstract.cfm?URI=ao-49-25-F59>, doi:10.1364/AO.49.000F59. 50
- [Moo05] K. L. Moore. *Ultracold Atoms, Circular Waveguides, and Cavity QED with Milli-meter-scale Electromagnetic Traps*. PhD thesis, University of California, Berkeley, 2005. 74
- [MTCK96] H. Mabuchi, Q. A. Turchette, M. S. Chapman, and H. J. Kimble. Real-time detection of individual atoms falling through a high-finesse optical cavity. *Opt. Lett.*, 21(17):1393–1395, Sep 1996. Available from: <http://ol.osa.org/abstract.cfm?URI=ol-21-17-1393>, doi:10.1364/OL.21.001393. 36, 72
- [MvdS99] H. J. Metcalf and P. van der Straten. *Laser Cooling and Trapping*. Springer, 1999. 80
- [NC00] M. A. Nielsen and I. L. Chuang. *Quantum Computation and Quantum Information*. Cambridge University Press, 2000. 99, 100, 102, 104, 105, 107, 119, 122, 134
- [NJD09] Hendra I. Nurdin, Matthew R. James, and Andrew C. Doherty. Network synthesis of linear dynamical quantum stochastic systems. *SIAM Journal on Control and Optimization*, 48(4):2686–2718, 2009. Available from: <http://link.aip.org/link/?SJC/48/2686/1>, doi:10.1137/080728652. 4, 123
- [NJP09] Hendra I. Nurdin, Matthew R. James, and Ian R. Petersen. Coherent quantum lqg control. *Automatica*, 45(8):1837 – 1846, 2009. Available from: <http://www.sciencedirect.com/science/>

- [article/B6V21-4WK4B3T-1/2/70c6e071f68558e9690d6fe9cbfb10f0](#),
[doi:DOI:10.1016/j.automatica.2009.04.018](#). 4
- [NTS⁺10] Kengo Nozaki, Takasumi Tanabe, Akihiko Shinya, Shinji Matsuo, Tomonari Sato, Hideaki Taniyama, and Masaya Notomi. Sub-femtojoule all-optical switching using a photonic-crystal nanocavity. *Nat Photon*, 4(7):477–483, 07 2010. Available from: <http://dx.doi.org/10.1038/nphoton.2010.89>. 47, 69
- [OLB08] Ognyan Oreshkov, Daniel A. Lidar, and Todd A. Brun. Operator quantum error correction for continuous dynamics. *Phys. Rev. A*, 78(2):022333, Aug 2008. [doi:10.1103/PhysRevA.78.022333](https://doi.org/10.1103/PhysRevA.78.022333). 123
- [ORX⁺87] L. A. Orozco, M. G. Raizen, Min Xiao, R. J. Brecha, and H. J. Kimble. Squeezed-state generation in optical bistability. *J. Opt. Soc. Am. B*, 4(10):1490–1550, Oct 1987. Available from: <http://josab.osa.org/abstract.cfm?URI=josab-4-10-1490>, [doi:10.1364/JOSAB.4.001490](https://doi.org/10.1364/JOSAB.4.001490). 72
- [Par92] K. R. Parthasarathy. *An Introduction to Quantum Stochastic Calculus*. Birkhauser, Berlin, 1992. 4, 12, 13
- [PLP⁺11] Alberto Peruzzo, Anthony Laing, Alberto Politi, Terry Rudolph, and Jeremy L. O’Brien. Multimode quantum interference of photons in multipoint integrated devices. *Nat Commun*, 2, 03 2011. Available from: <http://dx.doi.org/10.1038/ncomms1228>. 122
- [PLZY08] David Press, Thaddeus D. Ladd, Bingyang Zhang, and Yoshihisa Yamamoto. Complete quantum control of a single quantum dot spin using ultrafast optical pulses. *Nature*, 456(7219):218–221, 11 2008. Available from: <http://dx.doi.org/10.1038/nature07530>. 71
- [PMO09] Alberto Politi, Jonathan C. F. Matthews, and Jeremy L. O’Brien. Shor’s quantum factoring algorithm on a photonic chip. *Science*, 325(5945):1221, 2009. Available from:

<http://www.sciencemag.org/content/325/5945/1221.abstract>,
[arXiv:http://www.sciencemag.org/content/325/5945/1221.full.pdf](http://www.sciencemag.org/content/325/5945/1221.full.pdf),
[doi:10.1126/science.1173731](https://doi.org/10.1126/science.1173731). 99

- [PSK08] T.P. Purdy and D.M. Stamper-Kurn. Integrating cavity quantum electrodynamics and ultracold-atom chips with on-chip dielectric mirrors and temperature stabilization. *Applied Physics B: Lasers and Optics*, 90:401–405, 2008. 10.1007/s00340-007-2879-0. Available from: <http://dx.doi.org/10.1007/s00340-007-2879-0>. 73
- [RC88] P.R. Rice and H.J. Carmichael. Single-atom cavity-enhanced absorption. i. photon statistics in the bad-cavity limit. *Quantum Electronics, IEEE Journal of*, 24(7):1351–1366, jul 1988. [doi:10.1109/3.974](https://doi.org/10.1109/3.974). 44
- [ROKD91] A. T. Rosenberger, L. A. Orozco, H. J. Kimble, and P. D. Drummond. Absorptive optical bistability in two-state atoms. *Phys. Rev. A*, 43(11):6284–6302, Jun 1991. [doi:10.1103/PhysRevA.43.6284](https://doi.org/10.1103/PhysRevA.43.6284). 44
- [RRH⁺04] Christian F. Roos, Mark Riebe, Hartmut Häffner, Wolfgang Hänsel, Jan Benhelm, Gavin P. T. Lancaster, Christoph Becher, Ferdinand Schmidt-Kaler, and Rainer Blatt. Control and measurement of three-qubit entangled states. *Science*, 304(5676):1478–1480, 2004. Available from: <http://www.sciencemag.org/content/304/5676/1478.abstract>,
[arXiv:http://www.sciencemag.org/content/304/5676/1478.full.pdf](http://www.sciencemag.org/content/304/5676/1478.full.pdf),
[doi:10.1126/science.1097522](https://doi.org/10.1126/science.1097522). 99
- [RTB⁺89] M. G. Raizen, R. J. Thompson, R. J. Brecha, H. J. Kimble, and H. J. Carmichael. Normal-mode splitting and linewidth averaging for two-state atoms in an optical cavity. *Phys. Rev. Lett.*, 63(3):240–243, Jul 1989. [doi:10.1103/PhysRevLett.63.240](https://doi.org/10.1103/PhysRevLett.63.240). 45

- [RTB⁺91] G. Rempe, R. J. Thompson, R. J. Brecha, W. D. Lee, and H. J. Kimble. Optical bistability and photon statistics in cavity quantum electrodynamics. *Phys. Rev. Lett.*, 67(13):1727–1730, Sep 1991. doi:10.1103/PhysRevLett.67.1727. 45, 48, 54, 55, 72
- [SBF⁺10] C Santori, P E Barclay, K-M C Fu, R G Beausoleil, S Spillane, and M Fisch. Nanophotonics for quantum optics using nitrogen-vacancy centers in diamond. *Nanotechnology*, 21(27):274008, 2010. Available from: <http://stacks.iop.org/0957-4484/21/i=27/a=274008>. 36, 122
- [SC88] C.M. Savage and H.J. Carmichael. Single atom optical bistability. *Quantum Electronics, IEEE Journal of*, 24(8):1495–1498, aug 1988. doi:10.1109/3.7075. 45, 50, 54, 55
- [SD81] M. D Srinivas and E. B. Davies. Photon counting probabilities in quantum optics. *Optica Acta: International Journal of Optics*, 28(7):981–996, 1981. 31
- [SDGK69] A. Szoke, V. Daneu, J. Goldhar, and N. A. Kurnit. Bistable optical element and its applications. *Applied Physics Letters*, 15(11):376–379, 1969. Available from: <http://link.aip.org/link/?APL/15/376/1>, doi:10.1063/1.1652866. 48, 50
- [Sie86] A. Siegman. *Lasers*. University Science Books, 1986. 72, 73, 74
- [SSM08] Gopal Sarma, Andrew Silberfarb, and Hideo Mabuchi. Quantum stochastic calculus approach to modeling double-pass atom-field coupling. *Phys. Rev. A*, 78(2):025801, Aug 2008. doi:10.1103/PhysRevA.78.025801. 17
- [Ste] D. A. Steck. Cesium d line data. Available from: <http://steck.us/alkalidata/cesiumnumbers.pdf>. 38, 70, 72, 73
- [Sto06] J. K. Stockton. *Continuous Quantum Measurement of Cold Alkali-Atom Spins*. PhD thesis, California Institute of Technology, 2006. 20, 21

- [SvHM04] John K. Stockton, Ramon van Handel, and Hideo Mabuchi. Deterministic dicke-state preparation with continuous measurement and control. *Phys. Rev. A*, 70(2):022106, Aug 2004. doi:10.1103/PhysRevA.70.022106. 118
- [Tan99] Sze M Tan. A computational toolbox for quantum and atomic optics. *Journal of Optics B: Quantum and Semiclassical Optics*, 1(4):424, 1999. Available from: <http://stacks.iop.org/1464-4266/1/i=4/a=312>. 34, 118, 131
- [TMH⁺08] Ph Tamarat, N B Manson, J P Harrison, R L McMurtrie, A Nizovtsev, C Santori, R G Beausoleil, P Neumann, T Gaebel, F Jelezko, P Hemmer, and J Wrachtrup. Spin-flip and spin-conserving optical transitions of the nitrogen-vacancy centre in diamond. *New Journal of Physics*, 10(4):045004, 2008. Available from: <http://stacks.iop.org/1367-2630/10/i=4/a=045004>. 71
- [TRK92] R. J. Thompson, G. Rempe, and H. J. Kimble. Observation of normal-mode splitting for an atom in an optical cavity. *Phys. Rev. Lett.*, 68(8):1132–1135, Feb 1992. doi:10.1103/PhysRevLett.68.1132. 36, 72
- [Tsa09] Mankei Tsang. Time-symmetric quantum theory of smoothing. *Phys. Rev. Lett.*, 102(25):250403, Jun 2009. doi:10.1103/PhysRevLett.102.250403. 88
- [vH07] Ramon van Handel. *Filtering, Stability, and Robustness*. PhD thesis, California Institute of Technology, 2007. 31, 34
- [vHM05] Ramon van Handel and Hideo Mabuchi. Quantum projection filter for a highly nonlinear model in cavity qed. *Journal of Optics B: Quantum and Semiclassical Optics*, 7(10):S226, 2005. Available from: <http://stacks.iop.org/1464-4266/7/i=10/a=005>. 45

- [Vit67] A. Viterbi. Error bounds for convolutional codes and an asymptotically optimum decoding algorithm. *Information Theory, IEEE Transactions on*, 13(2):260 – 269, apr 1967. doi:10.1109/TIT.1967.1054010. 92
- [VSB⁺01] Lieven M. K. Vandersypen, Matthias Steffen, Gregory Breyta, Costantino S. Yannoni, Mark H. Sherwood, and Isaac L. Chuang. Experimental realization of shor’s quantum factoring algorithm using nuclear magnetic resonance. *Nature*, 414(6866):883–887, 12 2001. Available from: <http://dx.doi.org/10.1038/414883a>. 99
- [Wel03] Lloyd R. Welch. Hidden Markov Models and the Baum-Welch Algorithm. *IEEE Information Theory Society Newsletter*, 53(4), December 2003. Available from: http://www.itsoc.org/publications/nltr/it_dec_03final.pdf. 92
- [Win09] D J Wineland. Quantum information processing and quantum control with trapped atomic ions. *Physica Scripta*, 2009(T137):014007, 2009. Available from: <http://stacks.iop.org/1402-4896/2009/i=T137/a=014007>. 99
- [WM93] H. M. Wiseman and G. J. Milburn. Quantum theory of field-quadrature measurements. *Phys. Rev. A*, 47(1):642–662, Jan 1993. doi:10.1103/PhysRevA.47.642. 24, 26, 31, 33
- [WM08] D. F. Walls and G. J. Milburn. *Quantum Optics*. Springer, 2008. 18, 29, 30, 41, 51, 64
- [YHW⁺07] Xiaodong Yang, Chad Husko, Chee Wei Wong, Mingbin Yu, and Dim-Lee Kwong. Observation of femtojoule optical bistability involving fano resonances in high-q/ v_m silicon photonic crystal nanocavities. *Applied Physics Letters*, 91(5):051113, 2007. Available from: <http://link.aip.org/link/?APL/91/051113/1>, doi:10.1063/1.2757607. 47, 69